Universidade do Vale do Paraíba
Instituto de Pesquisa e Desenvolvimento
Programa de Pós-Graduação em Física e Astronomia

Nathanne Cristina Vilela Rost

IRON OXIDE NANOPARTICLES SYNTHESIS OPTIMIZED BY DESIGN OF EXPERIMENTS AND MAGNETIC PARTICLE IMAGING PERFORMANCE OF MAGNETOLIPOSOMES

SÍNTESE DE NANOPARTÍCULAS DE ÓXIDO DE FERRO OTIMIZADA POR PLANEJAMENTO EXPERIMENTAL E DESEMPENHO DE MAGNETOLIPOSSOMAS EM *MAGNETIC PARTICLE IMAGING*

São José dos Campos, SP

2021

NATHANNE CRISTINA VILELA ROST

IRON OXIDE NANOPARTICLES SYNTHESIS OPTIMIZED BY DESIGN OF EXPERIMENTS AND MAGNETIC PARTICLE IMAGING PERFORMANCE OF MAGNETOLIPOSOMES

SÍNTESE DE NANOPARTÍCULAS DE ÓXIDO DE FERRO OTIMIZADA POR PLANEJAMENTO EXPERIMENTAL E DESEMPENHO DE MAGNETOLIPOSSOMAS EM *MAGNETIC PARTICLE IMAGING*

Doctorate Thesis submitted to the Postgraduate Program on Physics and Astronomy from Universidade do Vale do Paraíba in fulfillment of the requirements for the degree of Doctor in Physics and Astronomy.

Tese de Doutorado apresentada ao Programa de Pós-Graduação em Física e Astronomia da Universidade do Vale do Paraíba, como complementação dos créditos necessários para obtenção do grau de Doutora em Física e Astronomia.

Supervisor: Prof. Dr. Leandro José Raniero

Co-supervisor: Prof. Dr. Carlos M. Rinaldi-Ramos (*University of Florida*)

São José dos Campos, SP
2021

Fundação Valeparaibana de Ensino

BIBLIOTECA

TERMO DE AUTORIZAÇÃO DE DIVULGAÇÃO DA OBRA

Ficha catalográfica

Rost, Nathanne Cristina Vilela
Iron oxide nanoparticles synthesis optimized by design of experiments and magnetic particle imaging performance of magnetoliposomes / Nathanne Cristina Vilela Rost; orientador, Leandro Jose Raniero; co-orientador Carlos M. Rinaldi-Ramos. - São José dos Campos, SP, 2021.
1 CD-ROM, 121 p.

Tese (Doutorado) - Universidade do Vale do Paraíba, São José dos Campos. Programa de Pós-Graduação em Física e Astronomia.

Inclui referências

1. Física e Astronomia. 2. Iron oxide nanoparticles. 3. Chemical coprecipitation. 4. Magnetoliposome. 5. Magnetic Particle Imaging. I. Raniero, Leandro Jose, orient. II. Rinaldi-Ramos, Carlos M. , co-orient. III. Universidade do Vale do Paraíba. Programa de Pós-Graduação em Física e Astronomia. IV. Título.

Eu, Nathanne Cristina Vilela Rost, autor(a) da obra acima referenciada:

Autorizo a divulgação total ou parcial da obra impressa, digital ou fixada em outro tipo de mídia, bem como, a sua reprodução total ou parcial, devendo o usuário da reprodução atribuir os créditos ao autor da obra, citando a fonte.

Declaro, para todos os fins e efeitos de direito, que o Trabalho foi elaborado respeitando os princípios da moral e da ética e não violou qualquer direito de propriedade intelectual sob pena de responder civil, criminal, ética e profissionalmente por meus atos.

São José dos Campos, 1 de Outubro de 2021.

Autor(a) da Obra

NATHANNE CRISTINA VILELA ROST

"IRON OXIDE NANOPARTICLES SYNTHESIS OPTIMIZED BY DESIGN OF EXPERIMENTS AND MAGNETIC PARTICLE IMAGING PERFORMANCE OF MAGNETOLIPOSOMES."

Tese aprovada como requisito parcial à obtenção do grau de Doutor, do Programa de Pós-Graduação em Física e Astronomia, do Instituto de Pesquisa e Desenvolvimento da Universidade do Vale do Paraíba, São José dos Campos, SP, pela seguinte banca examinadora:

PROF. DR. MARCO ANTONIO RAMIREZ RAMOS

PROF. DR. LEANDRO JOSÉ RANIERO

PROF. DR. CARLOS M. RINALDI-RAMOS / University of Florida

PROF. DR. OLI LUIZ DORS JUNIOR

PROF.ª DR.ª ANA MARIA DO ESPIRITO SANTO - Unifesp

PROF. DR. ERIC GARY FULLER – University of Florida

Prof.ª Dr.ª Lucia Vieira

Diretora do IP&D – Univap

São José dos Campos, 25 de agosto 2021.

This thesis is dedicated to Nicolas Faria Nunes, my husband and the love of my whole life; to Nanci Cunha Vilela Rost, my mother and the most important teacher during my entire journey and Phelipe Vilela Rost, my brother and one of the people who support me most in my academic research. *In memoriam* of Carlos Roberto Rost, my father, and the brightest star.

ACKNOWLEDGMENTS

First of all, this work would never be possible if God could not provide me grace, patience, health, wisdom, and persistence. Secondly, if I had not a supportive family, all my PhD and academic life would certainly be harder. Therefore, I would like, from all my heart, to thank my mother Nanci Rost for always give me strength, good energy, and good advice. You are the best example of how important is to study hard, work hard and fight even harder! I love you to the moon and back, girl! The memories of our childhood lead our personality as adults. Thank you to Carlos Rost, the brightest star in my sky for had been the best example of a father, ethic, and love. I also would like to thank Nicolas Faria Nunes for always been willing to hear me, for understanding all the times in which I prioritize my research, and for taking care of me with good foods when I get home after a lab day. I am pretty sure that you are the best husband, I love you so much! I could not forget to say thank you to a person who is often interested in my research, asking about science and nanoparticles. Your curiosity makes me feel like a good scientist and encourages me to work hard! Thank you for being always present in my life and help me in every single difficulty, my wonderful brother, Phelipe Rost. I try to be a good example for two very special girls, the brightness of my eyes and one of the most important reasons for my happiness. My goddaughters, princesses, and loves of my whole life, Camila Lima and Eloise Gwyneth, I study hard and try to be a good person because of you. To the people who always have a smile in receiving me and good talking even on my more exhaustive days, I would like to say that love all of you and I am so grateful for being part of this incredible family. Thank you for also being part of my life and indirectly contribute to this PhD, family Faria and Nunes.

I could not forget that the undergraduate period is the basis for post-graduate life. Then, thank you very much Wallyson Ribeiro for been with me since that time in which my love for science started. You are not only a friend or godfather but also a brother! I extend this thank you to William Rodrigues and the whole family, especially aunt Rita Rosangela. To somebody we will never forget, I want to say thank you from all my heart for believe in us and be one of the first to inspire our researches, uncle Joaquim Rodrigues, your histories will always be

remembered and taught to next generations. I can express the same gratitude feeling to Denise Maria, a sister that God generously gave me and who is there for me whatever the situation is. Thank you to be the first person to say “I will miss you, but you must go on this adventure” when I was planning the exchange in the USA. I could not forget to mention Marilia Rodrigues, for your friendship and for always been around and your family, for taking care of us on exhaustive studying days during engineering exams. I can live a million stories abroad, but the six amazing months in Porto City will always be remembered as the best! Caroline Barreto and Daniel Gonçalves, thank you for been present in every important step of my life! You both are essential for everything that I can successfully conclude, because of your encouragement. Daniel, you are the example of the scientist that I want to be. Caroline, you had taught me to enjoy life, see the best things even in the worst situation. I love you, my friends!

It is important to have in mind that the daily routine and the lab are essential for the PhD. Therefore, I would like to thank the friends from LNS for all these years working together, sharing the good results either the difficulties, thank you for all coffee and help. Especially the amazing and supporter girls, Marcela Candido, Thaís Veriato, Viviane Jesus, and Paula Vieira. I am so blessed to call you friends and share with you not only the lab-related problems but also some personal questions. Thank you for listen to me and enjoy good times together. I am also thankful to Vitor Poli for the support on *in vitro* experiments and good company. Prof. Dr. Leandro Raniero, thank you for being a reference as a researcher and supervisor since my undergraduate. Thank you for allow me to have autonomy in my studies and explore new ideas. I also would like to thank Prof. MSc. Fátima Broca and Prof. Dr. Josafá Aguiar for being supportive friends in my academic research and career. Thank you also to all administrative members of IP&D and Laboratório Central Multiusuários for the attention that you all always express to the students. Thank you also to Maria Alice Macedo and Prof. Dra. Sandra Costa, who constantly helped me regarding documents, during the two times when I was studying abroad. The success of the students is related to the quality of the University. In all these years in which I had the honor of studying at UNIVAP, the employees and professors always expressed respect to us and this is related to the excellence of this Institution. Then, thank you to all

safety, cleaning, and administration members for being part of this PhD. The professors who had taught me a lot of good things, so many physics formulae, and how to have patience when doing research, thank you very much! You all are what moves this nation and the entire world! Thank you for all the good work not only in classrooms but also in laboratories. I also want to thank Prof. Dr. Oli Dors for helping me with questions regarding the PPGFA and for encouraging me to travel to the USA, believing in my academic capacity.

The way I do research, plan experiments, and process data significantly improved when I visited The Rinaldi Lab. Therefore, thank you very much Prof. Dr. Carlos M. Rinaldi-Ramos for hosting me in your lab and for always been willing to help with the lots of questions about magnetic nanoparticles I had. Further, I would like to thank all the research groups and the people who never saved time to cooperate with me, especially my coauthors. I also thank the University of Florida and the Department of Chemical Engineering, J. Crayton Pruitt Family Department of Biomedical Engineering, and Sharma Lab. I have no doubts that it was great to be a Florida Gator! The time in which I lived in Gainesville, Florida was very important not only for my academic learning but also for getting to know so special friends, Ivanise and Ciro Branco, Vera and Pitágoras Bispo, Kacoli Sen, and the Fuller family. Thank you for helping me in the lab, questions of science, and more important, thank you for showing me new cultures and habits, which was very important for my cultural exchange abroad. Yasmin, Eric, Benjamin, and Thomas Fuller, thank you for becoming part of my family and for all the good memories we have together. Go gators!

Finally, thank you to Coordenação de Aperfeiçoamento de Pessoal de Nível Superior for the PhD scholarship in Brazil (88887.149922/2017-00) and in U.S. (88881.189058/2018-01). I could not achieve a doctorate degree without this financial support.

To everybody who reads this thesis, don’t stop believing in science, support the researchers. Science saves lives!

“Differences of habit and language are nothing at all if our aims are identical and our hearts are open.” J. K. Rowling

ABSTRACT

Iron oxide nanoparticles are clinically approved by Food and Drug Administration (FDA) in the United States of America, where are already used in cases of iron deficiency and as contrast agents for magnetic resonance imaging, highlighting the relevance of such nanomaterials in society. Liposomes are also accepted by FDA and the entrapment of iron oxide nanoparticles originates magnetoliposomes that represents one of the ways for combining magnetic nanoparticles and hydrophilic or hydrophobic molecules. Such combination can be useful for applications in combinatorial therapies, for instance, magnetic hyperthermia and Magnetic Particle Imaging (MPI), a new imaging modality. In this work, magnetic nanoparticles were synthesized by chemical coprecipitation, evaluating the effects of reactional parameters over the hydrodynamic diameter and composition of the samples by using Plackett-Burman experimental design. The results allowed a more reliable protocol, considering the experimental combinations that lead to smaller particles composed mostly of magnetite. Next, magnetoliposomes were prepared from magnetic nanoparticles stabilized by peptization. Characterization techniques were widely used and physical models were applied to data processing of magnetometry, magnetic susceptibility, and transmission electron microscopy. The magnetoliposomes performance as MPI tracers were compared to the nanoparticles (as-synthesized) and Ferucarbotran, the benchmark formulation. The results of this second stage of the work indicated improvement in the MPI physical signal per iron mass after the encapsulation, even though the most representative fraction of particles was governed by the Brownian relaxation mechanism. The magnetoliposomes had shown a signal more intense than Ferucarbotran, even with poorer resolution. This study can be useful for future works because one of the challenges in MPI researches is the production of tracers with performance equivalent to Ferucarbotran.

Keywords: iron oxide nanoparticles; chemical coprecipitation; Design of Experiments; magnetoliposomes; Magnetic Particle Imaging.

RESUMO

Nanopartículas de óxido de ferro são clinicamente aprovadas pela *Food and Drug Administration* (FDA) nos Estados Unidos, onde já são utilizadas em casos de deficiência de ferro e como agentes de contraste para ressonância magnética, ressaltando a relevância destes nanomateriais na sociedade. Lipossomas também são aceitos pela FDA e o encapsulamento de nanopartículas de óxido de ferro origina magnetolipossomas, que representam uma das formas de se combinar nanopartículas magnéticas a moléculas hidrofílicas ou hidrofóbicas. Esta combinação é útil para terapias combinadas, por exemplo, como hipertermia magnética e *Magnetic Particle Imaging* (MPI), uma nova modalidade de imagem. Neste trabalho, nanopartículas magnéticas foram sintetizadas por coprecipitação química, avaliando-se os efeitos dos parâmetros reacionais no diâmetro hidrodinâmico e composição das amostras por meio do planejamento experimental de Plackett-Burman. Os resultados possibilitaram um protocolo mais confiável, considerando-se as combinações experimentais que viabilizam partículas menores compostas principalmente por magnetita. A seguir, magnetolipossomas foram produzidos a partir de nanopartículas magnéticas estabilizadas por peptização. Técnicas de caracterização foram amplamente utilizadas e modelos físicos aplicados no processamento dos dados de magnetometria, suscetibilidade magnética e microscopia eletrônica de transmissão. A performance dos magnetolipossomas como marcadores para MPI foi comparada às nanopartículas como sintetizadas e ao Ferucarbotran, formulação de referência. Os resultados desta segunda fase do trabalho indicaram uma melhora no sinal físico do MPI por massa de ferro após o encapsulamento, embora a fração de nanopartículas mais representativa fosse governada pelo mecanismo de relaxamento de Brownian. Os magnetolipossomas apresentaram sinal mais intenso do que o Ferucarbotran, ainda que resolução inferior. Este estudo poderá ser útil para trabalhos futuros, pois um dos maiores desafios em pesquisas com MPI é a produção de marcadores com performance equivalente ao Ferucarbotran.

Palavras-chave: Nanopartículas de óxidos de ferro; coprecipitação química; Planejamento de Experimentos; magnetolipossomas; Magnetic Particle Imaging.

LIST OF FIGURES

CHAPTER 1

CHAPTER 2

LIST OF TABLES

CHAPTER 1

CHAPTER 2

LIST OF EQUATIONS

CHAPTER 1

CHAPTER 2

LIST OF ABBREVIATIONS

AGA	Speed of alkaline agent addition
bcp	Body centered cubic-packed
ccp	Cubic close-packed
DLS	Dynamic Light Scattering
DLVO	Derjaguin-Landau-Verwey-Overbeck
DMS	Dynamic Magnetic Susceptibility
DNA	Deoxyribonucleic acid
DOE	Design of Experiments
DSPC	1,2-distearoyl-*sn*-glycero-3-phosphocholine
FDA	Food and Drug Administration
Fe/OH agent	Molar ratio between the total quantity of iron and alkalin
Fe^{2+}/Fe^{3+}	Molar ratio between ferrous and ferric ions
FFP	Field-free point
FINEP	Financiadora de Estudos e Projetos
FTIR	Fourier Transform Infrared Spectroscopy
FWHM	Full-Width-at-Half-Maximum
hcp	Hexagonal close-packed
HIV-1	Human immunodeficiency virus type 1
ICCD	International Centre for Diffraction Data
IONPs	Iron Oxide Nanoparticles
IONPs@TMAOH	Iron Oxide Nanoparticles peptized with tetramethylammonium hydroxide
IR	Infrared
k	Factor
L	Level
ML	Magnetoliposomes
MPI	Magnetic Particle Imaging
MPR	Magnetic Particle Relaxometer
MRI	Magnetic Resonance Imaging

NP	Non-peptized
NPs	Nanoparticles
PDF	Powder Diffraction File
PDI	Polydispersity index
pH	Hydrogenionic potential
P	Peptized
PSF	Point Spread Function
PSNR	Peak Signal-to-Noise Ratio
RT	Reaction Time
SAR	Specific Absorption Rate
SPIONs	Superparamagnetic Iron Oxide Nanoparticles
SQUID	Superconducting Quantum Interference Device
SR	Stirring Rate
TEM	Transmission Electron Microscopy
Temp	Temperature
TMAOH	Tetramethylammonium hydroxide
TQI	Total Quantity of Iron
XRD	X-Ray Diffractometry

LIST OF SYMBOLS

$\tilde{\nu}_0$	Wavenumber
χ''_p	The peak in the out-of-phase susceptibility
ν_i	The fundamental frequency of the mode
ϕ_B	Brownian fraction
ϕ_N	Néel fraction
K_a	Anisotropy constant
V_h	Nanoparticles hydrodynamic volume
V_c	Magnetic core volume
V_{iv}	Frequency (in FTIR)
$f_{\tilde{\nu}_0}$	frequency of the interferogram
f_0	Frequency (in DMS)
k_B	Boltzmann constant
v_i	Vibrational quantum number
η_0	The viscosity of the carrier
τ_B	Brownian relaxation time
τ_N	Néel relaxation time
χ'_0	Zero frequency in-phase susceptibility
χ'_∞	Infinite frequency in-phase susceptibility
D	Coefficient of diffusion
D_h	Hydrodynamic diameter
D_m	Magnetic diameter
D_{pg}	Number median diameter
D_{pv}	Arithmetic volume mean diameter
D_s	Critical diameter
D_{spm}	Critical diameter related to superparamagnetism
E	Total energy
H	Applied magnetic field
h	Planck's constant

H_c	Demagnetization
hcp	Hexagonal close-packed
K	Magnetic anisotropy
$k_b T$	Thermal energy
m	Dipole moment
M_s	Saturation magnetization
N_A	Avogadro constant
R	Gas constant per mole
T	Absolute temperature
T	Absolute temperature
V	Nanoparticles volume
α	Hydrodynamic radius of the sphere
η	Viscosity of the liquid carrier
θ	Angle between incident beam and the reflected by lattice plane (when discussing XRD) or angle between easy axis and particle magnetization (when presenting DMS)
$B(\tilde{\nu}_0)$	Source intensity
V'	Constant velocity of the movable mirror
d	Spacing between crystal planes
i	Vibrational mode
n	Order of reflection
δ	Retardation
λ	X-rays wavelength

LIST OF CHEMICAL FORMULAE

(Fe5O7(OH).4H2O	Ferrihydrite
$(NH_4)_6Mo_7O_{24}$	Ammonium molybdate
CH_3COONa	Sodium acetate
$CHCl_3$	Chloroform
Cl^-	Chloride
CO_3^{2-}	Carbonate
F^-	Fluoride
Fe	Iron
$Fe(OH)_3$	Ferric hydroxide or bernalite
$Fe_{16}O_{16}(OH)_y(SO_4)_z \cdot n\ H_2O$	Schwertmannite
Fe^{2+}	Ferrous ion
Fe^{3+}	Ferric ion
Fe_3O_4	Magnetite
$Fe_5HO_8 \cdot 4\ H_2O$	Ferrihydrite
$FeCl_2{\cdot}4H_2O$	Iron (II) chloride tetrahydrate
$FeCl_3{\cdot}6H_2O$	Iron (III) chloride hexahydrate
FeO	Wüstite
$Fe_x^{III}Fe_y^{II}(OH)_{3x+2y-z}(A^-)_{z;}\ A^- = Cl^-;\ ½\ SO_4^{2-}$	Green Rusts
HCl	Hydrochloric acid
HNO_3	Nitric acid
KCl	Potassium chloride
NaOH	Sodium hydroxide
$NH_2OH{\cdot}HCl$	Hydroxylamine hydrochloride
NH_4OH	Ammonium hydroxide
O^{2-}	Oxygen
OH^-	Hydroxyl
SO_4^{2-}	Sulfate
α-Fe_2O_3	Hematite

α-FeOOH	Goethite
β-FeOOH	Akaganeite
γ-Fe_2O_3	Maghemite
γ-FeOOH	Lepidocrocite
δ-FeOOH	Feroxite

TABLE OF CONTENTS

Background and significance

INTRODUCTION

The intrinsic properties of materials are modified by scale reduction because of surface effects. The proportion of atoms at the surface is greater than in the internal structure, due to size decreasing. Therefore, reactions among substances and adjacent atoms are faster and the amount of reactive groups is correlated to the surface-to-volume ratio. Thus, the inner structure, electronic, optical, and even the magnetic characteristics of the matter change at the nanoscale, which leads to relevant objects of study (THANH, 2012).

In 1800 decades, the transformation of the fundamental properties of matter was demonstrated, for the first time, by Michael Faraday, on a revolutionary experimental observation of how spatial confinement changes gold colloids' optical characteristics, which probably led to nowadays nanoscience basis. Twenty years before this finding, the classical electromagnetism was established by Ampère, Maxwell, Faraday, Oersted, Biot and Savart (THANH, 2012). In addition, it is important to mention Nikola Tesla’s inventions, such as electric clocks, radio, wireless communication systems, high-frequency induction heating, X-ray equipment, gaseous tube, and fluorescent lights and, notably, the discovery of rotating magnetic field (SWEZEY, 1958; VUJIĆ, 2006). The controversial theorem of Bohr and Van Leeuwen seriously questioned the classical physics validity in demonstrating the magnetic order in materials. According to the Bohr-van Leeuwen theorem, in thermal equilibrium, the magnetization of a moving ensemble of particles is zero in a constant magnetic field. This controversial theory indicated that classical statistical mechanics and Maxwell’s equation generate no magnetic order. Therefore, for supplying the necessity of a groundbreaking approach in the physics of magnetism, the quantum mechanics ideas started to disseminate in the early 1900s by the magnetism perceptions, along with the discovery of the electron and its spin, leading to the Golden Age of Understanding (THANH, 2012).

Next, important equations for magnetism, such as Langevin’s theory of paramagnetism and Weiss’s molecular field theory were based on the work of quantum physicists, as De Broglie, Pauli, Heisenberg, and other renowned

scientists. Although the undoubted relevance of these theoretical developments for magnetism, practical applications were affected, in fact, by military investigations on permanent magnets and the interaction of magnetic materials with electromagnetic radiation, during the World War II period. Meanwhile, the perception of anti-ferromagnetism and ferrimagnetism was being developed by Louis Néel, whose theory of superparamagnetism contributed to the comprehension of fine particles' magnetic properties. William Fuller Brown's work also supported this research field (THANH, 2012).

These theoretical efforts on understanding magnetism and quantum physics enabled the current practical investigations on magnetic nanoparticles, a field that has been strengthening researches, especially in medicine, because of interesting results that come from the non-homogeneous magnetization profile (See Chapter 2). Indeed, some formulations containing magnetic nanoparticles composed of iron oxides are clinically approved by Food and Drug Administration (FDA) in the United States of America, reinforcing the importance and impact of these magnetic materials in society (THANH, 2012).

The uses of magnetic nanoparticles include, but are not limited to, magnetic fluid hyperthermia (DEATSCH; EVANS, 2014), triggered drug release (MOROS *et al.*, 2019), contrast agents in Magnetic Resonance Imaging (MRI) (LEE; HYEON, 2012) and more recently, tracers for Magnetic Particle Imaging (MPI) (FERGUSON *et al.*, 2009). Some liposomal formulations are also accepted by FDA and the entrapment of magnetic nanoparticles in such structures can benefit the combination of the nanomaterial with both hydrophilic and hydrophobic substances (ALBERTS *et al.*, 2002; KAMMARI *et al.*, 2017).

However, the brazilian investments in nanotechnology are more directed to researches funding than products development. Worldwide, about 4 trillion dollars were related to nanotechnology applications and commodities in 2018, whereas in Brazil, in a period of 10 years (2006-2016), R$81.29 million were invested by Financiadora de Estudos e Projetos (FINEP) for 56 projects, representing R$1.45 million per project. The total amount invested in those studies was R$134.83 million, considering also the financed by private companies. In summary, 60.2% of the amount directed for projects related to nanotechnology was sponsored by the government (BARBOSA *et al.*, 2018). It is also important to highlight a lack of nanomaterials informations in the brazilian

regulations, consequently, the management of nanotechnological goods available for consumers is impacted (HUPFFER; LAZZARETTI, 2019).

In this context, the motivation of this thesis was to synthesize IONPs by the coprecipitation method, starting from a reliable protocol that allows producing materials with dimension at the nanoscale, composed mostly of magnetite and with a colloidally stable surface. Once the nanoparticles were synthesized and stabilized by peptization, the formation of magnetoliposomes was made, motivated by the possibility of investigating their performance as tracer agents for MPI, especially the changes in the physical signal when compared to as-synthesized IONPs. This work contributes to the national science as new investigations on iron oxide nanoparticles, because the growth of researches groups on magnetic nanoparticles is of scientific importance to future applications, owing to the potential benefit for society, for instance, formulations as the FDA-approved ones. International collaborations will certainly help Brazilian scientists in expanding nanotechnological techniques, build up methodologies and improve data acquisition.

This thesis highlights the production, characterization, and application of Iron Oxide Nanoparticles (IONPs), focusing on their physics properties and data interpretation based on theoretical models. For better clarification of the concepts involved in this work, this thesis was organized by chapters. In CHAPTER 1: *Synthesis of Iron Oxides Nanoparticles Optimized by Design of Experiments*, the coprecipitation of such magnetic nanoparticles in alkaline media will be discussed, also how experimental steps directly influence nanoparticles hydrodynamic diameter, crystalline structure (related to iron oxide types), and chemical composition. For that, factorial designs were applied to estimate the relevance and significance of each experimental parameter over the investigated properties of the nanoparticles. This first publication allowed a better comprehension of the synthesis processes and helped in understanding how magnetite particles could be obtained with dimensions in nanoscale, without the necessity of changing the chemical route or equipment (ROST *et al.*, 2019).

In CHAPTER 2: *Magnetic Particle Imaging Performance of Liposomes Encapsulating Iron Oxide Nanoparticles*, the reader will benefit from a literature review regarding nanoparticles encapsulation in larger structures, especially in magnetoliposomes formation, along with MPI data of magnetic nanoparticles

before and after the entrapment. Also, results from magnetometry, susceptometry, and microscopy will be presented and corroborated with the MPI performance of both as-synthesized nanoparticles and magnetoliposomes. Interestingly, the results from this second publication had shown an increase in MPI signal per unit mass of iron after encapsulation. Additionally, physics perceptions could be acquired by using quantum mechanics models on data treatment, for instance, the Langevin function applied to the magnetization curves and the Debye model on magnetic susceptibility characterization (ROST *et al.*, 2020).

OBJECTIVES

General

- Synthesize IONPs by coprecipitation in alkaline media.
- Stabilize the surface of the synthesized IONPs.
- Encapsulate IONPs in liposomes.
- Evaluate the physical signal of such liposomes and as-synthesized nanoparticles in MPI.

Specifics

- Establish a reliable and reproducible protocol for the production of IONPs by coprecipitation in alkaline media. To this end, investigate the most relevant experimental parameters over nanoparticles size and iron oxide crystalline structure.
- Achieve ferrofluids formation by stabilizing nanoparticles' surface with molecules that promote electrostatic repulsion.
- Obtain superparamagnetic IONPs (SPIONs) with saturation magnetization between 80 and 90 $emu.g^{-1}$.
- Prepare magnetoliposomes by thin-film hydration method, evaluate the physical size, hydrodynamic diameter, particles encapsulation, and surface charge.
- Determine the effects of nanoparticles peptization and concentration on magnetoliposomes properties.
- Analyze the MPI performance of SPIONs and magnetoliposomes, observing signal enhancement after encapsulation.
- Estimate the fraction of Néel and Brownian particles contributing to MPI signal, by applying Debye’s model.

Chapter 1: *Synthesis of Iron Oxide Nanoparticles Optimized by Design of Experiments*

Brazilian Journal of Physics (2019) 49:22–27
https://doi.org/10.1007/s13538-018-0616-2

SOCIEDADE BRASILEIRA DE FÍSICA

CONDENSED MATTER

Synthesis of Iron Oxide Nanoparticles Optimized by Design of Experiments

Nathanne C. V. Rost[1] · Fatima M. Broca[1] · Giulia C. Gonçalves[1] · Marcela A. Cândido[1] · Maiara L. Castilho[2] · Leandro J. Raniero[1]

Received: 3 September 2018 / Published online: 13 November 2018

Abstract
Magnetic iron oxide nanoparticles have been widely studied for technological and biomedical applications due to its small size and the possibility of functionalizing the surface with intended molecules. Magnetite is the most used phase because of superparamagnetic characteristic, and it is synthesized by co-precipitation, starting from ferrous and ferric ions in alkaline media. However, depending on parameters of chemical reactions, such as molar ratio between iron and hydroxyl groups, stirring rate, and temperature, different iron oxide structures are formed through distinct pathways. Since several variables can affect the size, chemical composition, and crystalline structure of iron oxide nanoparticles during the synthesis, it is very important to apply experimental routines with a well-defined protocol and planning practical steps can significantly improve the quality of products. Plackett-Burman methodology from design of experiments is a filtration analysis, used in the initial stages of a process to investigate the main effects of factors over a characteristic of the final material. In this work, Plackett-Burman technique was employed in order to optimize bare iron oxide nanoparticle production by co-precipitation method, relating the different crystalline phases produced to the experimental routine. Dynamic light scattering, Fourier transform infrared spectroscopy, and X-ray diffractometry were used to characterize the samples.

Keywords Experimental design · Iron oxide nanoparticles · Chemical co-precipitation

1 Introduction

Iron oxide nanoparticles (IONPs) have magnetic properties and biocompatibility and do not offer risks to the environment. In nature, these oxides have eight polymorphs and each one keeps unique characteristics, for example, the magnetic property according to the crystalline phase [1]. Goethite (α-FeOOH) is an antiferromagnetic iron hydroxide, generally found in soils, sediments, and other natural resources. The synthetic form of this oxide has an orthorhombic structure [2]. Once that hematite (α-Fe_2O_3) is highly resistant to corrosion, this is the most stable iron oxide, but at room temperature, it is weakly ferromagnetic. Maghemite (γ-Fe_2O_3) is ferrimagnetic at room temperature and is an oxidized phase of magnetite [1]. When iron corrosion occurs in presence of chloride, the antiferromagnetic oxide akaganeite (β-FeOOH) is formed; its structure allows applications in which a high catalytic activity is required [3]. In Fe^{2+} oxygenation, the first oxide generated is lepidocrocite (γ-FeOOH), which presents antiferromagnetic characteristic [4, 5]. Ferrihydrite ($Fe_5O_7(OH).4H_2O$) is an iron oxide found in soils obtained by fast Fe^{3+} hydrolysis [6, 7]. Magnetite (Fe_3O_4) is the most magnetic phase of iron oxide, once the ions Fe^{2+} and Fe^{3+}in its structure confer superparamagnetic properties. Consequently, this phase is desired for many applications such as contrast agent in magnetic resonance imaging (MRI) and magnetic hyperthermia [8].

In addition to the small dimension and high surface area, it is possible covering IONPs with many molecules, allowing various applications. Therefore, these nanomaterials have been widely studied for several technological and biomedical applications. Each use of IONPs requires set shape, magnetic

✉ Leandro J. Raniero
lraniero@univap.br

[1] Laboratório de Nanossensores, Instituto de Pesquisa e Desenvolvimento, Universidade do Vale do Paraíba, Av. Shishima Hifumi, São José dos Campos 12244-000, Brazil

[2] Laboratório de Bionanotecnologia, Instituto de Pesquisa e Desenvolvimento, Universidade do Vale do Paraíba, Av. Shishima Hifumi, São José dos Campos 12244-000, Brazil

1.1 LITERATURE REVIEW

1.1.1 Iron oxides

The chemical element of atomic number 26, iron (Fe), is not essential just for life, but also plays an important role in the biosphere (FAIVRE, 2016). Ferrous (Fe^{2+}) and ferric (Fe^{3+}) ions bonded to oxygen (O^{2-}) or hydroxyl groups (OH^-) composes the sixteen existent iron oxides, hydroxides, and oxide-hydroxides, including four polymorphs of Fe_2O_3 and five of FeOOH (CORNELL; SCHWERTMANN, 2003). Natural occurred forms of these compounds comprise magnetite (Fe_3O_4), hematite (α-Fe_2O_3), maghemite (γ-Fe_2O_3), and wüstite (FeO). Among the minerals composing the Earth´s crust, iron oxyhydroxides and oxides correspond to more than 5%; hematite is the most abundant (FAIVRE, 2016). Table 1.1 defines the existent types of iron oxides and hydroxides (CORNELL; SCHWERTMANN, 2003).

Table 1.1 – Natural occurring and synthesized iron oxides, oxyhydroxides, and hydroxides.

Oxide-hydroxide and hydroxides	***Oxides***
Goethite α-FeOOH	Hematite α-Fe_2O_3
Lepidocrocite γ-FeOOH	Magnetite Fe_3O_4 ($Fe^{II}Fe^{III}O_4$)
Akaganéite β-FeOOH	Maghemite γ-Fe_2O_3
Schwertmannite $Fe_{16}O_{16}(OH)_y(SO_4)_z \cdot n\ H_2O$	β-Fe_2O_3
δ-FeOOH	ε-Fe_2O_3
Feroxyhyte δ´-FeOOH	Wüstite FeO
High-pressure FeOOH	
Ferrihydrite $Fe_5HO_8 \cdot 4\ H_2O$	
Bernalite $Fe(OH)_3$	
$Fe(OH)_2$	
Green Rusts $Fe_x^{III}Fe_y^{II}(OH)_{3x+2y-z}(A^-)_z$; $A^- = Cl^-$; ½ SO_4^{2-}	

Reference: (CORNELL; SCHWERTMANN, 2003).

To state the difference and similarities among iron oxides, and the global role of each of them, a brief description of the characteristics of the most relevant

forms is provided. Magnetite is a black ferrimagnetic mineral composed of Fe^{2+} and Fe^{3+}. This iron ore has been found in organisms such as turtles, lobsters, and magnetotactic bacteria that naturally synthesize magnetite nanoparticles arranged in chains; these products are known as magnetosomes (CORNELL; SCHWERTMANN, 2003; FAIVRE, 2016). Because crystals of magnetite had been found in some organisms, like turtles, this is probably one mechanism of orientation aid for such animals (CORNELL; SCHWERTMANN, 2003).

Hematite, the oldest recognized iron oxide, a valuable ore and remarkable pigment with structure hexagonal close-packed (hcp) of anions, widely composing soils and rocks, had a crucial relevance for the modern world, once it has been very useful as a source of iron, especially for industries (CORNELL; SCHWERTMANN, 2003; FAIVRE, 2016). The color of α-Fe_2O_3 varies from blood-red when finely divided to sparkling grey or black if roughly crystalline. Similar to goethite, this is one of the end phases during iron oxides transformations (CORNELL; SCHWERTMANN, 2003).

The red-brownish ferrimagnetic mineral maghemite is isostructural with magnetite, distinct by some cation sites. It is generated from heating other iron oxides close to organic matter or magnetite weathering in soils (CORNELL; SCHWERTMANN, 2003).

The anions composing the structure of wüstite are arranged in cubic close-packed (ccp), analogously to sodium chloride arrangement. This oxide is an important intermediate for iron ores reduction, is composed only of ferrous ions. The lack of oxygen commonly makes this black iron oxide non-stoichiometric. Another class of Fe oxides is green rusts, as indicated by the name, produced by corrosion processes. Green rusts are assembled by $Fe^{2+}OH$ octahedral layers; part of the ferrous ions are replaced by ferric ions. Then, other species of anions bind between the layers, such as SO_4^{2-} and Cl^- (CORNELL; SCHWERTMANN, 2003).

Goethite, named by Johann Wolfang von Goethe in 1815, (α-FeOOH, hcp), is part of the composition of rocks, ochre deposits, and soils, conferring their yellowish color and is also an important industrial pigment. At ambient temperature, this is one of the most thermodynamically stable iron oxides and is the first and last oxide phase to be produced in many transformations (CORNELL; SCHWERTMANN, 2003).

The origin of the name of akaganeite is because of its discovery in the Akagané mine (Japan, 1962). Akaganeite is mainly encountered in rust in marine environments and hot brines, in which there is a large amount of Cl^-, rarely found in others nature states. The crystalline arrangement of akaganeite is body-centered cubic packing, bcp. This structure encloses a low level of F^- and Cl^- and the color of this oxide is bright yellow (CORNELL; SCHWERTMANN, 2003).

Cornell and Schwertmann describe ferrihydrite as an “important precursor of more stable iron oxides”, which often occurs onto surfaces with a reddish-brown color. This iron oxide can be just found as nanocrystals and consists of hcp with some structural defects. The OH and H_2O composition on ferrihydrite vary, but the general formula is $Fe_5O_8H \cdot H_2O$ and in the literature is also reported as $Fe_5HO_8 \cdot 4\ H_2O$ or $Fe_5O_7(OH) \cdot 4H_2O$ (CORNELL; SCHWERTMANN, 2003).

Other examples of iron oxides are lepidocrocite, an orange product of Fe^{2+} oxidation, based in ccp arrangement, present in biota, rust, soils, and rocks (CORNELL; SCHWERTMANN, 2003); feroxyhyte, first reported by Chukhrov *et al.* (1977), is a ferromagnetic, poorly crystalline δ'-FeOOH, reddish-brown color, that is usually found in surfaces (CHUKHROV *et al.*, 1977) and schwertmannite, easily obtained in the laboratory and naturally found as a pyrite oxidation product. The Schwertmannite framework is the same as akaganeite, with the difference that the former contains, instead of chloride ions, SO_4^{2-} ions (CORNELL; SCHWERTMANN, 2003).

Figure 1.1(a) shows the formation of iron oxide on limestone by atmospheric weathering of pyrite, whilst Figure 1.1(b) represents natural pigments of iron oxides (CORNELL; SCHWERTMANN, 2003).

Figure 1.1 – Representation of iron oxides: (a) formation on limestone and (b) iron oxides natural pigments.

Reference: Adapted from CORNELL; SCHWERTMANN, 2003.

1.1.2 Nanomaterials and iron oxide nanoparticles

Nanomaterials are systems presenting at least one dimension in the nanoscale (1 – 100 nm); the reduction of materials sizes to the nanometer order (10^{-9} m) and the interesting changes in their characteristics motivated the growth of nanoscience, nanoengineering, and nanotechnology limits. Nanoparticles (NPs) design and manipulation allow the control over their chemical, biological and physical properties, to create new devices with differentiated macro and microscopic features. For instance, characteristic as morphology, biocompatibility, surface charge, electronic and magnetic properties are defined according to the synthetic process. Because of the high surface-to-volume ratio, studies involving NPs have been developed, for example, for drug delivery, chemical reactions, energy storage, and electronic devices (MANSOORI, 2005). Moreover, the use of nanoparticles as delivery vehicles for vaccines during the COVID-19 pandemic is an exceptional example of how important nanomaterials are for solving global issues. The formulations BNT162b2, from Pfizer-BioNTech and mRNA-1273, Moderna, both consist of lipid nanoparticles based on messenger RNA technology, present efficacy of ~95% against the virus and their manufacturing is fast, compared to other vaccines. These two formulations were approved for clinical emergent use and are helping to mitigate the effects of a pandemic, which was responsible for more than two million deaths globally (KHURANA *et al.*, 2021).

The applicability of nanomaterials also includes areas as agriculture (KHOT *et al.*, 2012), diseases diagnosis and treatments (VINHAS *et al.*, 2015), sorbents and sensors (FRYXELL; CAO, 2012), food packaging (BRADLEY *et al.*, 2011), water treatment and environmental remediation (GHASEMZADEH *et al.*, 2014). In this context, ferrofluids are a convenient class of nanomaterials, investigated for several purposes, for instance, electronics devices, catalysis, and medical uses (SPIZZO *et al.*, 2017). Figure 1.2 represents nanoparticles size, surface coatings (electrostatic or steric stabilizers, as PEG or other polymers, and also targets for molecular recognition, antibodies, deoxyribonucleic acid – DNA, etc. and functional groups for further ligations), shape (spheres, cubes, star, rods or plates) and material (metal particles, liposomes, hydrogel particles, etc.) (SUN *et al.*, 2014).

Figure 1.2 – Schematic representation of nanoparticles in terms of size, surface, shape, and material.

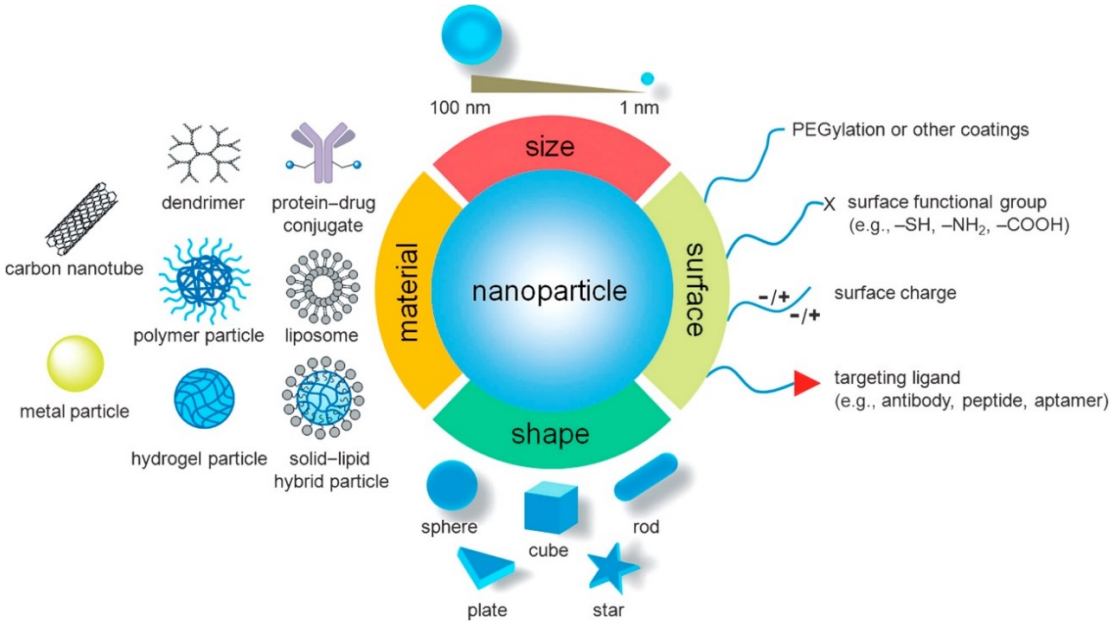

Reference: (SUN *et al.*, 2014).

A suspension of finely divided particles, even the ones which settle out over time, is defined as a colloid. In respect to magnetic nanoparticles, however, ferrofluids are suspensions that do not settle out due to colloidal stabilization that arises from surface coatings with dispersant molecules, such as surfactants or polymers. Further, thermal agitation prevents particles agglomeration because of Brownian motion. Unlike clutch fluids, also composed of magnetic particles, but

solidifies under applied field, the colloidal ferrofluids do not lose the flowability, even in presence of intense magnetic fields. Ferrofluids, for instance, IONPs, generally solids with dimensions of 3-15 nm are magnetic, single-domain nanomaterials (ROSENSWEIG, 1985). The superparamagnetic characteristics are due to particles' response to external magnetic field and recovery of the non-magnetic state when the field is removed. The magnetic properties of such materials can be designed by their dimension, considering that the magnetic domains are defined by a critical value of particles size (RAHMAN *et al.*, 2015), which will be better discussed in Chapter 2. Figure 1.3 demonstrates a ferrofluid subjected to a magnetic field (THANH, 2012).

Figure 1.3 – A ferrofluid composed of magnetite and the spikes induced by a permanent magnet, as a consequence of the balance between demagnetizing and gravitational energies.

Reference: (THANH, 2012).

Magnetic materials are classified according to the response to an applied field. Because of the absence of a permanent magnetic moment, diamagnetic materials are rarely employed, but alloys produced from the combination with paramagnetic components can be useful for purposes aiming the cancellation of the magnetism at a given temperature. Similar to the diamagnets, the paramagnets do not have a permanent magnetic moment and their uses are limited but can be required when very low temperatures are needed. In this sense, adiabatic demagnetization takes place (SPALDIN, 2010). Ferromagnets are appropriate flux multipliers and are also used for information and energy storage, which behave, respectively, as magnetic recording and magnets. Such applications are allowed by low coercivity and high permeability (HERNANDO *et al.*, 2001). The superparamagnetism, which will be more detailed in Chapter 2, is

characteristic of small ferri- or ferromagnetic particles because of the random flip of the magnetization direction influenced by the temperature (ENRIQUEZ-NAVAS; GARCIA-MARTIN, 2012). Such colloids had found applicability, for instance, in energy and data storage, magnetorheological polishing, and ferrofluids (JEONG *et al.*, 2007).

Because of the possibility of spatial control under an applied field due to the superparamagnetic response and taking into account that IONPs are usually well accepted *in vivo*, ferrofluids had also been extensively investigated for theranostic purposes (IYENGAR *et al.*, 2016). Controlled drug delivery (MOROS *et al.*, 2019), magnetic hyperthermia for cancer treatment (DEATSCH; EVANS, 2014), externally triggered heat and drug release (FULLER *et al.*, 2019), contrast agents for MRI (LEE; HYEON, 2012) and tracers for MPI (FERGUSON *et al.*, 2009) are some examples of the applicability of IONPs in medical researches. Additionally, as demonstrated in Figure 1.4, toxin removal from water and intoxicated human bodies, bacteria capturing, separation of proteins in bioscience researches, and biomolecule sensing by SPIONs serve as theranostic platforms; functionalization with targeting ligands takes place for specific recognitions (RAHMAN *et al.*, 2015).

Figure 1.4 – Biomedical applicability of SPIONs coated by biocompatible molecules.

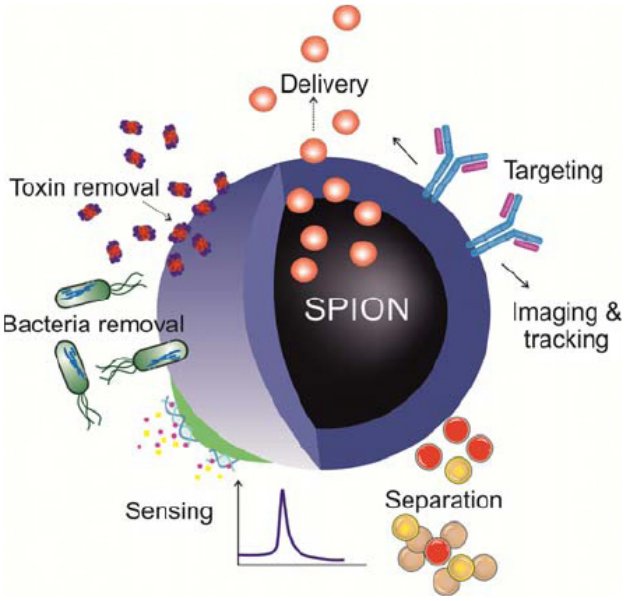

Reference: (RAHMAN *et al.*, 2015).

The FDA of the United States of America clinically approves IONPs (IYENGAR *et al.*, 2016). Some examples of those FDA-approved formulations include Ferumoxytol, authorized in 2009 and used in cases of iron deficiency, Resovist (Bayer Schering Pharma AG), composed of IONPs coated with carboxydextran, indicated for imaging liver and spleen lesions, allowed in 2001 and also approved in Europe, and Feridex (AMAG Pharma), an injectable solution applied as a contrast agent for MRI, accepted in 1996 (KAMMARI *et al.*, 2017). The acceptance of those magnetic nanoparticles for human uses highlights the importance of studies focused on developing new diagnostic and treatment supported by IONPs.

1.1.3 Synthesis of iron oxide nanoparticles by coprecipitation method

Even though iron oxides are found in nature, ferrofluids must be synthesized in laboratories. Some examples of the chemical routes able to produce IONPs are hydrothermal synthesis, microemulsions, sonochemical reactions, flow injection, and sol-gel processes. According to the colloidal nature of these particles with superparamagnetic properties, manufacturing monodispersed populations of IONPs by a reproducible method is still a challenge. Sometimes post-procedures are required, such as magnetic filtration,

size-exclusion chromatography, flow field gradient, or ultracentrifugation, leading to narrower size distribution and homogeneous composition of nanomaterials (LAURENT *et al.*, 2008).

Coprecipitation of iron salts is the most widespread method for magnetite nanoparticles synthesis (LAURENT *et al.*, 2008). Massart (1981) first proposed the preparation of IONPs through coprecipitation reactions replacing organic solvent by peptization with an alkaline solution as stabilizers (MASSART, 1981). This is not only the simplest and fastest way to obtain high production of IONPs, as well as environmental-friendly processes without toxic solvents. Further, the scale-up ability represents industrial significance. The purpose of this method is to prepare iron oxides at nanoscale, usually magnetite or maghemite, starting by an aqueous solution composed of Fe^{2+} and Fe^{3+} ions in stoichiometric ratio. Magnetite is completely precipitated at a hydrogenionic potential (pH) range between 8 and 14. Therefore, an alkaline solution is added. The reaction is described by Equation 1.1. Once magnetite is sensitive to oxidation and unstable in environmental conditions during coprecipitation reactions, the synthesis must be carried out under an inert atmosphere for avoiding the transformation of Fe_3O_4 to γ-Fe_2O_3 (LAURENT *et al.*, 2008).

$$Fe^{2+} + 2Fe^{3+} + 8OH^- \rightarrow Fe_3O_4 + 4H_2O \qquad \text{Equation 1.1}$$

Ahn *et al.* (2012) indicated the coexistence of reactions pathways that lead to the formation of different iron oxides during coprecipitation of ferrous and ferric ions. These authors showed that magnetite was synthesized by conversion mechanisms among other iron oxides (predominantly the topotactic transformation of goethite) depending on experimental conditions. At the beginning of the reaction, when pH is around 1-2, akaganeite is produced from the hydrolysis of $FeCl_3$ and stabilized by a stoichiometric amount of Cl^- ions incorporated into this structure. Nevertheless, this arrangement is converted into goethite at higher pH due to the replacement of Cl^- by OH^-. Those processes are defined as dissolution-recrystallization of akaganeite. One very important step during IONPs coprecipitation synthesis is to homogenize the pH in the reaction medium. Otherwise, two competing pathways can take place under slow or fast addition of the alkaline solution. The former promotes nucleation of akaganeite,

followed by goethite and magnetite formation. The latter leads to ferrous hydroxide nucleation and the production of magnetite through lepidocrocite. Magnetite is also obtained by goethite → hematite structural changes, a process comprising dehydration and rearrangement of goethite, caused by electron hopping between ferric and ferrous ions. All the complex coexistent pathways involved in magnetite formation affect the nanoparticles' size distribution and crystallinity (AHN *et al.*, 2012). It is important to address that high values of saturation magnetization are achieved when the atomic dipole of the nanoparticles is ordered; the different oxides obtained from reactions pathways in coprecipitation result in a magnetically dead layer on the surface of the nanoparticles, with saturation magnetization lower than the expected (UNNI *et al.*, 2017b). The magnetic properties of IONPs will be described in Chapter 2.

As long as in coprecipitation the growth of crystals is governed only by kinetic factors and the reactions are composed by a set of complicated pathways, the control over nanoparticles size distributions and shape is limited (LAURENT *et al.*, 2008; AHN *et al.*, 2012). The process of nanoparticles synthesis involves two stages that allow the production of colloids: nucleation and growth. The former arises immediately after the iron species concentration reaches a critical supersaturation, promoting the formation of nuclei (seeds), which act as a substrate for crystals growth. The latter involves solutes diffusion onto the surface of the pre-formed crystals, serving as a pathway for the nuclei growing (LAURENT *et al.*, 2008; THANH *et al.*, 2014).

LaMer and Dinegar (1950) were the first authors to explain nucleation and growth of particles in solution; according to this classical model, nuclei form from a short single burst and the growth is a separated stage, which allows the nuclei to develop uniformly, resulting in monodisperse particles (curve I, Figure 1.5) (LAMER; DINEGAR, 1950). Other mechanisms had been proposed for particles with uniform size distribution. For instance, rather than growth by diffusion, smaller particles can aggregate and result in clusters with homogenous dimensions (curve II, Figure 1.5). On the other hand, when subjected to nucleation multiple times, a self-sharpening of the size distribution is achieved by Ostwald ripening (curve III, Figure 1.5) (TARTAJ *et al.*, 2003).

Figure 1.5 – Schematic representation of nanoparticles nucleation and growth mechanisms. Curve I: the classical model of nucleation and uniform growth caused by diffusion, proposed by (LAMER; DINEGAR, 1950); curve II: nucleation and growth followed by aggregation of smaller particles; curve III: multiple nucleation event and growth by Ostwald ripening growth.

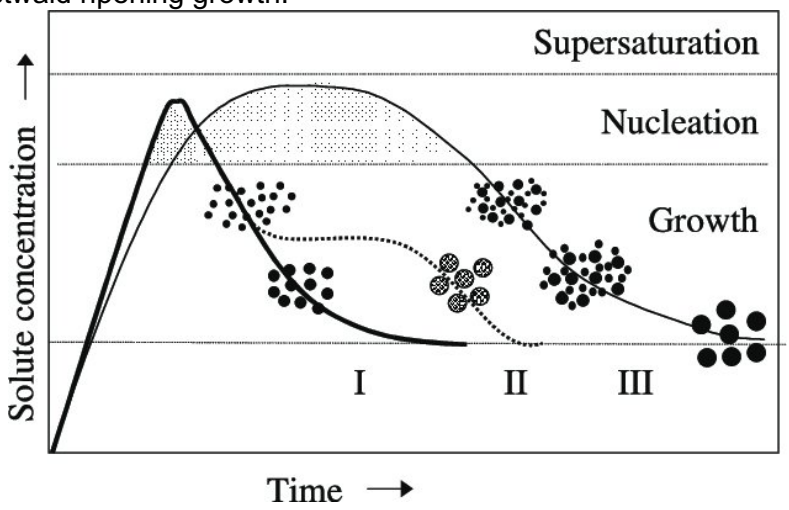

Reference: (TARTAJ *et al.*, 2003).

1.1.4 Stabilization of magnetic nanoparticles

IONPs tend to spontaneously aggregate to minimize the high surface energy, considering the instability and magnetic dipolar forces. As a result of combinatorial forces (Van der Waals, electrostatic, magnetic dipolar, and steric), the stability of magnetic nanoparticles relies on the equilibrium between repulsive and attractive mechanisms. DLVO theory (Derjaguin-Landau-Verwey-Overbeck) describes the electrostatic and Van der Waals forces. Isotropic and anisotropic interactions can contribute to interparticle interactions. The former is strongly induced in short-range by Van der Waals forces and the latter is generated from magnetic dipolar forces among particles (LAURENT *et al.*, 2008).

To ensure the potential applicability under magnetic fields and in a biological medium, and also the dispersion and increasing in surface-to-volume ratio compared to the bulk material, it is important to maintain chemical stability. Long-chain molecules adsorbed on nanoparticles surface avoids magnetic dipole interaction between particles by steric repulsion and consequently, agglomeration is eliminated (ROSENSWEIG, 1985; ANDRADE, ÂNGELA L. *et al.*, 2012). Electrostatic repulsions can be achieved by adding salts to particles' surfaces, for example, citrate coating (SARASWATHY *et al.*, 2014) or surfactants

(DEVI; MOHANTA, 2009). Figure 1.6 symbolizes particles stabilization by electrostatic and steric repulsion (LAURENT *et al.*, 2008).

Figure 1.6 – Stabilization of particles by (a) electrostatic layer and (b) steric repulsion (b).

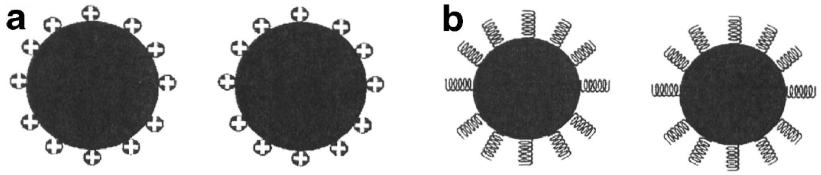

Reference: (LAURENT *et al.*, 2008).

Because the iron atoms on the surface of the particles behave as Lewis acids and coordinates with molecules that are lone-pair donators, in aqueous media Fe coordinates with water, which dissociates and forms hydroxyl groups. Therefore, IONPs are readily functionalized with amphoteric OH^- and may act as bases or acids. Thus, magnetite surface can be positive or negative according to the pH and the isoelectric point is generally at around pH 6.8 (LAURENT *et al.*, 2008).

Tetramethylammonium hydroxide (TMAOH) is a surfactant that chemically stabilizes IONPs. The OH^- present at the surface of the NPs absorbs the cationic species $[(CH_3)_4N]^+$ of TMAOH, which promotes electrostatic repulsion and confers colloidal stability to the solution. In other words, favors ferrofluids formation and improves size control. Indeed, TMAOH has a very active peptizing role, and additionally, the ability to make colloids dispersible also increases the crystallinity of the nanoparticles (ANDRADE, ÂNGELA L. *et al.*, 2012). The peptizing activity of TMAOH is represented in Figure 1.7.

Figure 1.7 – Repulsive forces created by tetramethylammonium cations adsorbed on magnetic nanoparticles surface, promoting electrostatic stabilization.

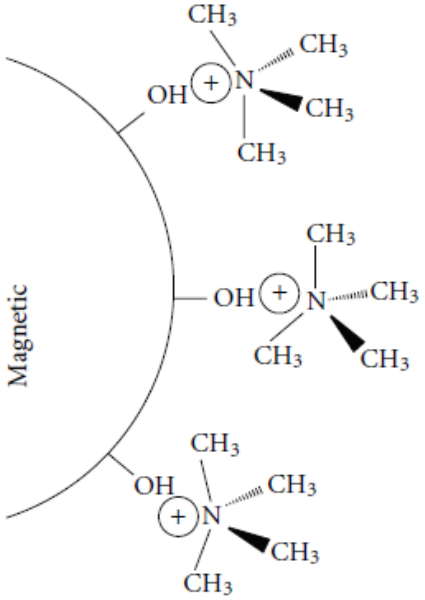

Reference: (ANDRADE, ÂNGELA L. *et al.*, 2012).

1.1.5 Design of Experiments applied to coprecipitation reactions

It is worthy to note that coprecipitation reactions yield considerable amounts of IONPs with potential scalability, easy execution, and accessible cost. Despite the undeniable efficacy of this chemical route, the lack of reproducibility affects the control over nanoparticles size distribution and other characteristics, such as the Specific Absorption Rate (SAR) that measures the heating capacity for hyperthermia applications (MÉRIDA *et al.*, 2015). It is extensively discussed in the literature that defined experimental parameters improve the homogeneity of IONPs size, crystalline structure, and magnetic properties during coprecipitation of the oxides. Consequently, the stirring rates, pH, the molar ratio between ferrous and ferric ions and between the total amount of iron and the alkaline agent, temperature, media composition, speed of addition of the basic solution, and the atmosphere (inert or non-inert) must be considered (KARAAGAC *et al.*, 2011; KARAAGAC; KOCKAR, 2012b; a; MÉRIDA *et al.*, 2015).

Magnetite structure can be represented as $[Fe^{3+}]_{Th}[Fe^{3+}Fe^{2+}]_{Oh}O_4$, once is composed by one tetrahedral and two octahedral iron sites of the face-centered cube of oxygen. Then, maintaining the $1Fe^{2+}$:$2Fe^{3+}$ ratio is decisive for the

homogeneous composition of IONPs. For this reason, aiming to preserve the chemical balance between iron ions, coprecipitation reactions are usually carried out under a nitrogen atmosphere, which prevents Fe^{2+} to Fe^{3+} oxidation. Karagaac and Kockar (2012) investigated the effect of $[Fe^{2+}]/[Fe^{3+}]$ in IONPs formation in an oxidizing environment. These authors confirmed the presence of co-products at 888 cm^{-1} in the FT-IR spectra, in samples synthesized with molar ratio=0.5 (1 Fe^{2+} / 2 Fe^{3+}), characterizing α-iron oxyhydroxide. This IR band disappeared when using $[Fe^{2+}]/[Fe^{3+}] \geq 0.8$, then it is essential to set an adequate ratio for magnetite formation. In addition, particles size and saturation magnetization both increased proportionally to the ratio between ferrous and ferric ions; it is well-known that at low field bigger particles are magnetized more easily than smaller ones (KARAAGAC; KOCKAR, 2012b).

Another important factor to be taken into account when synthesizing IONPs by coprecipitation route is the total amount of iron ions. Particles' crystallinity and size tend to reduce when prepared from higher amounts of iron because of kinetic results (KARAAGAC *et al.*, 2010).

Irrespective of the easy accomplishment of coprecipitation synthesis, producing magnetic nanoparticles relies on multiple steps and independent variables. For instance, the experimental specifications can vary, as temperature, reactants concentration, pH, and the molar ratio between reagents. In many processes that are dependent on a bunch of parameters, in industries, commerce, and laboratories, one or more characteristic of the final product can be affected by a single cause or a combination of them (MAHMOUDI *et al.*, 2008). It is also important to take into consideration that each cause or factor (k) can include one or more levels (L) (HIBBERT, 2012). The study of the influences of experimental steps has L^k possible combinations. In this sense, for a process made through 5 factors, each of them with 2 levels, 32 combinations should be completed for a thorough investigation of the effects over the final features, which is time-consuming and expensive (MAHMOUDI *et al.*, 2008; HIBBERT, 2012).

In this context, the Design of Experiments (DOE) overcomes the necessity of complete several runs to study the effects of parameters and levels over commodities. DOE is a multivariate data analysis that, by fitting the information in a linear or quadratic empirical function, estimates the interaction among factors and levels and how changing them alters final responses (HIBBERT, 2012). More

specifically, factorial designs investigate the connection between factors and levels. This statistical theory relies on orthogonal matrices, in which the inputs are based on the factors and levels. Next, experimental runs suggest the order of randomization in which the experiments must be carried out; this ensures that uncontrolled variables will not be partly responsible for irreproducibility. Based on these theoretical combinations, experimental practices are completed and the final responses of each are used for estimating the relation between one or more variables and also among the levels (MAHMOUDI *et al.*, 2008; HIBBERT, 2012).

For designs in which the intention is to outline the main effects over the responses, factorial mathematic models ensure a minimum number of experimental runs on a maximum amount of factors. One of the most used two-level fractionated designs is the Plackett-Burman methodology that is a filtration study applied in the initial stages of a certain process. As a prelude to optimization, this screening design aims to confirm the real significance of factors on the product characteristics (HIBBERT, 2012).

Karagaac and Kockar (2016) optimized IONPs production using magnetic properties as the response by experimental design in an orthogonal matrix and having a molar ratio between Fe^{2+} and Fe^{3+}, total iron ion concentration, base concentration, and reaction time as input parameters, with three levels each one. The authors related that an appropriate choice of factors could optimize the superparamagnetic characteristics of the materials (KARAAGAC; KOCKAR, 2016). Merida et. al (2015) employed a full factorial design aiming to define the key parameters of coprecipitation synthesis. These authors produced IONPs peptized with TMAOH and high SAR, starting from three factors and three center points (MÉRIDA *et al.*, 2015).

1.1.6 X-Ray Diffractometry

Crystal arrangements are generally differentiated by X-ray Diffractometry (XRD), a powerful technique able to identify unknown substances when the atoms of an organized framework scatter X-ray photons elastically (CHATTERJEE, 2001). The physics principle that governs the XRD technique is based on wavelengths of 10^{-3} to 10^{1} nm, which means high-energy electromagnetic waves, usually acquired in laboratories by sealed tubes. In these

cases, heating a tungsten filament in a vacuum generates electrons, which are accelerated by a high potential field (EPP, 2016). Multiple scattering and absorption effects may occur from the incidence of X-rays photons on a target, as exemplified in Figure 1.8 (SEIBERT; BOONE, 2005).

Figure 1.8 – Possible X-ray interactions originated from: (a) unattenuated beams (no interaction), (b) photoelectric absorption, (c) Rayleigh scattering and (d) Compton scattering.

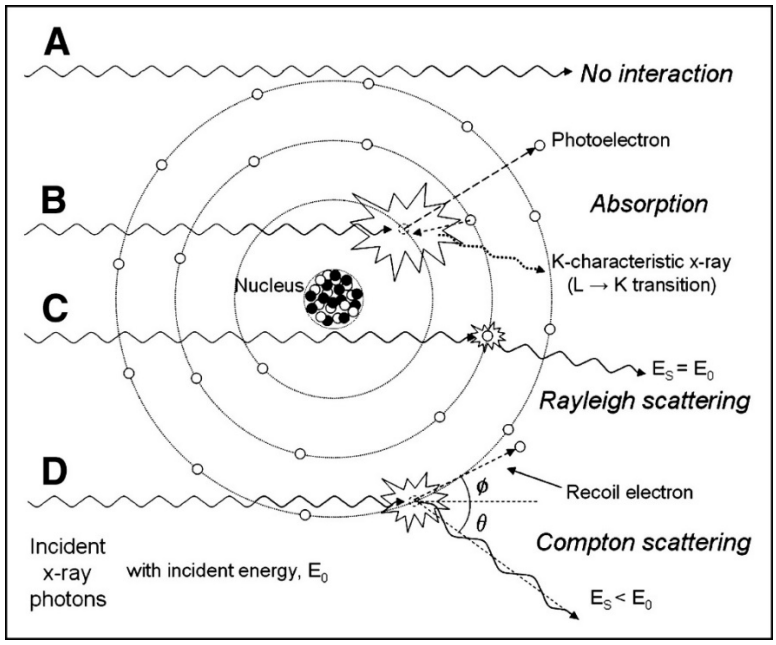

Reference: (SEIBERT; BOONE, 2005).

Bremsstrahlung is one of the two notable effects resulted from incident electrons on the generation of X-rays, that is the continuous distribution of wavelengths, caused by the deceleration of electrons. Another scattering is the ionization of atoms impinged by the incident radiation because of electrons ejection from the inner shells. In this case, a more stable state is achieved by the "jumping" of electrons from outer shells to fill the gaps in the inner shells. Consequently, photons are emitted because of the difference between the energies of electrons from distinct shells (EPP, 2016).

Relevant information can be extracted from XRD, such as degree of crystallization, particle size, and lattice constant determination. Bragg's Law summarizes the geometrical interpretation of the constructive interferences involved in XRD. This technique is based on X-rays diffraction by organized atomic planes and the angle of the diffracted signal. Figure 1.9 graphically

represents Bragg's Law (Equation 1.2), which allows the derivation of lattice spacing considering the crystal planes that diffract X-rays (CHATTERJEE, 2001; EPP, 2016).

$$n\lambda = 2d\ \sin\theta \qquad \text{Equation 1.2}$$

Where n = order of reflection, λ = X-rays wavelength, d = spacing between crystal planes, and θ = angle between the incident beam and the reflected by lattice plane. The interplanar spaces of crystallographic phases are identified by the angle θ, in which constructive X-rays interact with the crystalline structure (CHATTERJEE, 2001).

Figure 1.9 – Graphical representation of Bragg's Law: the geometric requirement for diffraction to occur from lattice planes.

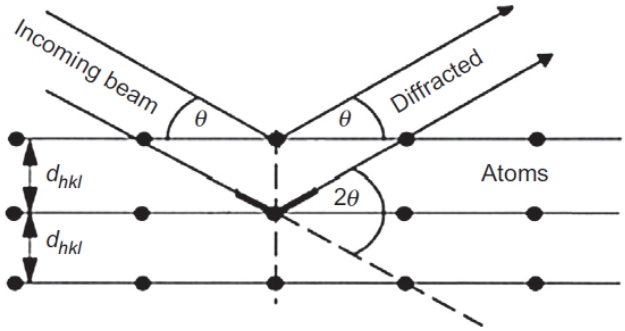

Reference: (EPP, 2016).

The collision of the X-ray photons on the atoms of a sample leads to specific diffraction phenomena due to the periodic arrangements of each matter. Therefore, the crystal structure of several materials can be investigated from the constructive or destructive scattering of radiation (EPP, 2016).

The diffractograms are recorded by a camera and the relative peak intensities are compared with standard patterns accessible in the database of Powder Diffraction File (PDF), from the International Centre for Diffraction Data (ICCD) (CHATTERJEE, 2001).

The Rietveld method is an evaluation tool for distinguishing several peaks in a unique diffractogram. The measured patterns are refined by calculations that consider equipment parameters and microstructure. The involved equations take

into account the intensities at 2θ, lattice parameters and space groups, occupation and temperature factor, the position of all atoms, crystallite size, texture, phase contents, and microstrains. For reliability observation, plots of the calculated and measured data are compared. The best refinement is the one that does not present large discrepancies, which means that both data are almost superimposed. These analyses simplify the differentiation of complex materials (EPP, 2016).

In respective to atoms organization, according to Cornell and Schwertmann (2003), “almost all iron oxides are crystalline” (CORNELL; SCHWERTMANN, 2003). For certain arrangements of iron oxides, oxyhydroxides, and hydroxides, small amounts of Cl^-, SO_4^{2-} and CO_3^{2-} can be part of the structure. These compounds are distinct by their atomic structural unit arrangement that is usually organized in hcp or ccp arrays of anions. With regards to ccp organization, the interstices are usually occupied by trivalent or divalent iron in octahedral coordination, $Fe(O,OH)_6$, and in some cases, filled with tetrahedral iron coordination (FeO_4). The dehydroxylated forms of oxide hydroxides are partially originated from similar anions organization, which assures the occurrence of cations rearrangement and OH loss, necessary for structural transformations (CORNELL; SCHWERTMANN, 2003). A representation of the different crystal structures of the most important iron oxides is depicted in Figure 1.10 (WU *et al.*, 2015).

Figure 1.10 - Crystallographic data and crystalline structure of (a) α-Fe2O3, (b) Fe3O4, and (c) γ-Fe2O3. Fe2+ and Fe3+ ions are represented, respectively, by black and green balls. O2- is illustrated as red balls.

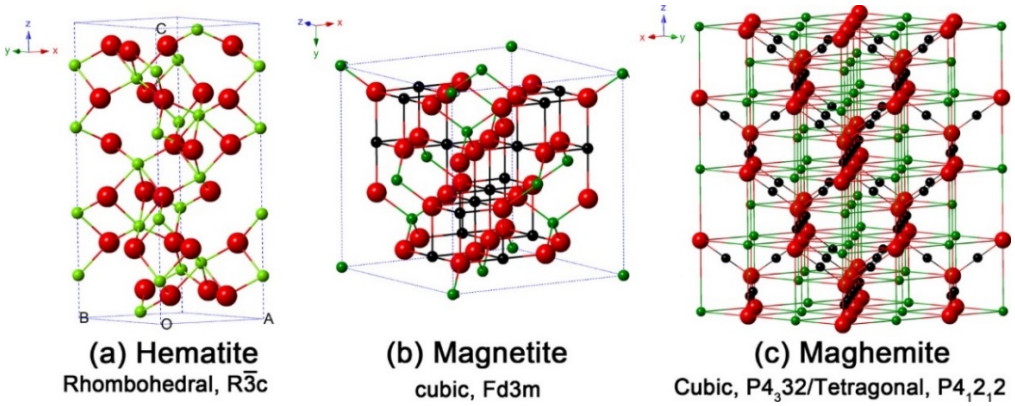

Reference: (WU *et al.*, 2015).

The most notable issue of characterizing iron oxides by XRD is the fact that the structure of those compounds is very similar. For instance, the cubic arrangement of maghemite has the same diffraction that magnetite and both can be differentiated just by some line shift at some angles, as represented in Figure 1.11. However, as any iron oxide phase can be obtained simply by oxidation or reduction of precursor forms, collecting XRD data is, in some cases, a basic characterization step to classify the types of magnetic oxides and the crystal arrangement (WU *et al.*, 2015).

Figure 1.11 – Diffractograms, from standard PDF, of maghemite (39-1346, purple color), magnetite (19-0629, blue color), and hematite (33-0664, red color).

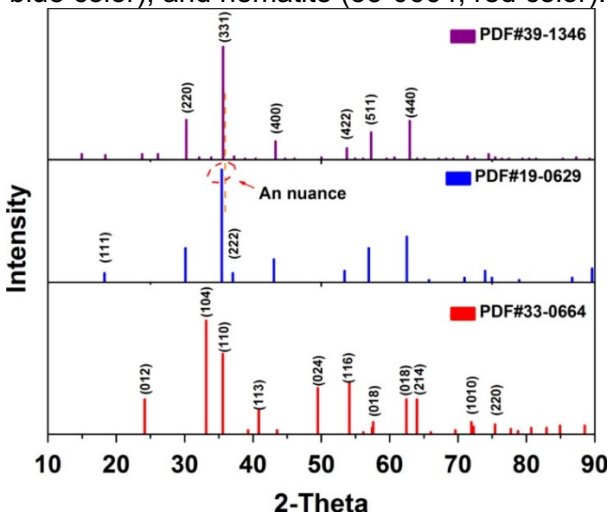

Reference: (WU *et al.*, 2015).

1.1.7 Fourier Transform Infrared Spectroscopy

Electromagnetic radiation is composed of electric and magnetic fields. The absorbance of the light, the visible region of the electromagnetic spectrum, arises from the interaction of the electric vector with the matter and is usually measured by spectroscopy. The absorbance of the light by molecules occurs in the infrared (IR) region (near IR: 14,000 – 4,000 cm^{-1}, mid IR: 4,000 – 400 cm^{-1}, and far IR: 400 – 4 cm^{-1}) (SMITH, 2011). By IR spectra, essential structural information about organic and inorganic molecules can be provided by Fourier Transform Infrared Spectroscopy (FTIR), based on transitions between energy states due to the interaction of electromagnetic waves with the matter (GRIFFITHS; DE HASETH, 2007; CHEN *et al.*, 2015). FTIR quantitative and qualitative applicability covers several purposes, such as biochemical data in forensic studies (ZHANG *et al.*, 2017), analyses of asphalt materials (HOU *et al.*, 2018), chemical characterization of bones, and dentin (LOPES *et al.*, 2018). In nanoscience, FTIR has been used for confirming the functionalization (SHARMA *et al.*, 2010) and adsorption (TSAI *et al.*, 2011) of substances on nanomaterials surface, formation of iron oxide nanoparticles (KARAAĞAÇ *et al.*, 2010), and also as complementary technique to XRD (BRAHMANWADE *et al.*, 2016; TRIVEDI *et al.*, 2017).

The basis of FTIR is the absorbance of molecular vibrations that occur from the motion of atomic structure as simples as diatomic to complex compounds, for instance, organics. The degree of freedom of a molecule containing *N* atoms is *3N*, related to the number of vibrational modes of atoms and their translational and rotational movements in the three perpendicular directions at once (x, y, and z axes) (GRIFFITHS; DE HASETH, 2007). Those molecular vibrations are represented in Figure 1.12 and, depending on their corresponding wavelengths and absorption band can be classified into bending or stretching modes. Therefore, functional groups and other components of a certain sample are identified conforming to the intensity and position of absorption peaks (YU *et al.*, 2019).

Figure 1.12 – Molecular vibrations from the motion of atomic structures: (a) stretching and (b) bending.

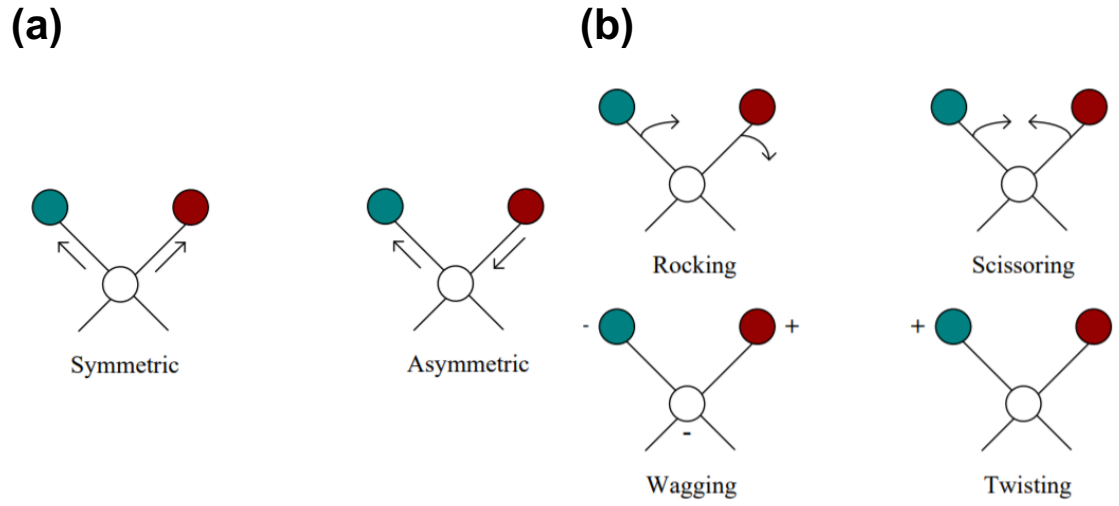

Reference: (YU *et al.*, 2019).

Harmonic displacements of atoms lead to vibrational modes of molecules, so that at a unique frequency v_i all atoms vibrate, considering each mode, *i.* Equation 1.3 describes the vibrational energy states, V_{iv} (GRIFFITHS; DE HASETH, 2007).

$$V_{iv} = h\nu_i \left(v_i + \frac{1}{2}\right) \qquad \text{Equation 1.3}$$

Where V_{iv} = frequency, usually given in units of hertz, h = Planck's constant, ν_i = the fundamental frequency of the mode and v_i = vibrational quantum number, i = vibrational mode. The wavenumbers of vibrational frequencies are often given in cm^{-1} (GRIFFITHS; DE HASETH, 2007).

Characteristic frequencies of specific functional groups can be detected in vibrational modes in which not the entire molecule has representative displacements, only a few atoms. In this way, it is possible to observe spectral features in defined regions, the so-called fingerprint of a given substance, considering that slight differences in the vibrational modes occur for every molecule, except enantiomers. To make data interpretation easier, structure correlation tables have been reported for the association of absorption bands with functional groups. With the assumption that some bands are related to the

frequency of significant motion of just some atoms and that those frequencies are different for each molecule, it is feasible to distinguish compounds (GRIFFITHS; DE HASETH, 2007).

Most vibrational modes have radiation energy in the region of the mid-infrared spectrum (400 – 4000 cm^{-1}), that is the difference between the ground and first excited state, respectively, v_i = 0 and v_i = 1. Information about vibrational modes of heavy atoms can be found at the far-infrared spectral region (10 – 400 cm^{-1}), but it is rarely applied (GRIFFITHS; DE HASETH, 2007).

Infrared spectra are acquired by devices that work based on the principle of interferometry. In an interferometer, a radiation beam is divided into two different paths, then a path difference is added, recombination of both paths occurs and interference between the beams takes place. A detector computes, as a function of path difference, the intensity variation related to the beam from the interferometer (GRIFFITHS; DE HASETH, 2007).

The interferometer is assembled by one fixed and one moving mirror, bisected by a beamsplitter, which can partially reflect a radiation beam from an external origin to the fixed mirror. The external radiation beam can also be transmitted to the movable mirror. Interference between these two paths of the radiation beam can occur when both beams return to the beamsplitter. Additionally, they are again transmitted and reflected. Therefore, the intensity variation of these two beams gives the spectral information of samples analyzed by FTIR spectrometers (GRIFFITHS; DE HASETH, 2007).

The so-called retardation optical path is the difference between the beams that go to the fixed and the movable mirrors and returns to the beamsplitter. The interferogram is defined as the modulated component that composes the intensity of the beam at the detector, related to the retardation. The efficiency of the beamsplitter, the amplifier characteristics, response of the detector, and also intensity of the source determines the interferogram amplitude. Equation 1.4 represents the interferogram (GRIFFITHS; DE HASETH, 2007).

$$S(\delta) = B(\tilde{\nu}_0)cos2\pi\tilde{\nu}_0\delta$$ Equation 1.4

Where $B(\tilde{\nu}_0)$ = source intensity at a $\tilde{\nu}_0$ = wavenumber, δ = retardation.

The cosine Fourier Transform of $B(\tilde{\nu}_0)$ is $S(\delta)$. Finally, by calculating this cosine from the interferogram, the spectrum is given by Fourier Transform, which can now be related to the molecular vibrations. Fourier Transform is described by Equation 1.5 (GRIFFITHS; DE HASETH, 2007).

$$f_{\tilde{\nu}_0} = 2V'\tilde{\nu}$$ Equation 1.5

Where $f_{\tilde{\nu}_0}$ = frequency of the interferogram, V' = constant velocity of the movable mirror ($cm.s^{-1}$), $\tilde{\nu}$ = wavenumber.

1.2 MATERIALS AND METHODS

In the method presented in this Chapter, bare IONPs were synthesized in alkaline media, without peptizing steps. The results of the procedures made in this way allowed a better understanding of how the experimental parameters affect nanoparticles' hydrodynamic diameter, crystalline structure, and composition.

Rigorous control was maintained throughout the processes, from synthesis to characterization, aiming to reduce errors in DOE responses related to equipment, reagents masses variations, and methods of working.

Iron (II) chloride tetrahydrate ($FeCl_2 \cdot 4H_2O$ >99%, Sigma-Aldrich) and iron (III) chloride hexahydrate ($FeCl_3 \cdot 6H_2O$ >97%, Dinâmica) were used as the source of ferrous and ferric ions, respectively. Sodium hydroxide (NaOH >97%, Fmaia) was applied as an alkaline agent for iron precipitation. The glassware was washed with hydrochloric acid (HCl) 50% v/v in deionized water for removing spurious contaminations. Deionized water (18.2 Ωm) purified by a Sartorius arium® comfort system was used throughout the experiments.

1.2.1 Plackett-Burman factorial design for the experimental procedures

To determine the most relevant factors over IONPs size and composition, the Plackett-Burman factorial design was created in a trial version of Minitab v. 1.7. In this context, seven input factors with two levels each were defined, as described in Table 1.2.

Table 1.2 – Factors and levels applied for the factorial design creation and informed in Minitab as input, for randomization. The experimental conditions to be investigated by DOE were defined according to the literature.

Factor abbreviation	Meaning	Minimum level	Maximum level
Fe^{2+}/Fe^{3+}	Molar ratio between ferrous and ferric ions	0.5	0.9
SR	Stirring rate	104.72 $rad.s^{-1}$	188.49 $rad.s^{-1}$
Temp	Temperature	293.15 K	371.15 K
AGA	Speed of alkaline agent addition	2 $mL.min^{-1}$	instantaneous
Fe/OH	The molar ratio between the total quantity of iron and alkaline agent	0.3	0.5
RT	Reaction time	1800 s	3600 s
TQI	The total quantity of iron	0.100 mol	0.150 mol

1.2.2 Synthesis of bare iron oxide nanoparticles

Based on the runs proposed by the Plackett-Burman method, twelve samples of IONPs were prepared (namely S-1 to S-12). Trivial calculations indicated the required masses of $FeCl_2 \cdot 4H_2O$ and $FeCl_3 \cdot 6H_2O$, which were solubilized in deionized water for a final volume of 50 mL each. Iron chloride solutions were mixed in a round-bottom flask and homogenized in a magnetic stirrer hotplate (Fisatom, 752A), at 104.72 or 188.49 $rad.s^{-1}$. A condensing system was used to preserve the volume constant. The experiments were carried out at room temperature (293.15 K) or 371.15 K. For precipitation of the oxides, 50 mL of sodium hydroxide solution were abruptly added to the iron solution (the entire volume at once) or slowly, at a rate of 2 mL. min^{-1} by a titrator 848 Titrino Plus, Metrohm. The concentration of the alkaline agent was defined based on the

reaction parameter Fe/OH ratio. The reaction time of 1800 or 3600 seconds was counted after adding the precipitant solution. The samples prepared under heating were cooled down to room temperature before purification processes. Figure 1.13 shows the experimental setup.

Figure 1.13 – Experimental set-up for coprecipitation of iron oxide nanoparticles, based on the runs suggested by DOE.

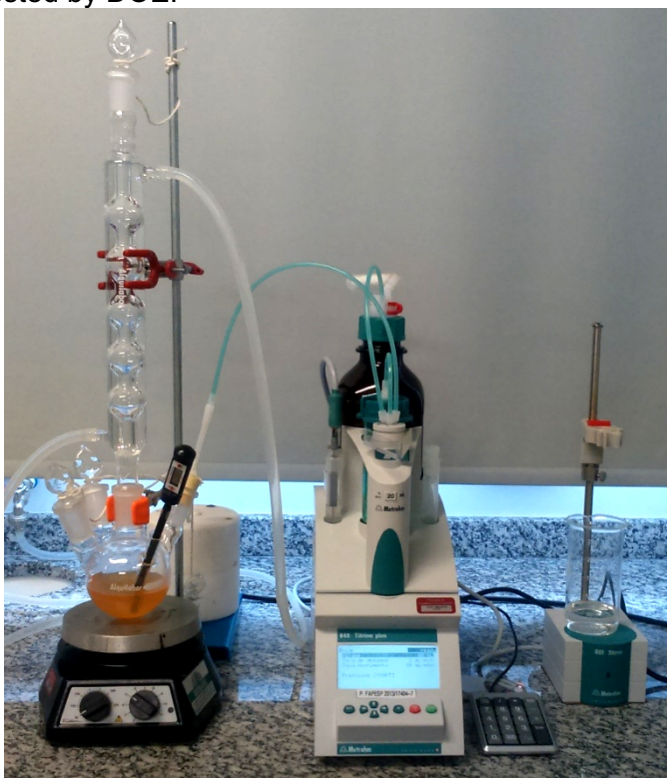

Reference: Author.

1.2.3 Samples characterization

All samples were diluted (30 µL of iron oxide particles in 1,500 µL of deionized water) and centrifuged at 2,500 rpm and 20ºC in a Heraeus Multifuge X1R centrifuge (Thermo Scientific) for 5 minutes for removing larger particles aggregates. Based on the coefficient of diffusion calculated from the Stokes-Einstein Equation (Equation 1.6) (EINSTEIN, 1905; HUNTER, 2013), the hydrodynamic diameter of IONPs was achieved. For such purpose, 14 runs of 10 seconds were completed in a Zetasizer Nano ZS-90 (Malvern) in a DTS0012 cuvette, at an angle of 90º.

$$D = \frac{RT}{N_A 6\pi\eta\alpha}$$ Equation 1.6

Where D = coefficient of diffusion, R = gas constant per mole, T = absolute temperature, N_A = Avogadro constant, η = viscosity of the liquid carrier, and α = hydrodynamic radius of the sphere.

As long as the objective was to evaluate the overall influence of experimental parameters over particles composition, the samples, were analyzed by XRD without being washed in deionized water. Because bare IONPs were synthesized and no additional stabilizing steps were performed, the nanoparticles settled out over time; then, 10 mL of the pellet were pipetted to Petri dishes and completely dried at room temperature. The X-ray diffractometer XRD-6000 (Shimadzu) was used, along with Cu-Kα (λ = 154439 Å) and reference codes, from ICCD, 34-1266 (akaganeite), 33-0664 (hematite), 39-1346 (maghemite), 05-0628 (sodium chloride), 19-0629 (magnetite) and 29-0713 (goethite). The data were treated and interpreted in the software X'Pert High Score Plus which was also used for the Rietveld method, which provided the percentage of magnetite per sample.

FTIR analyses were made using the dried powder of IONPs in ATR mode of Spectrum 400, Perkin Elmer with spectral resolution 4 cm^{-1}. The spectra were collected at the Mid-Infrared region (4000 – 400 cm^{-1}).

The responses of each sample, S-1 to S-12, obtained from DLS, XRD, and FTIR data were described in Minitab v. 1.7 and the relationship among the factors, levels, and particles characteristics was achieved. Figure 1.14 shows the flowchart that was designed for a better understanding of DOE.

Figure 1.14 – Flowchart of the IONPs syntheses process: factorial design by DOE, coprecipitation of the magnetic nanoparticles, and the obtainment of a reliable protocol.

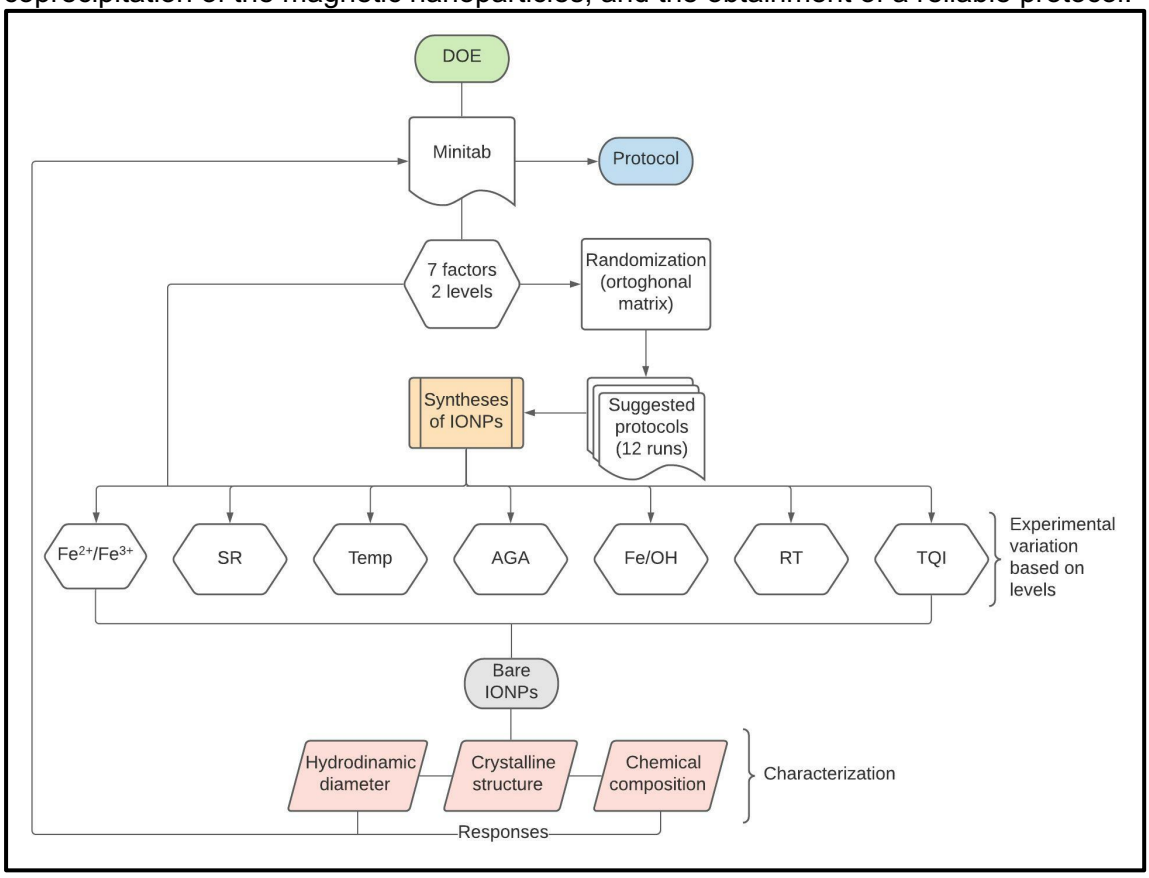

Reference: Author.

1.3 RESULTS AND DISCUSSION

1.3.1 Hydrodynamic diameters

Table 1.3 - Experimental protocols suggested by Plackett-Burman filtration and applied to 12 runs of IONPs synthesis.

Run	**S-1**	**S-2**	**S-3**	**S-4**	**S-5**	**S-6**
Fe^{2+}/Fe^{3+}	0.5	0.9	0.5	0.5	0.9	0.9
SR ($rad.s^{-1}$)	104.72	188.49	188.49	104.72	188.49	104.72
Temp (K)	293.15	293.15	293.15	293.15	293.15	293.15
AGA	fast	fast	slow	slow	fast	slow
Fe/OH	0.5	0.3	0.3	0.3	0.5	0.5
RT (s)	3,600	1,800	3,600	1,800	1,800	3,600
TQI (mol)	0.100	0.100	0.150	0.100	0.150	0.150
Run	**S-7**	**S-8**	**S-9**	**S-10**	**S-11**	**S-12**
Fe^{2+}/Fe^{3+}	0.5	0.9	0.9	0.9	0.5	0.5
SR ($rad.s^{-1}$)	188.49	104.72	188.49	104.72	104.72	188.49
Temp (K)	371.15	371.15	371.15	371.15	371.15	371.15
AGA	fast	slow	slow	fast	fast	slow
Fe/OH	0.3	0.3	0.5	0.3	0.5	0.5
RT (s)	3,600	1,800	3,600	3,600	1,800	1,800
TQI (mol)	0.150	0.150	0.100	0.100	0.150	0.100

Reference: (ROST *et al.*, 2019).

In the initial steps of this work, one of the main difficulties was to synthesize magnetite nanoparticles with nanoscale dimensions. For this reason, the Plackett-Burman filtration method was used for designing the experiments. The factors and levels which most probably could affect nanoparticles' size and composition were defined according to the literature. Then, these parameters were randomized by DOE algorithms in an orthogonal matrix, using the software Minitab. Afterward, twelve experimental runs were carried out to synthesize

IONPs by coprecipitation in alkaline media, following the conditions described in Table 1.3.

For collecting the responses of each run, the hydrodynamic diameter was measured by DLS. Then, the size of each sample was inserted in the Minitab project table, which was used by the software to calculate the main effects.

The main effects plot suggested in Figure 1.15 estimates the most relevant factors over particles diameter. The dashed horizontal line marks the edge of relevance. As larger the distance between the two blue dots, distinct by the blue line, the more important is the factor in the response. The relevance of each parameter is associated with the angle between the blue and the dashed line. As this angle approximates to zero, lesser is the relevance of a given factor.

Figure 1.15 – Main Effects Plot for nanoparticles size, obtained from the response (hydrodynamic diameter) of the experimental runs.

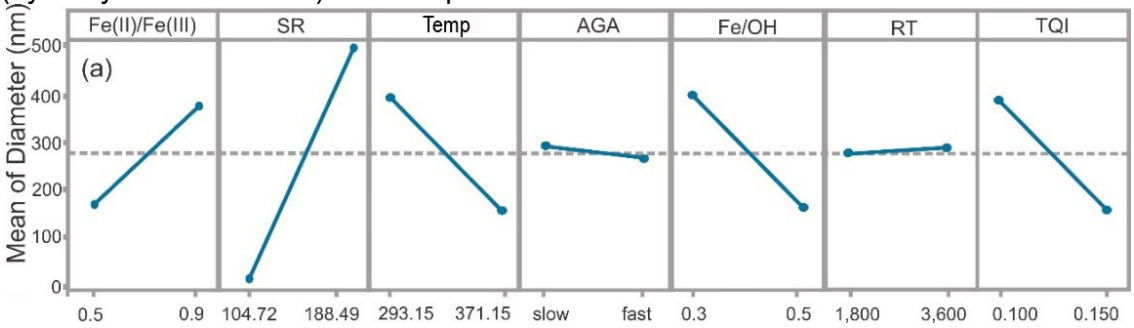

Reference: (ROST *et al.*, 2019).

The factors with main effects over particles diameter were SR, Fe^{2+}/Fe^{3+}, Temp, Fe/OH, and TQI. It is straightforward to note that smaller diameters are easier to be achieved when using $Fe^{2+}/Fe^{3+} = 0.5$, SR = 104.72 $rad.s^{-1}$, Temp = 371.15 K, AGA = irrelevant, but fast addition eliminates the use of Titrino, Fe/OH = 0.5, RT = irrelevant, TQI = 0.150 mol.

The average size increases proportionally to pH and is also pertinent to the nature of the alkaline agent; stronger basic solutions cause more deprotonation of iron ions and consequently, the formation of larger particles (JAYAKUMAR, 2007). Then, it was expected that the maximum level of Fe/OH (less amount of alkaline agent) could lead to smaller particles, which was in agreement with the main effects plot from the Design of Experiments. Indeed, the smaller particles (S-1, S-11, S-12) were synthesized with Fe/OH=0.5.

The largest particles (S-2 and S-6) were produced with Fe^{2+}/Fe^{3+}=0.9. The main effects plots are in agreement with Karaagac and Kockar (2012). Those authors had found that this factor affects the nucleation of iron oxide nanoparticles. In this context, at the higher molar ratio between ferrous and ferric ions, the quantity of nuclei is limited. In this way, during the growth stage larger particles are acquired (KARAAGAC; KOCKAR, 2012b)

The data were classified into four different groups according to similar characteristics of the composition, which will be discussed later. It is known that the conditions of reactions directly influence nanoparticles size distribution due to nucleation and growth of crystals. Materials with different size populations arise from processes in which both steps occur simultaneously (LIM *et al.*, 2013). Intensity distributions are shown in Figure 1.16.

Figure 1.16 – Size distributions of IONPs plotted by the intensity of scattered light (collected by DLS).

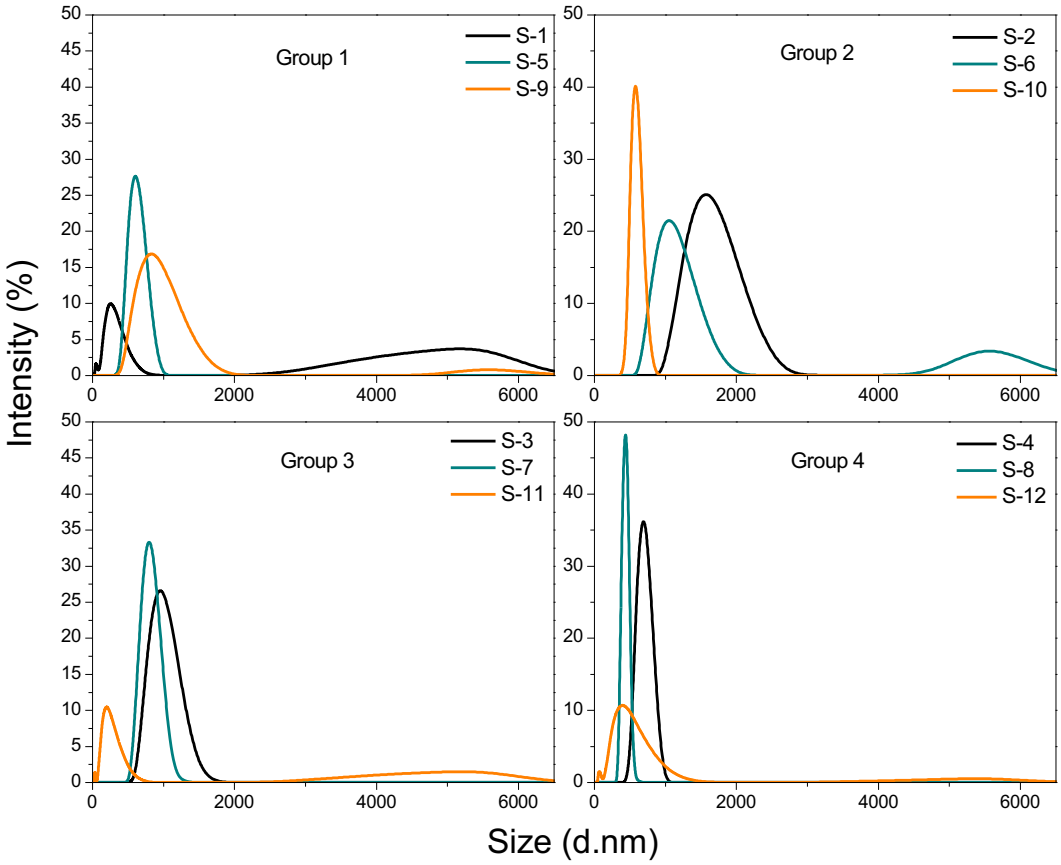

Reference: Author.

According to Figure 1.16, the samples presenting only one intensity band related to hydrodynamic diameter were S-5 (612 ± 108.3 nm), S-2 (1614 ± 320.3 nm), S-10 (586 ± 65.92 nm), S-3 (978 ± 184.6 nm), S- 7 (800 ± 113.6 nm), S-4 (692 ± 86.92 nm) and S-8 (434 ± 33.12 nm). These considerations indicate that the protocols used for obtaining those samples favor more uniformity during the development of nuclei, in a stage separated from growth. However, according to the polydispersity index (PDI) values (S- 5: 0.650, S-2: 0.313, S-10: 0.764, S-3: 0.343, S-7: 1.000, S-4: 0.674, and S- 8: 0.894), no sample was monodisperse. The monodispersity is achieved when PDI ≤ 0.200. As indicated by the effects plots (Figure 1.15), the factors and levels which should be favorable to the formation of smaller nanoparticles were lowest Fe^{2+}/Fe^{3+} and ST, highest Temp, Fe/OH, and TQI. The sample S-2 presented the biggest dimension (1614 nm), which corroborates the fact that the conditions of this particular run were unfavorable to the production of smaller nanoparticles. All the other samples presenting only one intensity band were produced with at least two factors appropriate to size reduction. Among them, the smallest nanoparticles (S- 8, 434 nm) were originated from an experiment performed with three factors at levels required to minimize the hydrodynamic diameter. Only three out of seven samples presenting a unique intensity band were obtained with reliable results, with correlogram matching the International Standard on Dynamic Light Scattering, ISO 13321 (1996) (ISO, 1996). This correlation is confirmed in the equipment, as a good quality report.

Overall, the samples containing multiple diameter populations had smaller sizes. The hydrodynamic diameters at the most representative intensities were S-1 (284 ± 122.5 nm), S-9 (876 ± 270.8 nm), S-6 (1101 ± 249.9 nm), S- 11 (232 ± 110.4 nm), and S-12 (453 ± 218.5 nm). The experiment that produced the smallest particle (S-11) was conducted under all factors and levels required for the lowest diameter. It is noteworthy that, excluding the sample with the biggest size (S-6), all these results were collected with a good quality report, following the ISO criteria. However, all those samples also consisted of second population size and, in all cases, were bigger than 4,000 nm. The PDI were found to be S-1: 0.590, S-9: 0.255, S-6: 0.419, S-11: 0.392 and S-12: 0.282.

Although no sample had shown the highest intensity band at the nanoscale (<100 nm), neither monodispersity (PDI < 0.200), the correlograms of S-1, S-2,

S-3, S-9, S-11, and S-12 were fitted in the ISO 13321. Additionally, the PDI of those samples was lower than 0.600. These findings support the interpretation by number distribution. It is important to follow such requirements because this type of data is derived from the intensity of light scattering (the preliminary result shown in the DLS technique), applying the Mie theory. For better data visualization, the intensity distributions of this set are illustrated again in Figure 1.17.

Figure 1.17 – Intensity distribution of the samples obtained with a good quality report and PDI < 0.600; zoom-in highlights the region of nanoscale.

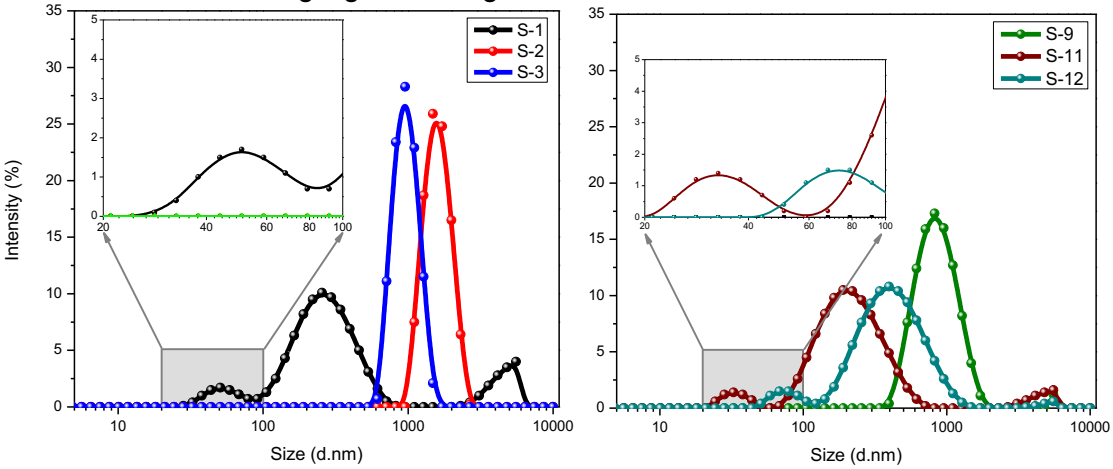

Reference: Author.

Irrespective of the fact that the light scattering bands of nanoparticles within 100 nm were not the most intense, S-1, S-11, and S-12 had shown some contribution at the nanoscale region, although those bands did not achieve even 5% of the scattered light. In this case, if more detail about the smaller particles is required, the number distribution can be explored. The number distribution of S- 1, S-11, and S-12 is depicted in Figure 1.18 for emphasizing the smaller particles achieved by DOE randomization.

Figure 1.18 - Number distribution of the samples obtained with a good quality report. Region A represents nanoscale and Region B microscale.

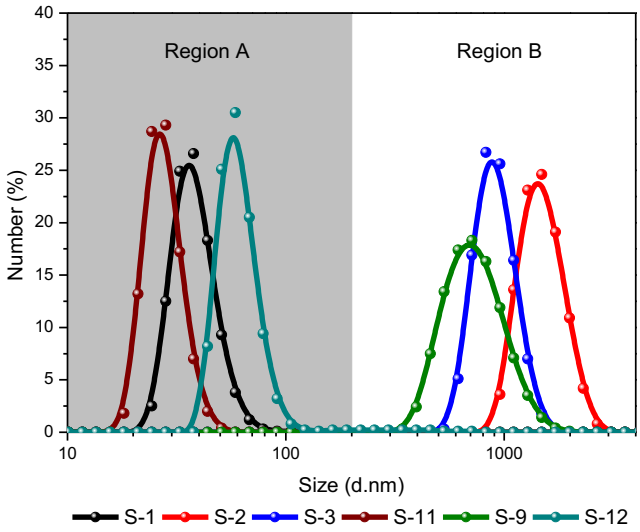

Reference: (ROST *et al.*, 2019).

Figure 1.19 – Schematic representation of the intensity-number distribution of size measured by DLS. Red arrows represent light scattering. Bigger particles scatter more light, therefore the bands relative to them are higher in intensity distribution. Therefore, the number of smaller particles can be more significant.

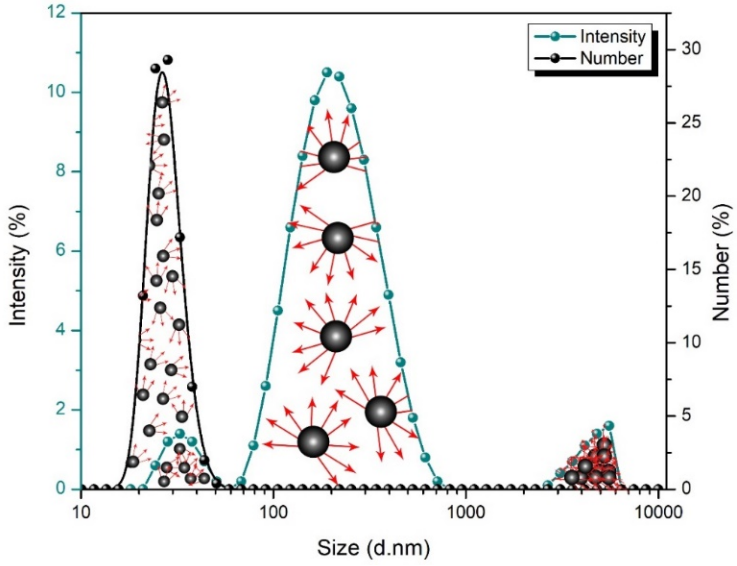

Reference: Author.

Figure 1.18 confirms that even though S-1 (100% corresponds to particles with 39 nm), S-11 (28 nm, 99.8%), and S-12 (61 nm, 97.9%) were produced with multiple size populations, nanoparticles were obtained in higher numbers than bigger particles. Moreover, bigger particles were formed in such insignificant amounts that are not shown in the number distribution. However, the intensity of

scattered light was higher at bigger hydrodynamic diameters because larger particles tend to scatter more light than the smaller ones, as schematically represented by Figure 1.19.

It is straightforward that DOE was useful for tracking the effects of factors and levels over bare IONPs hydrodynamic diameter. The absence of stabilizer agents led to visible sedimentation over time and broad size distribution. Results of nanoparticles peptized with TMAOH will be presented in Chapter 2.

1.3.2 Crystalline structure

XRD was used for investigating the crystalline structure of the different oxides produced per batch of nanoparticles. Rietveld refinement was applied to quantify the percentage of magnetite. As a complementary technique, FTIR spectra of all samples were collected to confirm the chemical bonds of iron oxides, especially the absorption band related to magnetite. The responses of each batch were added to the Minitab project to relate the factors and levels to the percentage of magnetite per randomized run. Figure 1.20 gives the main effects plot on magnetite formation. Figure 1.21 depicts the spectra and diffractograms of all samples, which were separated into four groups according to similarities in absorption bands and peaks.

Figure 1.20 - Main Effects Plot for nanoparticles crystalline structure, obtained from the response (magnetite percentage) of the experimental runs.

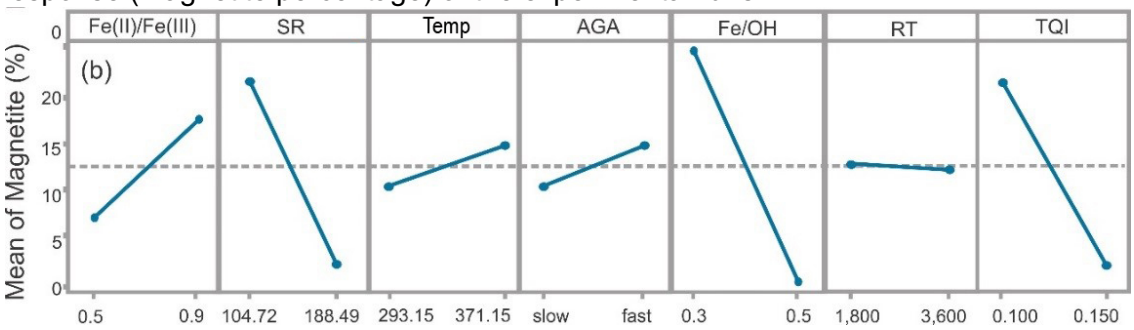

Reference: (ROST *et al.*, 2019).

Figure 1.21 – IONPs separated into groups according to similar characteristics: (a) FTIR spectra and (b) XRD diffractograms.

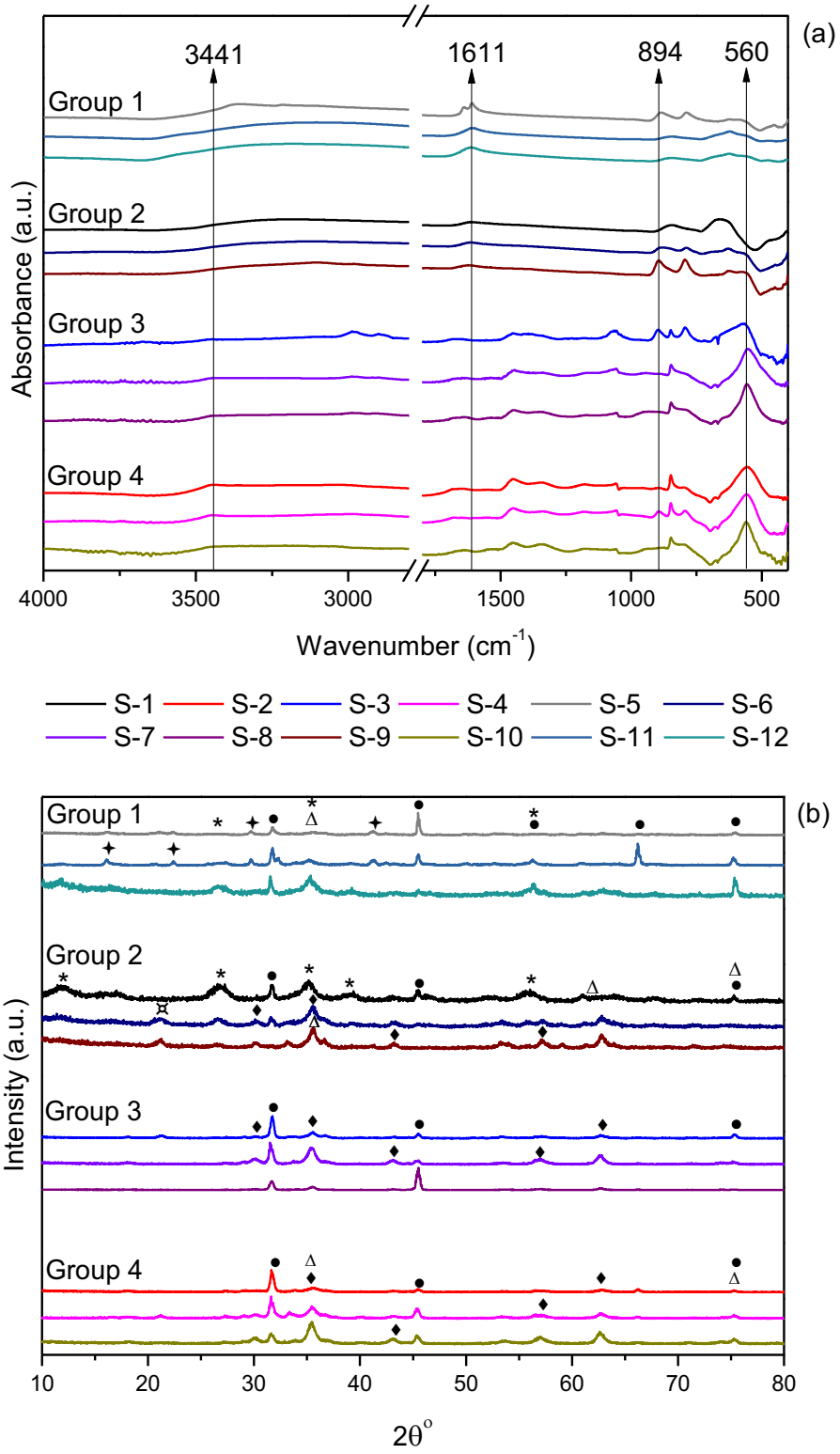

✦= excess of Fe^{2+},* = β-FeOOH, Δ = α-Fe_2O_3,

□ = ɣ-Fe_2O_3, ¤ = α-FeOOH, ♦ = Fe_3O_4 and • = NaCl

Reference: (ROST *et al.*, 2019).

The parameters Fe/OH, SR, TQI, and Fe^{2+}/Fe^{3+} were the most relevant over magnetite % and varying RT was insignificant. According to the main effects plot, the protocol favorable to the highest percentage of magnetite would be Fe^{2+}/Fe^{3+} = 0.9, SR = 104.72 rad.s^{-1}, Temp = 371.15 K, AGA = fast, Fe/OH = 0.3, RT = irrelevant, but reacting for 1,800 s can save time in experiments, TQI = 0.100 mol. These conditions match the protocol S-10; which produced 70% of magnetite, the highest percentage observed in this study. The highest temperature was beneficial to magnetite formation, which agrees with the fact that the O_2 solubility is controlled (GILBERT *et al.*, 2008).

The samples presented an excess of sodium chloride that arises from the coprecipitation reaction (as a reminder, sodium hydroxide was the alkaline agent), which is the reason why peaks of NaCl were identified in all diffractograms. This sub-product formed by ionic bonds was not detected by FTIR because the technique characterizes covalent bonds, but the crystal structure is easily identified by XRD (marked by solid black spheres in Figure 1.21 (b)).

The OH bending at iron oxide's surface was detected at 3441 cm^{-1}. The IR absorption band at 560 cm^{-1} is characteristic of Fe-O vibrations in magnetite structure and was found in S-2, S-4, S-8, and S-10 spectra. (SKLUTE *et al.*, 2018). Magnetite structure was further confirmed at 30, 35.3, 43.1, 57.0, and 62.6 θ XRD peaks. The quantification made by Rietveld had shown 14.0%, 43.0%, 16.0 % and 70.0% of magnetite in S-2, S-4, S-8 and S-10, respectively. The effects plots (Figure 1.20) demonstrates that Fe/OH=0.3 improves the percentage of magnetite, corroborating with the results presented by Ahn *et al*. (2012) (AHN *et al.*, 2012). The samples synthesized with Fe/OH=0.3 (groups 3 and 4) had shown the absorption band at 560 cm^{-1}. On the other hand, the IR vibration typical of magnetite was not found in the spectra of IONPs prepared with Fe/OH=0.5 (groups 1 and 2), which confirms that this condition avoids Fe_3O_4 formation. At lower wavenumbers, tracers of goethite were found at 447 cm^{-1} in S-6, S-9. Akaganeite was identified at 473 cm^{-1} for S-11. The reaction pathways of coprecipitation method led to the production of multiple oxides, as represented in Figure 1.22. Additionally, the experiments were carried out under non-inert atmosphere.

Figure 1.22 – Schematic representation of reaction pathways that originates different iron oxides during coprecipitation in alkaline media.

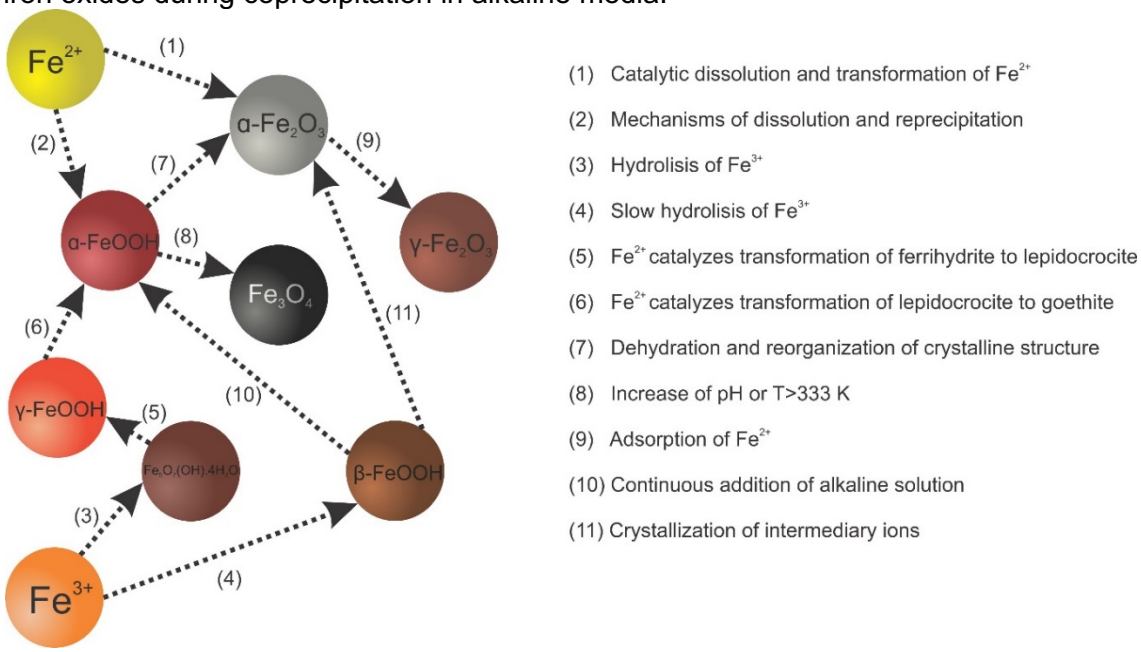

Reference: (ROST *et al.*, 2019).

Akaganeite can be obtained by hydrolysis of Fe^{3+} ions and is the precursor of some reactions. The IR band at ~ 845 cm^{-1} was found in all samples from groups 3 and 4. The 1611 cm^{-1} band was present in all spectra from group 1 and characterized some traces in group 2 (RAMAN *et al.*, 1991; SKLUTE *et al.*, 2018). The XRD peaks at 12, 26.8, and 35.3 θ confirmed akaganeite in S-1, S-11, and S-12, which indicates higher Fe^{3+} hydrolysis in these protocols.

Goethite arises from the combination of akaganeite and slow addition of the alkaline agent or due to excess hydroxyl groups, which is caused by varying the molar ratio between reactants. Additionally, this oxide can also be obtained when dissolution and re-precipitation of the ions precursors occurs. The topotactic transformation of goethite leads to magnetite arrangement. Temperature higher than 333 K also supports magnetite structure because this condition controls the solubility of O_2. The bands related to goethite were identified at 626 cm^{-1} (S-11 and S-12), 788 cm^{-1} (S-5, S-6, and S-9), and 883 cm^{-1} (S-5). The absence of goethite bands in S-2, S-4, S-8, and S-10 spectra suggested the complete transformation of this structure in magnetite.

Hematite organization assembles from rearrangement of goethite because of dehydration processes. The nucleation of hematite benefits from the presence of akaganeite. In presence of ferrihydrite transformed by hydrolysis of Fe^{3+},

hematite is also formed. The hematite absorption bands were found at 628 cm^{-1} (traces in groups 1 and 2), 799 cm^{-1} (S-5, S-6 and S-9), 897 cm^{-1} (S-3, S-5 and S-9, traces in S-4), 1339 cm^{-1} (trace in S-10) and 1637 cm^{-1} (trace in S-5). The XRD peak at 35.5 θ was present in the diffractograms of S-4, S-6, S-9, and S- 10.

Lepidocrocite results from ferrihydrite transformation catalyzed by Fe^{2+} or by modifying ferrous ion concentration. The presence of IR bands at 1450 and 1175 cm^{-1} in all spectra from groups 3 and 4 implies that lepidocrocite was formed. Table 1.4 shows all the IR absorption attributions bands characterized from S-1 to S- 12.

Table 1.4 - IR bands attributed to iron oxides in each sample prepared based on the factorial design from DOE, along with the IR bands found in the literature.

Sample	**IR band (cm^{-1})**	**IR band (cm^{-1}) in the literature**	**Attribution**
S-6 S-9	**447**	**447,** (SKLUTE *et al.*, 2018)	Goethite (α-FeOOH)
S-11	**473**	**470,** (SKLUTE *et al.*, 2018)	Akaganeite (*β*-FeOOH)
S-12	**476**	**478,** (SKLUTE *et al.*, 2018)	Lepidocrocite (γ-FeOOH)
		480, (DEMIR *et al.*, 2015)	Hematite (α-Fe_2O_3)
S-7	**553**	**553,** (SKLUTE *et al.*, 2018)	Maghemite (γ-Fe_2O_3)
S-4 S-8	**559**	**560,** (SKLUTE *et al.*, 2018)	Magnetite (Fe_3O_4)
S-2 S-10	**560**	**560,** (SKLUTE *et al.*, 2018)	Magnetite (Fe_3O_4)
		563, (DEMIR *et al.*, 2015)	Maghemite (γ-Fe_2O_3)
S-3	**570**	**571,** (DEMIR *et al.*, 2015)	Hematite (α-Fe_2O_3)
S-5 S-9	**583**	**583,** (SKLUTE *et al.*, 2018)	Lepidocrocite (γ-FeOOH)
S-11 S-12	**623**	**626,** (SKLUTE *et al.*, 2018)	Hematite (α-Fe_2O_3) Goethite (α-FeOOH)

Sample	IR band (cm^{-1})	IR band (cm^{-1}) in the literature	Attribution
S-5	**623**	**626,** (SKLUTE *et al.*, 2018)	Goethite (α-FeOOH)
S-6 S-9	**627**	**626,** (SKLUTE *et al.*, 2018)	Hematite (α-Fe_2O_3) Goethite (α-FeOOH) Lepidocrocite (γ-FeOOH)
S-1	**660**	**661,** (SKLUTE *et al.*, 2018)	Hematite (α-Fe_2O_3)
S-5 S-6	**785**	**786,** (SKLUTE *et al.*, 2018)	Goethite (α-FeOOH)
S-3 S-9	**793**	**794,** (SKLUTE *et al.*, 2018)	Goethite (α-FeOOH)
S-4	**796**	**794,** (SKLUTE *et al.*, 2018)	Goethite (α-FeOOH)
		800, (DEMIR *et al.*, 2015)	Hematite (α-Fe_2O_3)
S-10	**800**	**800,**(DEMIR *et al.*, 2015)	Hematite (α-Fe_2O_3)
S-2 S-3 S-4 S-7 S-8 S-10 S-11 S-12	**849**	**845,** (SKLUTE *et al.*, 2018)	Akaganeite (β-FeOOH)
S-6	**877**	**873,** (DEMIR *et al.*, 2015)	Maghemite (γ-Fe_2O_3)
S-5	**885**	**883,** (SKLUTE *et al.*, 2018)	Goethite (α-FeOOH)
S-2 S-3 S-4 S-9	**894**	**897,** (DEMIR *et al.*, 2015)	Hematite (α-Fe_2O_3)
S-7	**944**	**940,** (HAKEEM *et al.*, 1986)	Goethite (α-FeOOH)
S-3	**1065**	**1064,** (RAMAN *et al.*, 1991)	Ferric hydroxide ($Fe(OH)_3$)

Sample	IR band (cm^{-1})	IR band (cm^{-1}) in the literature	Attribution
S-2 S-4 S-7 S-8 S-10	**1172**	**1176,** (WECKLER; LUTZ, 1998)	Lepidocrocite (γ-FeOOH)
S-7	**1337**	**1339,** (DEMIR *et al.*, 2015)	Hematite (α-Fe_2O_3)
		1333, (RAMAN *et al.*, 1991)	Ferric hydroxide ($Fe(OH)_3$)
S-2 S-4 S-10	**1341**	**1339,** (DEMIR *et al.*, 2015)	Hematite (α-Fe_2O_3)
S-3	**1403**	**1400,** (RAMAN *et al.*, 1991)	Akaganeite (β-FeOOH) Goethite (α-FeOOH)
S-7	**1446**	**1450,** (RAMAN *et al.*, 1991)	Lepidocrocite (γ-FeOOH)
S-2 S-3 S-4 S-7 S-8 S-10	**1450**	**1450,** (RAMAN *et al.*, 1991)	Lepidocrocite (γ-FeOOH)
S-8	**1533**	**1534,** (CHUKANOV; CHERVONNYI, 2016)	Akaganeite (β-FeOOH)
S-11	**1611**	**1615,** (RAMAN *et al.*, 1991)	Akaganeite (β-FeOOH) Feroxite (δ-FeOOH)
S-1 S-5 S-6 S-9 S-12	**1615**	**1615,** (RAMAN *et al.*, 1991; SKLUTE *et al.*, 2018)	Akaganeite (β-FeOOH)
S-5 S-7 S-8 S-10	**1635**	**1637,** (DEMIR *et al.*, 2015)	Hematite (α-Fe_2O_3)
		1635, (ORDOUKHANIAN *et al.*, 2016)	O-H combined to Fe (bending vibration)
S-2	**1649**	**1650,** (MUSIĆ *et al.*, 1986)	Goethite (α-FeOOH)
S-3	**1666**	**1667,** (RAMAN *et al.*, 1991)	Goethite (α-FeOOH)

Sample	IR band (cm^{-1})	IR band (cm^{-1}) in the literature	Attribution
S-9	**2982**	**2978,** (CHUKANOV; CHERVONNYI, 2016)	Akaganeite (β-FeOOH)
S-9 S-11	**3104**	**3100,** (HAKEEM *et al.*, 1986)	Fe(II)-OH in Goethite
S-6	**3117**	**3114,** (BIKIARIS *et al.*, 2000)	OH groups
S-2 S-4 S-8	**3439**	**3442,** (ORDOUKHANIAN *et al.*, 2016)	OH^- adsorbed on the iron oxide surface
		3438, (LI *et al.*, 2012)	Adsorbed water
S-7	**3446**	**3442,** (ORDOUKHANIAN *et al.*, 2016)	OH bending
		3442, (ORDOUKHANIAN *et al.*, 2016)	OH^- adsorbed on the iron oxide surface
		3450, (HAKEEM *et al.*, 1986)	OH and water
		3450, (MUSIĆ *et al.*, 1986)	Hematite (α-Fe_2O_3) Maghemite (γ-Fe_2O_3)

1.4 CONCLUSIONS

Based on effects plots from the experimental design, it was concluded that the stirring rate, temperature, the molar ratios Fe^{2+}/Fe^{3+} and Fe/OH, and total amount of iron are the most relevant factors over the hydrodynamic diameter of the particles. The speed at which the alkaline agent was added to the mixture of iron ions and the reaction time was not relevant over the samples size. Plackett-Burman technique led to the conclusion that smaller particles were obtained by coprecipitation in alkaline media when synthesized under Fe^{2+}/Fe^{3+} = 0.5, SR = 104.72 $rad.s^{-1}$, Temp = 371.15 K, Fe/OH = 0.5, and TQI = 0.150 mol. The sample that had shown the smallest hydrodynamic diameter (S-11) was synthesized with all factors and levels favorable to size reduction.

Concerning the percentage of magnetite per sample, significant influences were related to SR, TQI, Fe/OH, and Fe^{2+}/Fe^{3+}. In this context, the ideal protocol for magnetite formation was SR = 104.72 $rad.s^{-1}$, TQI = 0.100 mol, Fe/OH = 0.3, and Fe^{2+}/Fe^{3+} = 0.9. The protocol applied for S-10 corroborated such conditions and consequently, led to the highest percentage of magnetite found in this work (70 %). Nanoparticles with smaller sizes and composed most of magnetite could be easier achieved if using SR = 104.72 $rad.s^{-1}$, T = 371.15 K and fast AGA.

It was concluded that Plackett-Burman is a powerful technique to estimate the most important experimental set-ups over nanoparticles characteristics. However, considering that multiple iron oxides were formed and also the polydispersity of IONPs produced in this work, along with the fact that those particles were sedimenting over time, the next steps were focused on surface stabilization.

Chapter 2: *Magnetic Particle Imaging Performance of Liposomes Encapsulating Iron Oxide Nanoparticles*

Journal of Magnetism and Magnetic Materials 504 (2020) 166675

Contents lists available at ScienceDirect

Journal of Magnetism and Magnetic Materials

journal homepage: www.elsevier.com/locate/jmmm

Magnetic particle imaging performance of liposomes encapsulating iron oxide nanoparticles

N.C.V. Rost[a], K. Sen[b], S. Savliwala[b], I. Singh[b], S. Liu[b], M. Unni[b], L. Raniero[a], C. Rinaldi[b,c,*]

[a] *Laboratório de Nanossensores, Instituto de Pesquisa e Desenvolvimento, Universidade do Vale do Paraíba, Av. Shishima Hifumi, 2911 - 12244-000 São José dos Campos, Brazil*
[b] *Department of Chemical Engineering, University of Florida, P.O. Box 116005, Gainesville, FL 32611-6005, USA*
[c] *J. Crayton Pruitt Family Department of Biomedical Engineering, University of Florida, P.O. Box 116131, Gainesville, FL 32611-6131, USA*

ARTICLE INFO

Keywords:
Iron oxide nanoparticles
Magnetoliposomes
Magnetic particle imaging
MPI

ABSTRACT

Magnetic Particle Imaging (MPI) is a new imaging modality that quantifies spatial distribution of superparamagnetic iron oxide nanoparticles in a field of view through their non-linear magnetization response to an applied magnetic field. Liposomes loaded with magnetic nanoparticles (magnetoliposomes) are potential theranostic drug carriers that can combine magnetic properties with drug carrier ability. Prior work suggests that MPI signal can be affected by dipolar interactions between magnetic nanoparticles in close proximity – for instance, in a polymer matrix. Here we evaluate if encapsulating magnetic nanoparticles in liposomes has an impact in their MPI performance. For this purpose, magnetoliposomes were prepared using charge-stabilized iron oxide nanoparticles (IONPs) and their physical, magnetic and MPI properties were characterized. Interestingly, encapsulation of IONPs in magnetoliposomes led to an increase in MPI signal per unit mass.

1. Introduction

Magnetic particle imaging (MPI) is a new imaging technique that relies on the non-linear superparamagnetic response of magnetic nanoparticles, enabling high sensitivity quantitative and tomographic imaging of their distribution. Some of the unique features in MPI include negligible tissue background, negligible signal attenuation with tissue, and no ionizing radiation [1,2]. MPI first reported in 2005 by Gleich and Weizenecker [3,4] has found applicability in cancer imaging [4], assessment of aneurism hemodynamics [5], quantification of vascular stenosis [6], monitoring transplantation, biodistribution and clearance of stem cells *in vivo* [7], evaluating bleeding in traumatic brain injury [8] and tracking superparamagnetic iron oxide nanoparticles (SPIONs) biodistribution [9]. Ferucarbotran consists of small (4.2 nm) polycrystalline iron oxide nanoparticles in a carboxydextran matrix with hydrodynamic diameter of ~60 nm [10–12]. It has been suggested that interactions between the IONPs in the carboxydextran matrix result in improved MPI performance, to the point that Ferucarbotran is widely used by the MPI community [13].

Liposomes loaded with iron oxide nanoparticles (IONPs), so-called magnetoliposomes (ML) [14], are attractive as theranostic platforms [15] because of the possibility of transporting therapeutic molecules combined with the imaging and heating properties of IONPs. Furthermore, the composition can be made to be similar to cell membranes and it is possible to functionalize their surface with targeting molecules [16]. While ML have been extensively studied in the context of drug delivery and MRI, their use as a tracer for MPI remains relatively unexplored. However, ML behavior might be comparable to Ferucarbotran. The closed packing of IONPs in liposomes may change particles interactions and make them better for MPI.

Maruyama et al (2016) reported thermosensitive ML containing calcein or doxorubicin (DOX), and evaluated their potential as MPI tracers, drug delivery vehicles and agents for magnetic hyperthermia. The results indicated the usefulness of MPI for visualizing magnetic thermosensitive liposomes and monitoring drug release caused by hyperthermia [17]. However, these authors characterized the MPI performance of their ML using a prototype scanner that operates at a drive field frequency of 400 Hz and drive field amplitude of 20 mT [17,18]. In contrast, commercially available MPI scanners operate at higher frequencies of 25 kHz for the Bruker system and 45 kHz for the Magnetic Insight Momentum imager, and at lower excitation field amplitude of up to 16 mT for both systems, which will have an effect on the MPI signal intensity and resolution, owing to the response of magnetic nanoparticles to external magnetic fields [19]. As an example, during MPI-guided hyperthermia, Tay et al. (2018) observed negligible tumor heating at a frequency of 20 kHz, whereas at 354 kHz all tissues

* Corresponding author at: Department of Chemical Engineering, University of Florida, P.O. Box 116005, Gainesville, FL 32611-6005, USA.
E-mail address: carlos.rinaldi@ufl.edu (C. Rinaldi).

https://doi.org/10.1016/j.jmmm.2020.166675
Received 30 November 2019; Received in revised form 18 February 2020; Accepted 26 February 2020
Available online 27 February 2020
0304-8853/

2.1 LITERATURE REVIEW

2.1.1 Magnetoliposomes

Liposomes are vesicles composed of phospholipids, which means structures similar to cell membranes; this configuration confers biocompatibility, biodegradability, and inert biological activity. Further, considering the amphiphilic feature of such phospholipids achieved by a polar head group and two non-polar hydrocarbon tails, the liposomal compartments are useful for encapsulating hydrophobic and hydrophilic substances, as schematized in Figure 2.1. Indeed, these vesicles are potential drug delivery candidates. For instance, Doxil manufactured by Ortho Biotech, 1995 and ThermoDox from Celsion, 2013 are FDA-approved liposomes formulations, both loaded with doxorubicin. The former is a PEGylated product for treating ovarian cancer and the latter is a heat-activated liposome for breast and primary liver cancer (ALBERTS *et al.*, 2002; KAMMARI *et al.*, 2017).

Figure 2.1 – Representation of liposomes structure, assembled by the hydrophilic tail and hydrophobic head of phospholipids.

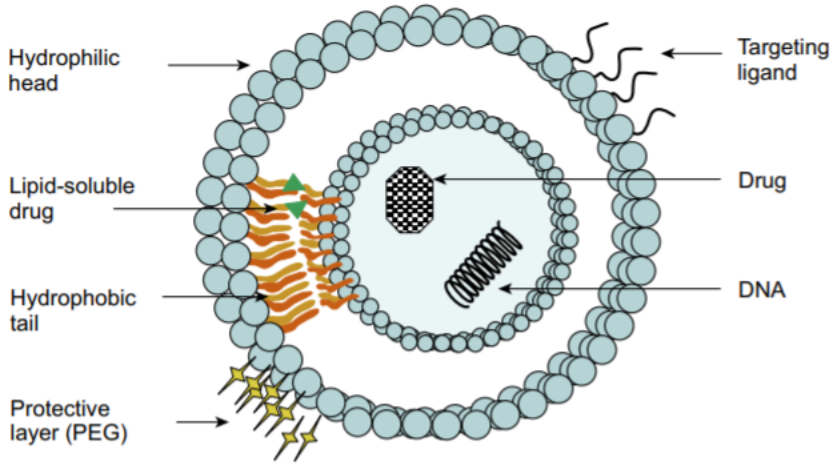

Reference: (KAMMARI *et al.*, 2017)

Among the techniques for liposomes formation, hydration provides spontaneous arrangement, as shown in Figure 2.2. Initially, the phospholipid and hydrophobic cargo are dissolved in an organic solvent, which must be completely evaporated in a rotary evaporator, for example. This step forms a thin film of a phospholipid, which is hydrated with aqueous media containing the required hydrophilic substances. In this step, the solution used for hydration must be at a

temperature above the phospholipid transition. The self-assembly of liposomes occurs because of the hydrophobic characteristic of the tail region combined with lipids hydration in an aqueous medium (KAMMARI *et al.*, 2017). The freeze-thaw method is usual when decreasing the vesicles lamellarity is desired (SRIWONGSITANONT; UENO, 2010). Extrusion, homogenization, and sonication are alternatives of downsizing steps to control the size distribution of the final formulation. The formation of sealed and stable compartments is inherent to the self-association of phospholipids layers, which occurs when the thin film contacts the aqueous phase or during the application of an external force (stirring or sonication) that cause layers disruption. Once the hydrocarbon tails are not exposed to water, the closure of liposomes is energetically favorable (ALBERTS *et al.*, 2002; KAMMARI *et al.*, 2017).

Figure 2.2 - Schematic representation of liposomes formation by thin-film hydration method.

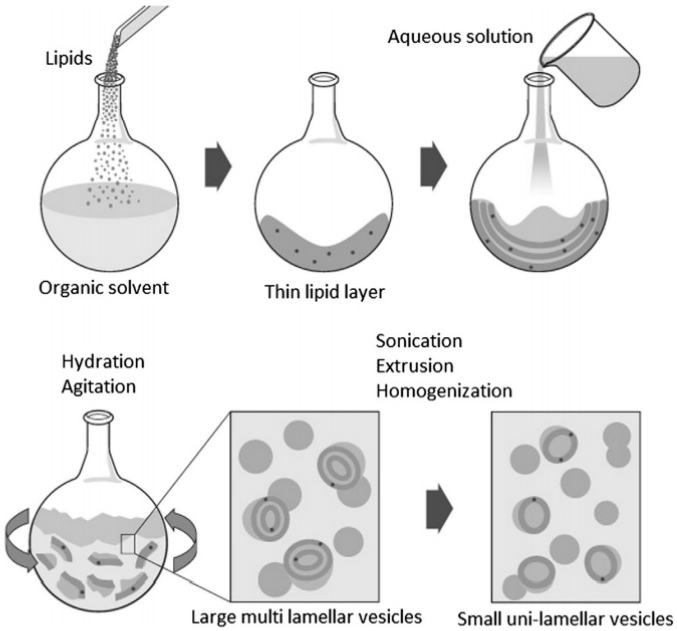

Reference: (KAMMARI *et al.*, 2017).

In 1988, De Cuyper and Joniau incubated pre-formed liposomes with magnetite nanoparticles synthesized by coprecipitation and stabilized by lauric acid. Supported by adsorption isotherms and electron micrograph data, these authors had found that the iron core was covered by a phospholipid bilayer due to adsorption of the charged head-groups on the iron surface. This was the first

time in which magnetoliposomes were reported, defined as “phosphatidylglycerols adsorbed onto magnetizable solid particles (DE; JONIAU, 1988).” Among the methods for entrapping SPIONs in the vesicular configuration of liposomes, hydration provides a higher probability of encapsulation because the nanoparticles interact directly with the inner phospholipid layer (SANTHOSH *et al.*, 2015). Additionally, not only SPIONs but also liposomes are FDA approved, which simplifies the clinical evolution of magnetoliposomes. As exemplified in Figure 2.3, both hydrophilic and hydrophobic SPIONs can be incorporated inside liposomes, in the aqueous lumen, or the lipid bilayer, respectively. However, as the nanoparticles are usually larger than the liposomes membrane thickness, distortion may takes place when encapsulating hydrophobic materials. (AMSTAD *et al.*, 2011; KRALJ *et al.*, 2017).

Figure 2.3 – Hydrophobic or hydrophilic SPIONs and drug localization in liposomes.

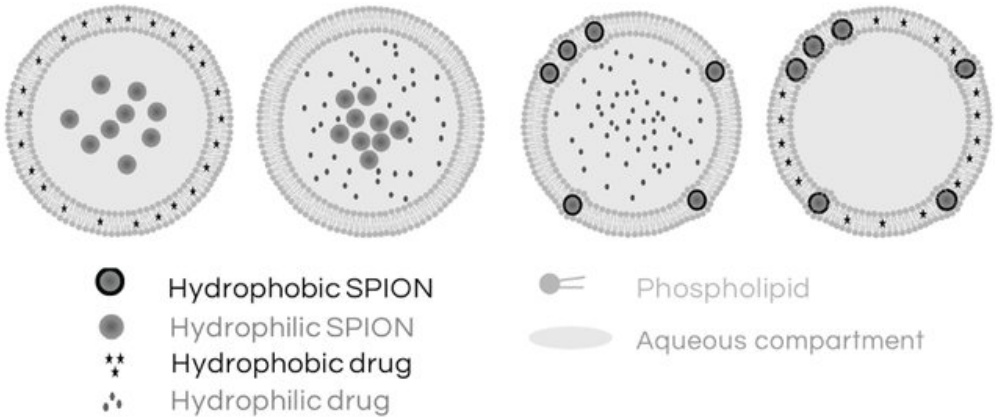

Reference: (KRALJ *et al.*, 2017).

The coating of nanoparticles with zwitterionic molecules, such as the phospholipid 1,2-distearoyl-*sn*-glycero-3-phosphocholine (DSPC), is a good alternative for reducing or even inhibit protein corona formation. One of the main efforts of nanomaterials *in vivo* applications is to avoid this shielding effect (RAHMAN *et al.*, 2015). The scientific relevance of magnetoliposomes comprises the versatility for applications demanding non-invasive control, imaging tools, magnetic targeting, and triggered drug release under alternating magnetic field exposure (AMSTAD *et al.*, 2011; KRALJ *et al.*, 2017). Upon the consideration that the lipid composition determines the membrane melting point and consequently, the permeability, the cargo can be released when the liposomes

are heated above the phospholipid melting point. Thermoresponsive delivery vehicles can thus be created to release the drug in conditions close to body temperature, as applied in magnetic fluid hyperthermia (AMSTAD *et al.*, 2011).

2.1.2 Magnetic properties of iron oxide nanoparticles

For any study on IONPs, understanding the magnetic properties is of paramount importance, because the usability depends on how rapidly the nanoparticles' dipole changes the orientation under magnetic fields (VAN RIJSSEL *et al.*, 2015). Therefore, the magnetic domains of the materials must be upon consideration. First hypothesized by Pierre Weiss in 1907, the magnetic domains composes ferromagnetic solids and in each of them, atoms' magnetic moments are aligned to a fixed direction (ROSENSWEIG, 1985). The internal energy of bulk ferromagnets, such as nickel, cobalt, or iron, tends to be spontaneously minimized. Therefore, magnetic domains naturally take place in the material structure and each of those regions comprises magnetic moments aligned in the same direction. The defects in the crystalline structure, as vacancies or dislocations, originate domain walls that separate the magnetic domains by a thickness relied on crystallographic, energetic, and geometric factors. Because the probability of structural defects is higher as bigger the material, magnetic domain formation is more feasible in larger ferromagnets (THANH, 2012), as illustrated in Figure 2.4 (a) (DEMAS; LOWERY, 2011).

The scale reduction considerably changes the energetic stability derived from domains formation. This is one of the reasons why smaller particles are preferable to bulk for a bunch of applications. The size reduction implies the absence of domain formation when no magnetic field is applied (THANH, 2012). In this case, for particles smaller than a critical diameter (D_s), the sample presents single-domain and the magnetization is uniform in each of them, but the magnetic orientation randomly varies in different domains, (THANH, 2012; MOHAPATRA; LIU, 2018), as represented in Figure 2.4 (b) (DEMAS; LOWERY, 2011). Also, as an effect of nanoscale in ferromagnetic materials, nanoparticles were found to have demagnetization (H_c) values almost two orders of magnitude larger than bulk (MOHAPATRA; LIU, 2018).

Figure 2.4 – (a) Multidomain of ferromagnets particles and single-domain of superparamagnetic nanoparticles when no magnetic field is applied and (b) under magnetic field.

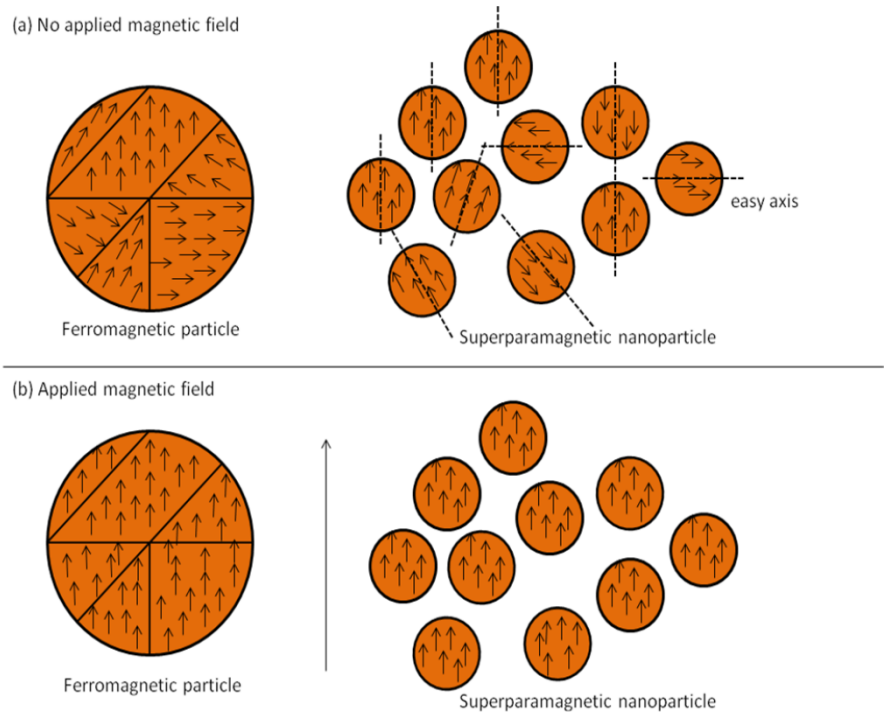

Reference: (DEMAS; LOWERY, 2011).

The superparamagnetism is usually observed in single-domain ferro- and ferrimagnetic nanoparticles, because those magnetic crystal does not have long-range order due to reduced size. One of the properties that arise from such circumstances is the relatively high magnetization and material saturation under low applied fields. Additionally, no net remanent magnetization is retained in superparamagnetic nanoparticles after removing the applied field. This characteristic happens because the magnetization of the single superparamagnetic domains immediately jumps among stable orientations, owing to the fact the difference in energies is negligible. Those differences are so small that is enough to allow the cancelation of total particle magnetization by the thermal energy (DEMAS; LOWERY, 2011).

The balance of magnetostatic, anisotropy, and exchange energies determines the size of the critical domain and, considering that half of the single-domain energy can be correlated to the magnetostatic, multi-domains occur in particles with dimensions larger than D_s, as schematized in Figure 2.5. The H_c value is zero when the dimension of single-domain particles is smaller than the critical diameter related to superparamagnetism (D_{spm}). H_c decreases as particles

diameter diverges from D_s. Only at a single-domain regime, the maximum coercivity can be reached. Because of thermal energy, which leads to random effects, the coercivity decreases in smaller particles. Due to domain divisions, this value also decreases for materials presenting multi-domains (MOHAPATRA; LIU, 2018).

Figure 2.5 – Single or multidomain formation and nanosize effect on the magnetic properties of particles.

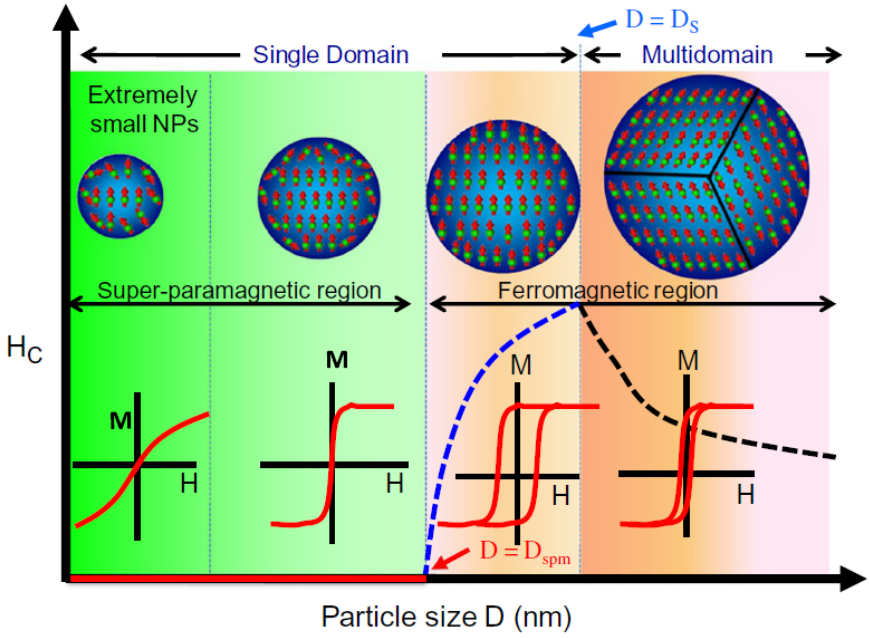

Reference: (MOHAPATRA; LIU, 2018)

The magnetization curves of superparamagnetic nanoparticles are commonly collected for studying the magnetic dipole moment. However, the particles must be diluted enough to individually respond to the applied field. Otherwise, if the samples are immobilized, the easy axes are fixed, affecting the magnetic anisotropy of the particles and, consequently, the orientation. Langevin's equation (Equation 2.1) describes the field-dependent magnetization, owing to the orientational freedom of magnetic crystals in liquid (CHANTRELL *et al.*, 1978; VAN RIJSSEL *et al.*, 2015). Figure 2.6 represents how a magnetization curve is constructed (SILVA, 2017).

$$M(\alpha) = \coth(\alpha) - \frac{1}{\alpha};\ \alpha = \frac{\mu_0 m H}{k_B T};\ \mu_0 = 4\pi \times 10^{-7}\ TA^{-1}m \qquad \text{Equation 2.1}$$

Where m = dipole moment, H = external field (A/m) and $k_b T$ = thermal energy.

Figure 2.6 – Magnetization curve illustration of a material magnetized to saturation under an applied magnetic field.

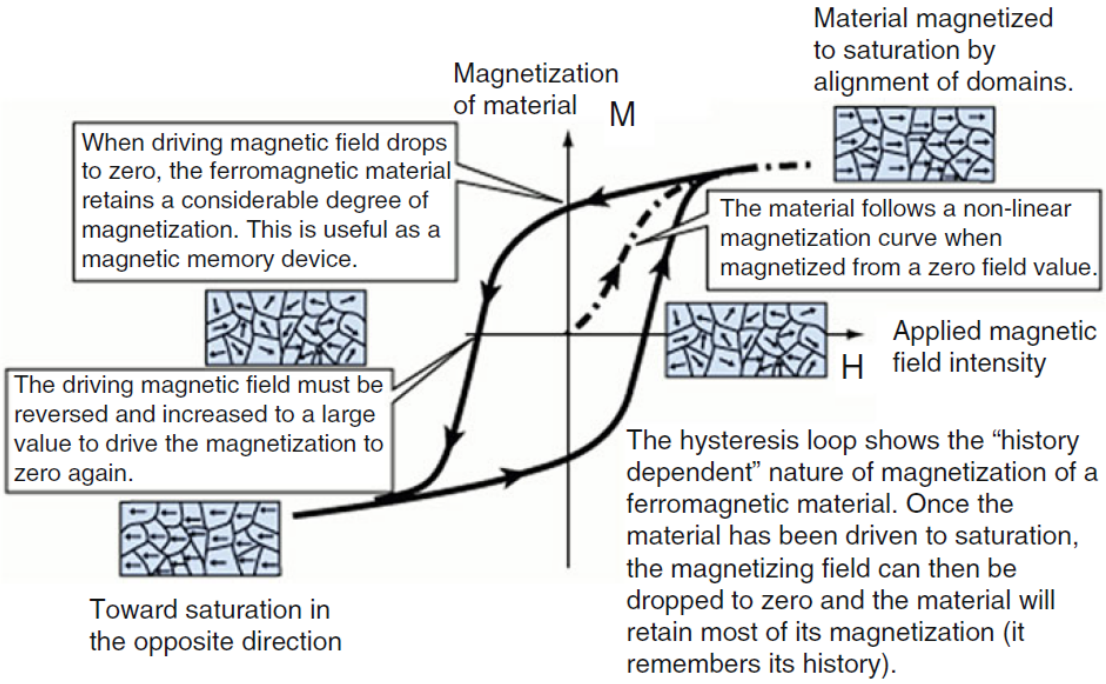

Reference: (SILVA, 2017).

Another useful property achieved due to magnetization curves is the magnetic diameter of nanoparticles. Usually, a crystallized magnetic core is surrounded by an amorphous and non-stable layer composed of multiple iron oxides other than magnetite (VAN RIJSSEL *et al.*, 2015). This magnetically dead layer leads to a decrease in saturation magnetization and can be estimated by the Langevin function fitted to magnetization curves. The chemical route used to synthesize the nanoparticles determines the magnetic properties, crystalline structure, and, therefore, also the magnetic diameter (UNNI *et al.*, 2017a).

2.1.3 Dynamic Magnetic Susceptibility

Particles with single-domain are governed by energy barriers, as illustrated in Figure 2.7 (a). These energies guide the magnetic behavior of such particles, considering total energy (E), magnetic anisotropy (K), the volume of the nanoparticle (V), the angle between the easy axis and particle magnetization (θ),

saturation magnetization (M_s) and the applied field (H) (ABENOJAR *et al.*, 2016). Another property of magnetic nanoparticles is the relaxation time, determined by the size distribution of the sample, temperature, layer coating thickness, and particles core because these characteristics affect magnetic crystals. The particles can be subjected to two different mechanisms of relaxation or a combination of them. In some situations, the magnetic dipole rotates within the particles, whose physical structure is fixed and this is called Néel relaxation (Figure 2.7 (b)). On the other hand, Brownian relaxation is defined as the physical rotation of the entire particle under a time-varying applied field and the magnetic dipoles are oriented to a fixed direction, as suggested in Figure 2.7 (b) (ABENOJAR *et al.*, 2016; MALDONADO-CAMARGO *et al.*, 2016).

Figure 2.7 – (a) Illustration of the energy barriers in single-domain particles and (b) representation of Néel and Brownian relaxation.

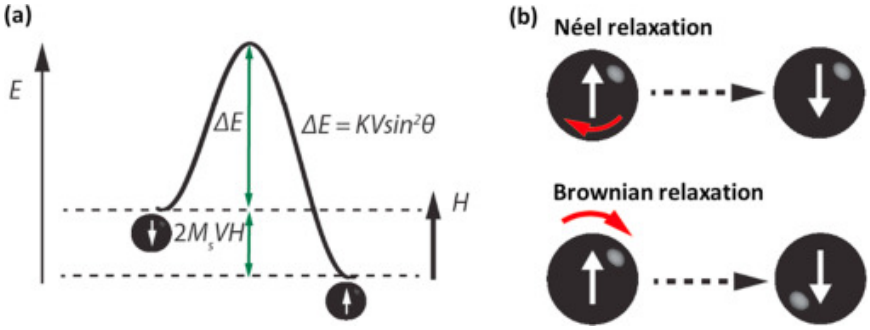

Reference: (ABENOJAR *et al.*, 2016).

Equation 2.2 and Equation 2.3 give, respectively, the Brownian and Néel relaxation times (ROSENSWEIG, 1985; MALDONADO-CAMARGO *et al.*, 2016).

$$\tau_B = \frac{3V_h\eta_0}{k_BT} \qquad \text{Equation 2.2}$$

$$\tau_N = \frac{1}{f_0}\exp\frac{K_aV_c}{k_BT} \qquad \text{Equation 2.3}$$

Where τ_B = Brownian relaxation time, V_h = particles hydrodynamic volume η_0 = viscosity of the liquid carrier, k_B = Boltzmann constant, T = absolute temperature, τ_N = Néel relaxation time, f_0 = frequency, ≈ 10^{-9} Hz, K_a = anisotropy constant, V_c = magnetic core volume.

The mechanism of relaxation governing ferrofluids under an alternating magnetic field can be measured by Dynamic Magnetic Susceptibility (DMS). In DMS spectra, one peak is observed for samples rotating only by Brownian or Néel relaxation. Ideally, the in-phase and out-of-phase curves cross each other when the particles are completely Brownian, according to the Debye model. For samples consisting of a mixture of particles relaxing by both mechanisms, two peaks are observed, but the in-phase and out-of-phase components do not present crossing, as demonstrated in Figure 2.8 (MALDONADO-CAMARGO *et al.*, 2016).

Figure 2.8 – DMS spectra representation for particles governed by Néel relaxation (red dashed line), Brownian (blue solid line), or a mixture of particles relaxing by both (black dashed line).

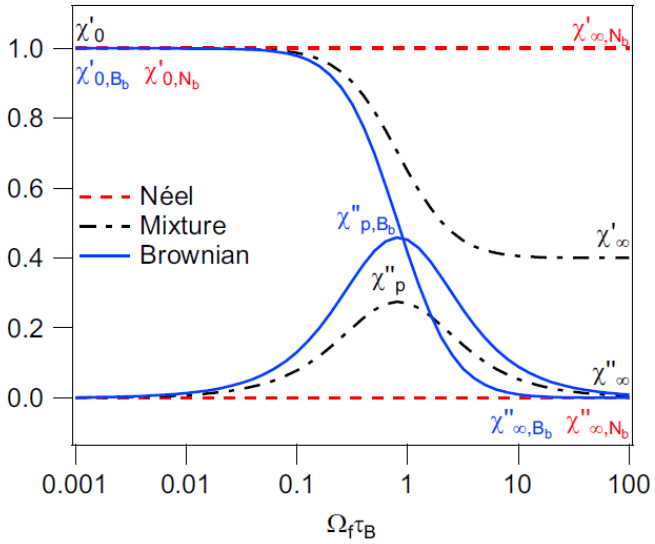

Reference: (MALDONADO-CAMARGO *et al.*, 2016).

Where χ'_0 = zero frequency in-phase susceptibility, χ'_∞ = infinite frequency in-phase susceptibility, χ''_p = peak in the out-of-phase susceptibility.

The heat dissipation ability of magnetic nanoparticles, essential for hyperthermia applications, is generated due to magnetic moments relaxation delay by Brownian and Néel mechanisms (ANDRADE, ÂNGELA L *et al.*, 2012). Analogously, how the nanoparticles rotates also matters for other purposes. The image quality in terms of resolution and sensitivity is expected to worsen in MPI when analyzing particles significantly governed by Brownian rotation. In this

context, aiming to estimate the fraction of Néel and Brownian particles, Maldonado-Camargo *et al.* (2016) derived some equations and applied them to DMS spectra of samples consisting only of particles governed by Brownian or Néel rotation and mixtures relaxing by both. The equations that these authors used will be described on Page 86 (MALDONADO-CAMARGO *et al.*, 2016).

2.1.4 Magnetic Particle Imaging

Magnetic Particle Imaging (MPI) is a new image modality able to track and quantify SPIONs. First reported by Gleich and Weizenecker in 2005 (GLEICH; WEIZENECKER, 2005), MPI uses includes, but are not limited to cancer imaging (YU *et al.*, 2017), *in vivo* evaluation of biodistribution, and clearance of stem cells (ZHENG *et al.*, 2016), investigation of aneurism hemodynamics (SEDLACIK *et al.*, 2016) and controlling bleeding in the traumatic brain (ORENDORFF *et al.*, 2017). The images construction does not require ionizing radiation or contrast agent and is created with negligible tissue background and slight signal attenuation (ZHOU *et al.*, 2018).

MPI general concepts rely on the non-linear superparamagnetic response of materials along with their saturation in magnetization at some magnetic field strengths, as represented by Figure 2.9. Materials with magnetic properties present magnetization *M(t)* in the function of time (*t*), under an oscillating magnetic field (*H,* also called modulation field, represented as green curve in Figure 2.9) with enough amplitude *A* and single drive frequency f_1. A series of harmonic frequencies and also f_1 consists of *M(t)*. Higher harmonics (demonstrated as *S*, red bars in the Fourier Transform) are observed for time-dependent magnetization (represented as red curve) because of the non-linear magnetization curve (black curve) of the material. When occurs addition of a time-independent field to the modulation field, because of constant saturation, the magnetization of the material is not affected by *H,* and the harmonics are suppressed. The image reconstruction occurs starting from the harmonics highlighted by grey boxes in Figure 2.9 (a) and (b). Because of the difficulty in isolating the f_1 signal owing to the fact the superimposed modulation field signal is higher, f_1 is not applied for developing the image. By adequately filtering, the

received signal can be differentiated from higher frequencies (GLEICH; WEIZENECKER, 2005).

Figure 2.9 – (a) Modulation field applied to the material at a single frequency; (b) addition of time-independent field to the modulation field (b).

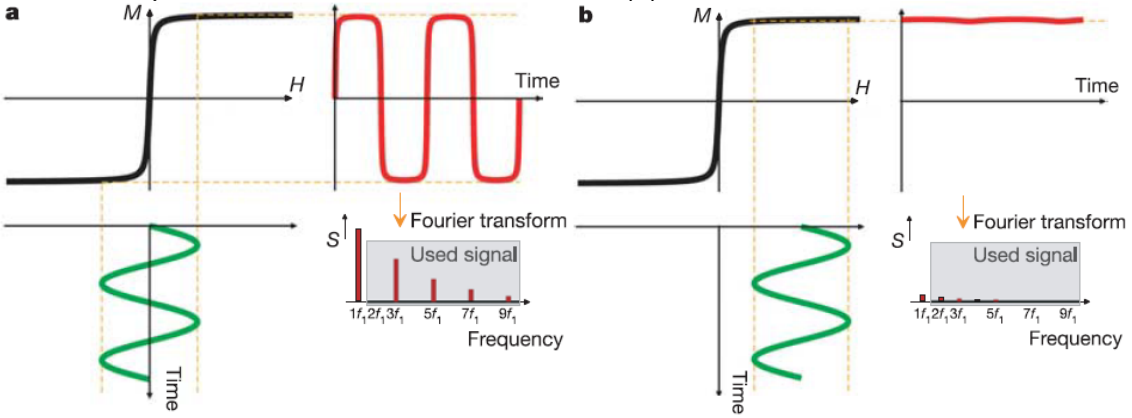

Reference: (GLEICH; WEIZENECKER, 2005).

A field-free point (FFP) or selection field appears because the time-independent field added to the modulation field is superimposed, increasing towards the edges of the imaging device, but vanishes in the center. In summary, the produced signal arises from the material located at the FFP, considering that those materials respond to the oscillating field. Therefore, magnetic nanoparticles out of the selection field retain the saturation in magnetization and do not generate a signal. For those reasons, tomographic information can be obtained by moving the selection field through the interest area and volume (GLEICH; WEIZENECKER, 2005). Figure 2.10 illustrates the creation of the FFP (HERZ *et al.*, 2018).

Figure 2.10 – How FFP is created in MPI by opposing permanent magnets. The signal is generated only by nanoparticles located at the selection field, because of the non-linear response to the superimposed magnetic field.

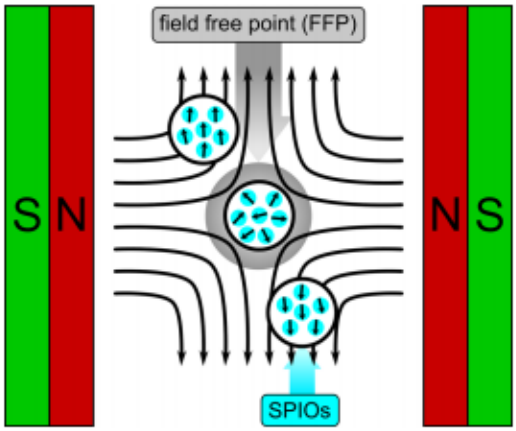

Reference: (HERZ *et al.*, 2018).

An outline of the main components of an MPI scanner, proposed by Gleich and Weizenecker in 2005 is demonstrated in Figure 2.11. The selection field arises from the selection and drive field coils and consequent two opposing direct currents. The harmonics are created by the recording coils. In Figure 2.11b, a scanner able to encode only by drive fields is exemplified. In this case, two opposing drive field coils generating an almost homogeneous field in the center are applied for each spatial direction (GLEICH; WEIZENECKER, 2005).

Figure 2.11 – The concept and main components of an MPI scanner: (a) selection and drive field coils, recording coils, and FFP creation and (b) selection field generator and drive field coils representation.

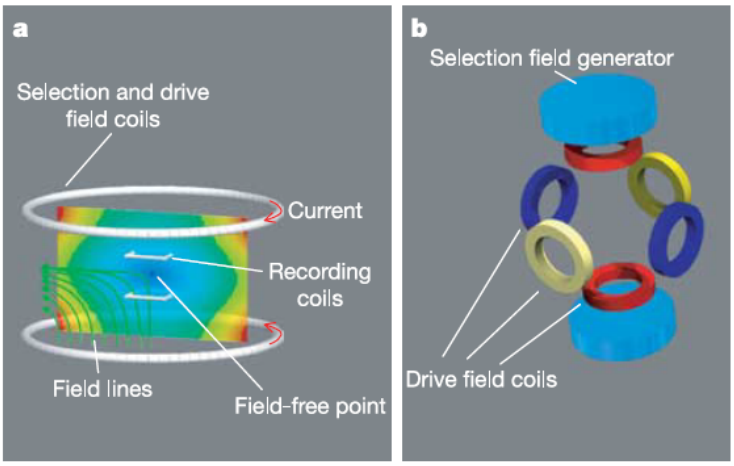

Reference: (GLEICH; WEIZENECKER, 2005).

The x-space formalism of MPI is schematically represented in Figure 2.12. The non-linear magnetization response of SPIONs, determined by the Langevin function, generates the MPI signal, that is, the Point Spread Function (PSF) (SARITAS *et al.*, 2013).

Figure 2.12 – x-space concepts of MPI: (a) Langevin function characterizes the magnetization curves of SPIONs, which results in non-linear response and determines the PSF, (b) creation of the FFP by permanent magnets, and (c) the movement of FFP for creating a trajectory cross the image.

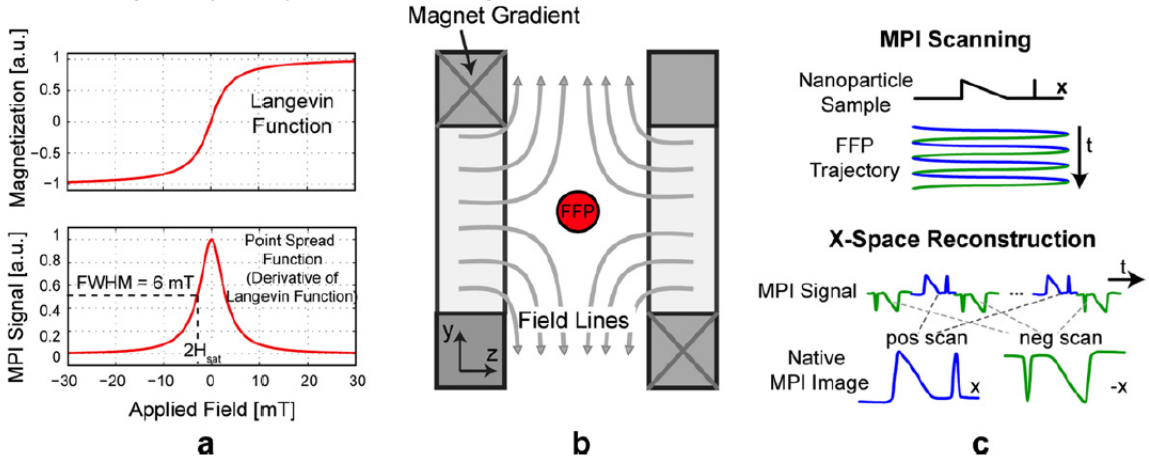

Reference: (SARITAS *et al.*, 2013).

The use of a Magnetic Particle Relaxometer (MPR) is a fast, cheap and easy way to estimate the performance of the particles in MPI with high sensitivity and variable excitation field, frequency, and amplitudes. For such purposes, small volumes of samples are required. Therefore, MPR is a valuable technique for investigating magnetic nanoparticles behavior in situations in which an MPI full system is not available (GARRAUD *et al.*, 2018).

2.2 MATERIALS AND METHODS

The experiments described in this Chapter were conducted in the University of Florida Department of Chemical Engineering and J. Crayton Pruitt Family Department of Biomedical Engineering.

The precursors of iron used for synthesizing the nanoparticles, iron (II) chloride tetrahydrate 99% ($FeCl_2 \cdot 4H_2O$), iron (III) chloride hexahydrate 97% ($FeCl_3 \cdot 6H_2O$), tetramethylammonium hydroxide (TMAOH) solution 25% w/v, iron standard for ICP, Ferucarbotran (Resovist, from Meito Sangyo Co. Ltd, 58.6 mg/mL), hydroxylamine hydrochloride 99% ($NH_2OH \cdot HCl$), chloroform ($CHCl_3$), sodium acetate >99% (CH_3COONa), DSPC (1,2-distearoyl-*sn*-glycero-3-phosphocholine), 1,10-phenanthroline monohydrate >99% were purchased from Sigma-Aldrich. Nitric acid (HNO_3, Optima^{TM} grade) and ammonium hydroxide (NH_4OH) 29% v/v were bought from Fisher Scientific and ammonium molybdate ($(NH_4)_6Mo_7O_{24}$) from Merck. Deionized water (18.2 Ω) was used throughout the processes.

2.2.1 Synthesis of iron oxide nanoparticles

IONPs were synthesized by coprecipitation in alkaline media, under an inert atmosphere and peptized with TMAOH (MÉRIDA *et al.*, 2015). The processes were performed in a fume hood. To this end, 200 mL of a solution containing a total iron concentration of 0.3 $mol.L^{-1}$ was prepared, maintaining the molar ratio of $1Fe^{2+}$:$2Fe^{3+}$, starting from separated solutions of both precursors, previously sonicated in a water bath for 20 minutes and deoxygenated for 5 min. The mixture was made in a wide neck reactor placed inside a heating mantle (TM570, Glas-Col), mechanically stirred at 250 rpm (overhead stirrer BDC2002, Caframo) under vigorous bubbling of nitrogen, and heated until 75°C, when 35 mL of NH_4OH was added. Then, the temperature was set to 85°C, and the pH controlled for 1 hour at the range 8 - 9. Once the reaction was completed, the magnetic solution was cooled down to room temperature, still under stirring and inert atmosphere.

Aliquots of 20 mL of magnetic particles were transferred to 50 mL conical tubes and centrifuged at 1,500 rpm for 10 minutes (5430R, Eppendorf), followed by discard of the supernatant supported by a magnet at the bottom of the tubes to hold the pellet. This step was made for removing reaction sub-products.

For peptization, TMAOH (25% w/w 1 mol.L^{-1}) was added to the particles pellet in proportion 1:1, owing to the centrifuged volume of magnetic solution. After homogenizing in a vortex until the particles are completely solubilized, the content of all conical tubes was poured in a glass jar and ultrasonicated in an ice bath, using a high energy probe at the amplitude of 40% with a pulse-pause combination of 10 seconds off, 40 seconds on. Then, the solution was centrifuged at 1,800 rpm for 10 minutes, the supernatant was discarded and the peptization was repeated. Finally, the peptized nanoparticles were centrifuged at 2,500 rpm for 10 minutes, the supernatant discarded and the black paste poured in a glass jar, which was allowed to dry overnight at room temperature in a fume hood, followed by storage at 4°C.

2.2.2 Iron quantification by UV absorption assay

Initially, 2 µL of iron oxide nanoparticles were completely digested in 1 mL of nitric acid 70% overnight, in borosilicate tubes at 101°C, by using a dry bath. Tubes containing deionized water were added as blank and all samples were prepared in triplicate. On the next day, 10 µL of the digested samples were dried in borosilicate vials for 1 hour at 115°C in the dry bath. Meanwhile, iron standards for ICP previously diluted in deionized water and storage at 4°C, at concentrations from 0 – 100 µg/mL were prepared, as described next for the samples. Once the drying of the samples had finished, 46 µL of deionized water were added to each vial, followed by the addition of 30 µL of hydroxylamine (8.06 mol.L^{-1}), and this reaction was allowed for 1 hour, to reduce Fe^{3+} to Fe^{2+} and also prevents ferrous ions oxidation. Then, 49 µL of sodium acetate (1.22 mol.L^{-1}) was used as a buffer, and 75 µL of 1,10- phenanthroline (13 mmol.L^{-1}) was added to form the complex iron (II)– *o*- phenanthroline. Finally, 100 µL of each sample and iron standard were pipetted out to microplates and the UV absorption of the iron (II)– *o*- phenanthroline complex was read at a wavelength of 508 nm in a Spectramax M5, Molecular Devices.

Based on the absorptions of iron standards, the calibration curve was made by linear regression, considering R^2=0.9999. According to Beer's Law (Equation 2.4), the concentration is proportional to sample absorbance.

$$\boldsymbol{A = \varepsilon bc} \qquad \text{Equation 2.4}$$

Where A = absorbance (arbitrary units), ε = molar absorptivity (mL/mg.cm), b = the path length (~ 1 cm), c = concentration (mg/mL).

The total iron mass was calculated based on the slope from the absorbance *vs* concentration graph and also considering the dilution factor of each sample, from the digestion process until the addition of reagents. Further, it is important to analyze the error of each measurement, which should not be higher than 10%, along with standard deviations.

2.2.3 Preparation of magnetoliposomes

DSPC liposomes entrapping IONPs peptized with TMAOH were prepared by the thin-film hydration method. The 2D structure of the phospholipid is represented in Figure 2.13.

Figure 2.13 – 2D structure of the phospholipid DSPC, used for forming the liposomes by hydration method.

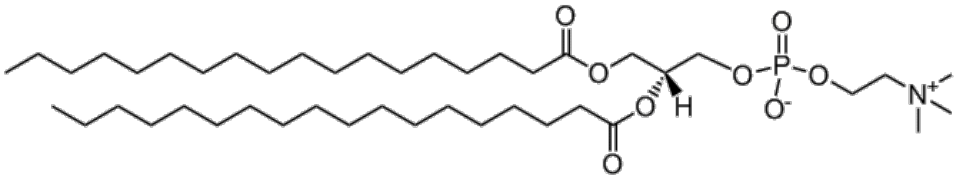

Reference: Avanti Polar Lipids.

The phase transition temperature of DSPC is 55°C, therefore the magnetoliposomes preparation was carried out under 65°C. A 50 mL borosilicate round-bottom flask was used (the volume matters because larger flasks change the thin film formation). First of all, 4 mL of a solution containing 1 mg/mL of DSPC in chloroform was prepared at room temperature, followed by rotary evaporation of the organic solvent in a Buchi R- 215 rotary evaporators for 1.5 hours at

220 rpm, 65 °C, and 1008 mbar. Meanwhile, the IONPs solution previously prepared at 2 mg/mL of Fe_3O_4, pre-filtered once through PTFE 0.22 µm membranes and quantified by UV absorption assay was sonicated in the water bath for 20 minutes and heated until 65 °C for 1 hour. It is important to certify that the temperature of nanoparticles is higher than the phase transition of the phospholipid. Otherwise, the self-assembly mechanism of magnetoliposomes will be affected and the encapsulation may not occur. Once the 1.5 hours required for chloroform evaporation had been completed, 4 mL of the pre-heated IONPs were added to the thin film of a phospholipid, and the hydration was allowed for 1 hour at 220 rpm in the rotary evaporator, without applying vacuum.

To reduce vesicles lamellarity, five cycles of freeze and thaw were performed by alternating between exposing the round-bottom flask to liquid nitrogen and water bath at 65 °C with circular movements. Immediately after completing freeze and thaw cycles, the magnetoliposomes solution was quantitatively transferred to a conical tube and ultrasonicated for 5 minutes at amplitude 38%, cooled down in hands, and ultrasonicated again, totalizing energy of 4.3 kJ. As an annealing step, the sample was kept in the water bath at 65 °C for 1 hour, cooled down to room temperature for 30 minutes, and stored at 4 °C. The liposomes should not be exposed to fast temperature variation for avoiding content release.

2.2.4 Characterization

Magnetoliposomes should not be characterized on the same day of preparation, because the results were found to be very different. However, the characterizations should be completed within one week because particles' passive release over time was observed in the initial samples (data not shown), once no phospholipid other than DSPC was used, neither PEGylation, which should improve vesicles permeability and stability.

2.2.4.1 Transmission Electron Microscopy (TEM)

IONPs were imaged in a Hitachi H-7000 Transmission Electron Microscope with Veleta CCD side-mount camera, whereas the encapsulation in liposomes was investigated in a Hitachi H-7600 Transmission Electron Microscope at an acceleration voltage of 80 kV. The ideal concentration of IONPs was found to be 45 µg/mL onto 200-mesh formvar coated copper grids, and 0.09 mg/mL of iron oxide for magnetoliposomes. Because the lipid bilayers are electron transparent, magnetoliposomes were stained with 2% (w/v) of ammonium molybdate at pH 7.4 and room temperature, at the volumetric proportion of 1:1. The samples were allowed to be stained for 5 minutes before pipetting 10 µL on TEM grids.

It is crucial to certify that the staining solution is free of crystals. Additionally, the magnetoliposomes grid must be imaged from 4 hours to one week after preparation because it was visually observed sample degradation over time, confirmed by the greenish color that appears on the older grids containing magnetoliposomes. Further, magnetoliposomes should not be imaged right after grid preparation because drying artifacts may be added to the micrographs. The grids used for magnetoliposomes should not be imaged more than twice because electron beam can lead to membrane disruption and particle release. Ideally, Cryo-TEM is the best choice for imaging liposomes.

The statistical analyses were made in ImageJ 1.52a aiming to access the physical size of the samples, counting at least 1,000 particles or magnetoliposomes across images. The lognormal distribution fit was made in IGOR Pro 6.37, which allowed to obtain number median diameter (D_{pg}), geometric deviation (ln σ), and volume median diameter (D_{pgv}), as described by Equation 2.5 (UNNI *et al.*, 2017a).

$$D_{pgv} = \exp\left(lnD_{pg} + 3ln^2\sigma\right) \qquad \text{Equation 2.5}$$

Next, the arithmetic volume mean diameter (D_{pv}) and standard deviation (σ) were calculated by applying Equation 2.6 and Equation 2.7 (UNNI *et al.*, 2017a).

$$D_{pv} = \exp\left(lnD_{pgv} + \frac{ln^2\sigma/2}{2}\right)$$ Equation 2.6

$$\sigma = D_{pv}\sqrt{\exp(ln^2\sigma) - 1}$$ Equation 2.7

2.2.4.2 Dynamic Light Scattering

DLS was applied to measure the hydrodynamic diameters and electrophoretic mobility of IONPs and magnetoliposomes in a BI-90Pluse/Zeta PALS dynamic light scattering and zeta potential analyzer. The samples were diluted to 0.02 mg/mL of Fe_3O_4 in deionized water and 10 runs of 30 seconds were completed at 25 °C, scattering angle of 90°, considering refractive index 1.450 and uniform spheres.

The samples were prepared at the same concentration for charge determination (10 runs, 25 °C), but diluted in KCl 1 mmol.L^{-1} and the pH was previously collected. Smoluchowski model was used.

2.2.4.3 Superconducting Quantum Interference Device (SQUID) magnetometry

A Magnetic Property Measurement System 3 (MPMS 3, Quantum Design) was used for collecting magnetization curves at 300 K of 100 µL of sample and magnetic fields range of -7 to 7 T. The magnetic diameter values were estimated through magnetogranulometry, applying the Langevin function and lognormal fit in IGOR Pro 6.37.

2.2.4.4 Dynamic Magnetic Susceptibility

To evaluate the fraction of particles governed by Néel and Brownian rotation before and after the encapsulation, IONPs and magnetoliposomes were analyzed by DMS. The spectra were acquired by a DynoMag Susceptometer (Acreo) in volume susceptibility mode using 200 µL of the sample at 2.45 mg/mL of Fe_3O_4. IGOR Pro 6.37 was used for fitting the data to the Debye model by the lognormal distribution of hydrodynamic diameter.

The hydrodynamic diameter, zero frequency, and infinite frequency in-phase susceptibility were calculated and the fractions were obtained, as shown in Equation 2.8 and Equation 2.9 (MALDONADO-CAMARGO *et al.*, 2016).

$$\phi_N = \frac{\chi'_\infty}{\chi'_0} \qquad \text{Equation 2.8}$$

$$\phi_B = \frac{\chi'_0 - \chi'_\infty}{\chi'_0} \qquad \text{Equation 2.9}$$

Where ϕ_N = Néel fraction, ϕ_B = Brownian fraction, χ'_0 = zero frequency in- phase susceptibility, χ'_∞ = infinite frequency in-phase susceptibility.

2.2.4.5 Magnetic Particle Imaging

To evaluate the applicability of IONPs before and after encapsulation in liposomes as tracer agents, MPI measurements were carried out in a Momentum imager (Magnetic Insight, Inc.). For comparison, the benchmark formulation Ferucarbotran was also analyzed. In the prototype Relax module, the Point Spread Function (PSF) was collected at an excitation field of 4 mT and frequency 45 kHz using 10 µL of the sample placed in PCR tubes. The concentrations of IONPs and magnetoliposomes were, respectively, 1.65 mg/mL and 58.6 mg/mL. The average of positive and negative scans raw data allowed calculating the peak signal-to-noise ratio (PSNR), which was normalized by iron mass. Additional data in the isotropic mode were collected for obtaining images of each sample. The Figure 2.14 presents a flowchart of the methodology.

Figure 2.14 – Flowchart of the processes from IONPs synthesis to MPI measurements

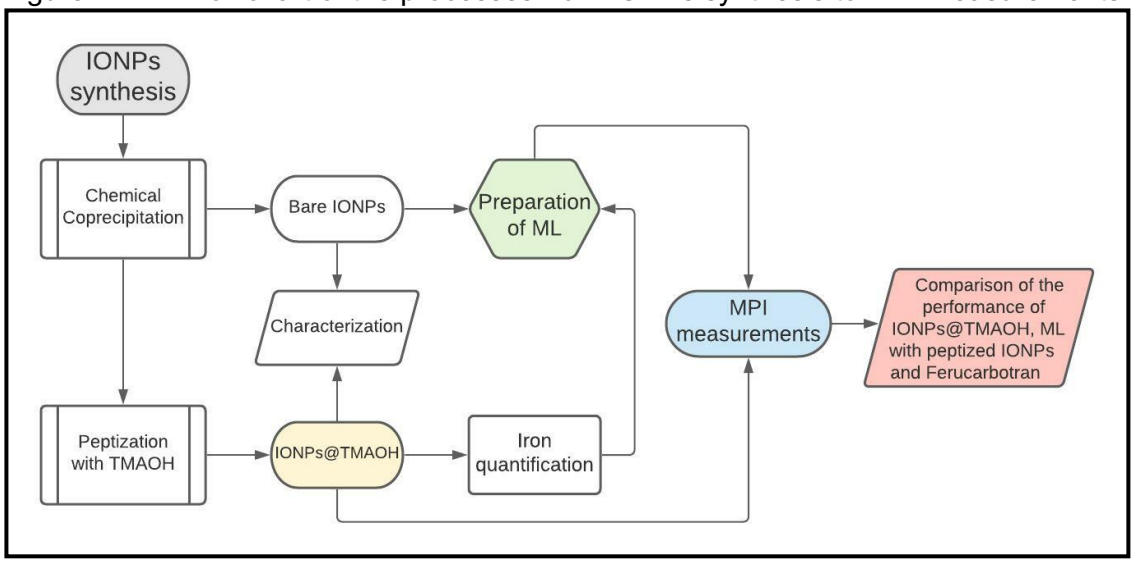

Reference: Author.

2.3 RESULTS AND DISCUSSION

2.3.1 Effects of peptization and nanoparticles concentration on entrapment in liposomes

In the early steps of magnetoliposomes preparation, peptized (IONPs @TMAOH) and non-peptized IONPs were tested to evaluate the effects over encapsulation, size, and magnetic properties. Figure 2.15 depicts TEM micrographs of those as-synthesized nanoparticles.

Figure 2.15 – TEM micrographs: (a) IONPs@TMAOH with magnification 100000 x, (b) 150000 x and (c, d) non-peptized IONPs with 100000 x.

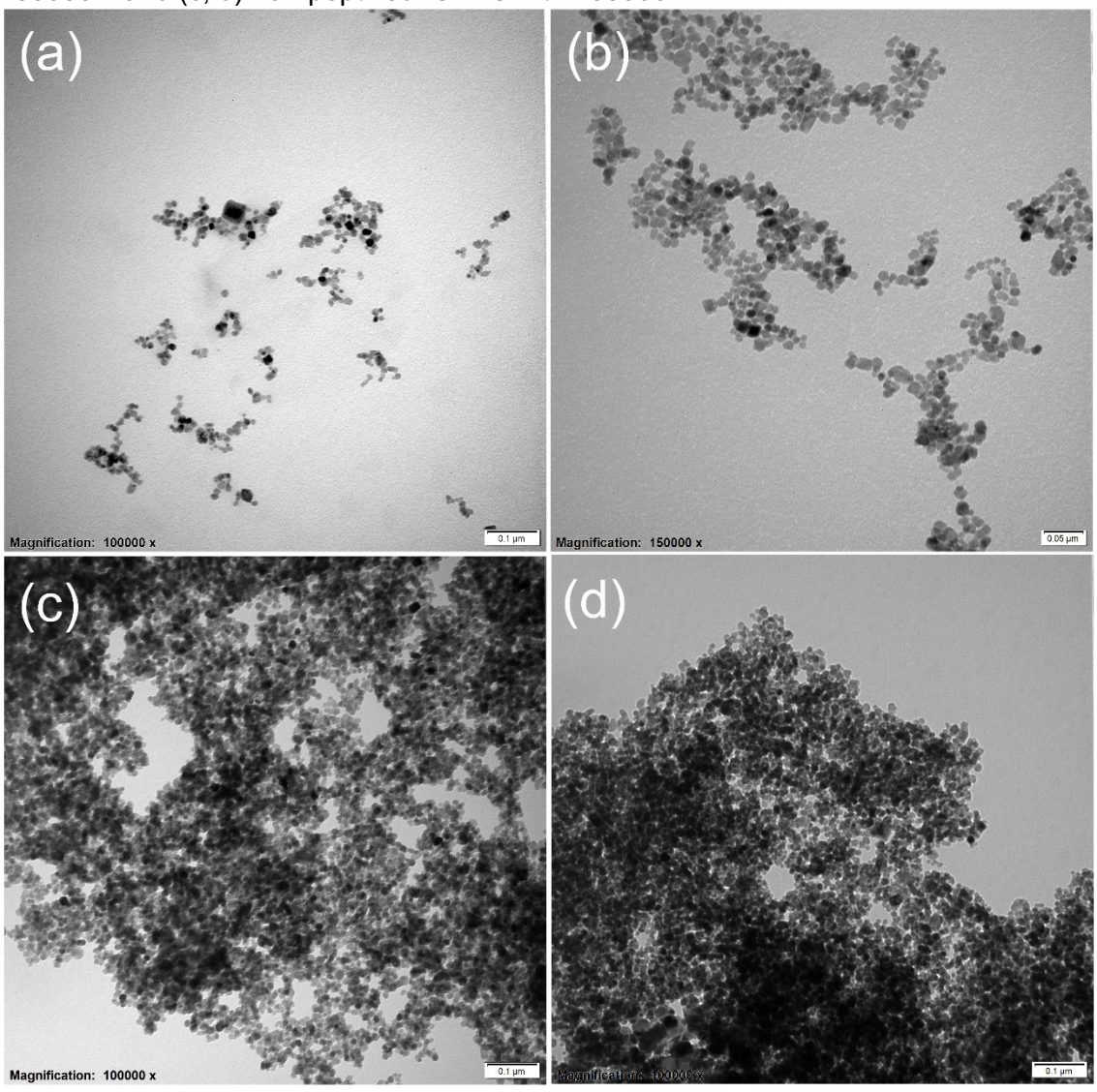

Reference: Author.

It is evident that IONPs@TMAOH are dispersed and non-peptized IONPs show agglomeration because no molecule was attached to the surface and consequently, repulsion did not take place. Zeta potential measurements confirmed these assumptions. The charge of IONPs@TMAOH was found to be - 26.31 mV at pH 7.23, whereas SPIONs was +0.442 mV at pH 5.81. Statistical analyses performed on TEM images of IONPs@TMAOH indicated a physical size of 10.4 ± 4.8 nm (the size distribution will be presented later when compared to magnetoliposomes data). The size distribution was not calculated for bare IONPs due to high polydispersity and sedimentation over time. The UV absorption assay used for iron quantification does not apply to sedimentable samples because mass gradient leads to higher errors than the acceptable by this method. Consequently, the mass balances did not close for bare nanoparticles. MPR measurements were carried out for both samples and the results are shown in Figure 2.16.

Figure 2.16 – MPR signal collected from (a) IONPs@TMAOH and (b) bare IONPs.

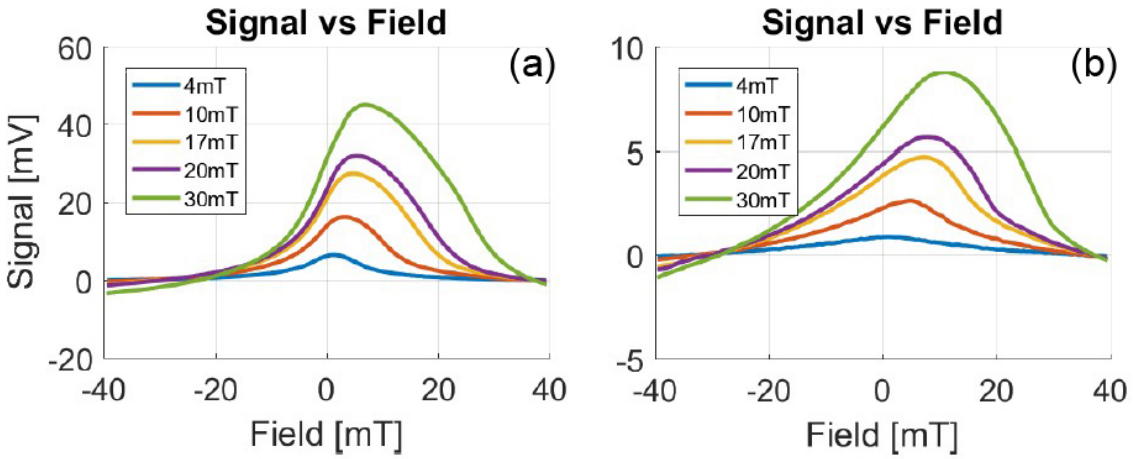

Reference: Author.

The highest signals, proportional to the excitation field, were observed for IONPs@TMAOH. As optimization step of magnetoliposomes (ML) preparation, particles concentration was investigated at 0.3, 1.0, 1.6, 2.5 and 3.0 mg/mL for both peptized (P) and non-peptized (NP). Zeta Potential measurements indicated, for ML with peptized nanoparticles at 0.3, 1.0, 1.6, 2.5 and 3.0 mg/mL, -15.65 mV (pH 8.11), -38.32 mv (pH 7.87), -22.55 mV (pH 8.15), -22.32 mV (pH 8.20) and - 29.19 mV (pH 8.38), respectively. The values for ML-NP were

found to be, at the same order of concentration, -0.226 mV (pH 7.21), +0.224 mV (pH 6.28), +13.20 mV (pH 5.90) (ML-NP-2.5 and ML-NP-3.0 were not measured). The charges indicated that the encapsulation did not affect the colloidal stability of peptized particles, neither for non-peptized. Further, the colloidal stability of these samples was visually observed over time, as shown in Figure 2.17. The lowest concentrations of IONPs@TMAOH did not favor the production of stable magnetoliposomes, because sedimentation occurred. However, at 1.6, 2.5, and 3.0 mg/mL of peptized nanoparticles, sedimentation was not noted (the picture was taken 51, 22 and 21 days after ML-P-1.6, ML-P-2.5, and ML-P-3.0 had been prepared). The zeta potential of ML-NP at all concentrations corroborated with the presence of sedimentation.

Figure 2.17 – Visual observation of the stability of magnetoliposomes formed with IONPs@TMAOH and non-peptized IONPs at different concentrations.

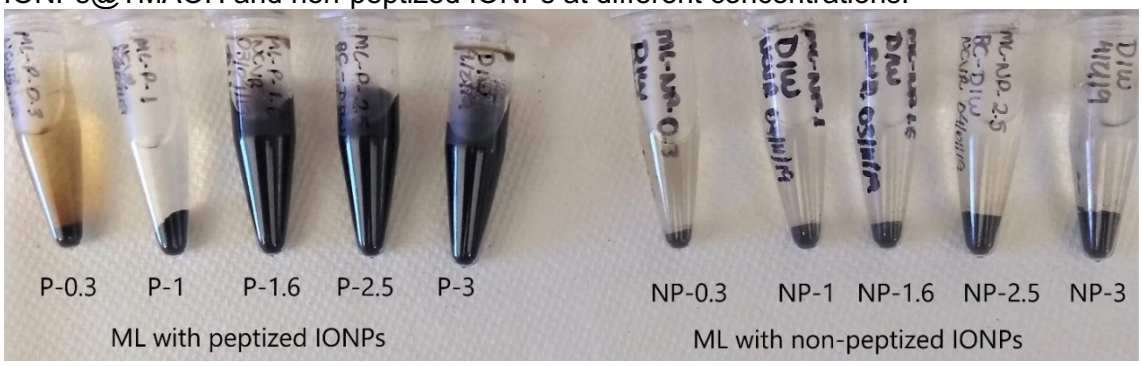

Reference: Author.

Figure 2.18 presents TEM micrographs of magnetoliposomes prepared with IONPs@TMAOH at 1.6 and 3.0 mg/mL and non-peptized IONPs at 1.0 and 1.6 mg/mL. The images of ML-P-2.5 presented a lot of unidentified artifacts and, therefore, are not shown.

Figure 2.18 – TEM micrographs of magnetoliposomes prepared with: IONPs@TMAOH at (a) 1.6 mg/mL and (b) 3.0 mg/mL and non-peptized IONPs at (c) 1.0 mg/mL and (d) 1.6 mg/mL.

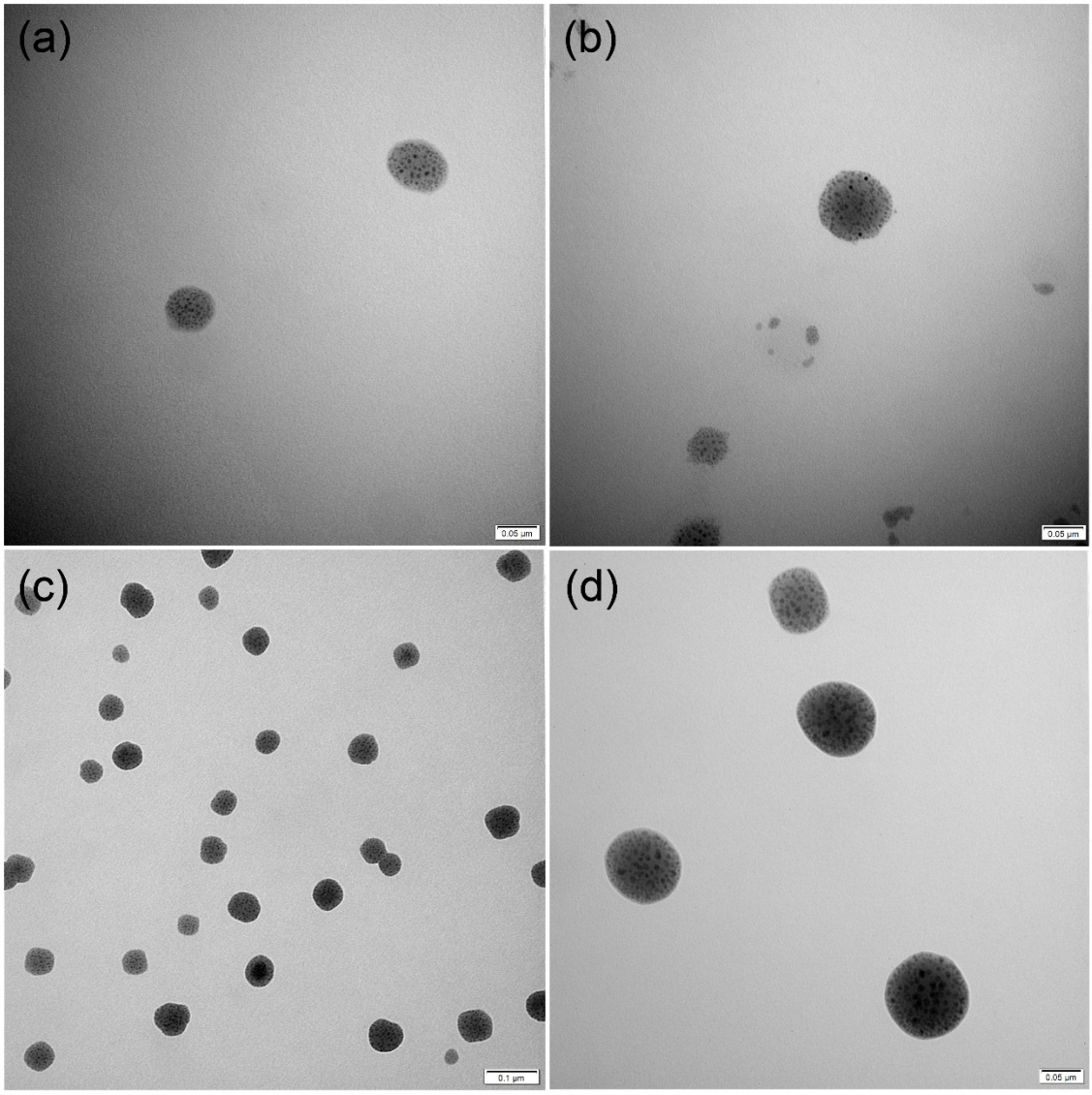

Reference: Author.

Statistical analyses for calculating the size distribution were not performed, considering the low number of magnetoliposomes per image. The micrographs proved the encapsulation of IONPs in DSPC liposomes. Even though the images of liposomes formed with non-peptized particles show a higher amount of material, those samples were not stable, as confirmed by Zeta Potential and visually. The observation of additional micrographs of magnetoliposomes prepared with IONPs@TMAOH suggested lots of free particles and empty vesicles at 2.5 and 3.0 mg/mL. The 1.6 mg/mL batch presented some encapsulated vesicles and also lots of empty liposomes. Therefore, the next

batches of magnetoliposomes, which had the best results in characterizations (presented in the next sections), were made starting from 2.0 mg/mL of IONPs@TMAOH.

2.3.2 Liposomes loaded with the proper concentration of peptized nanoparticles

2.3.2.1 The hydrodynamic and physical diameter

Figure 2.19 shows some micrographs of magnetoliposomes formed with 2.0 mg/mL of IONPs@TMAOH.

Figure 2.19 – TEM images of magnetoliposomes prepared with 2.0 mg/mL of IONPs@TMAOH.

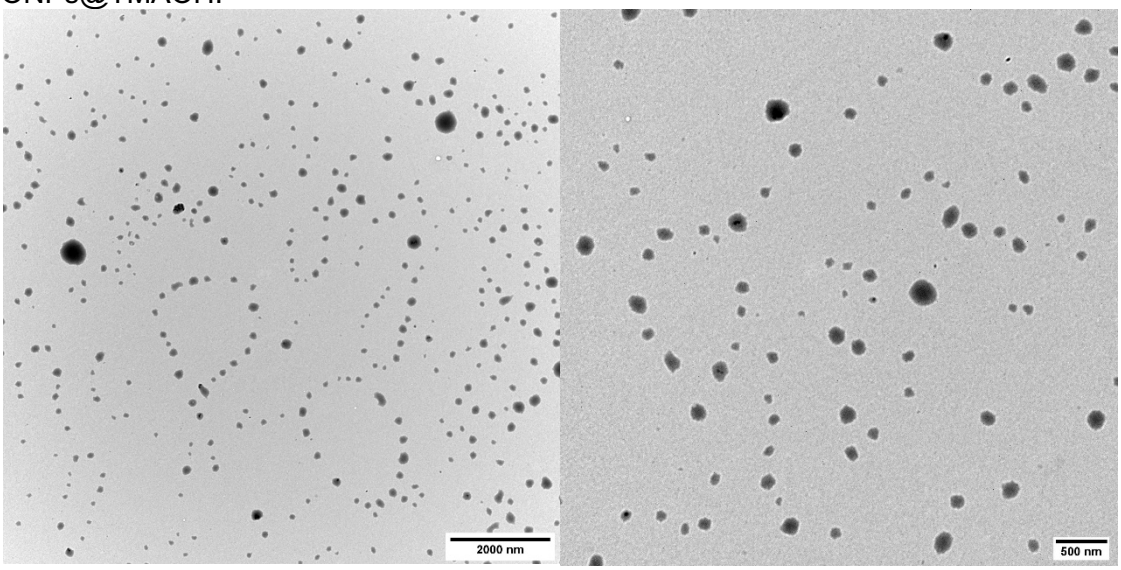

Reference: Author.

Figure 2.20 – TEM images along with size distributions and lognormal fit of (a, b) IONPs and (c, d) magnetoliposomes. The gray square in (c) represents the magnification area shown in (e).

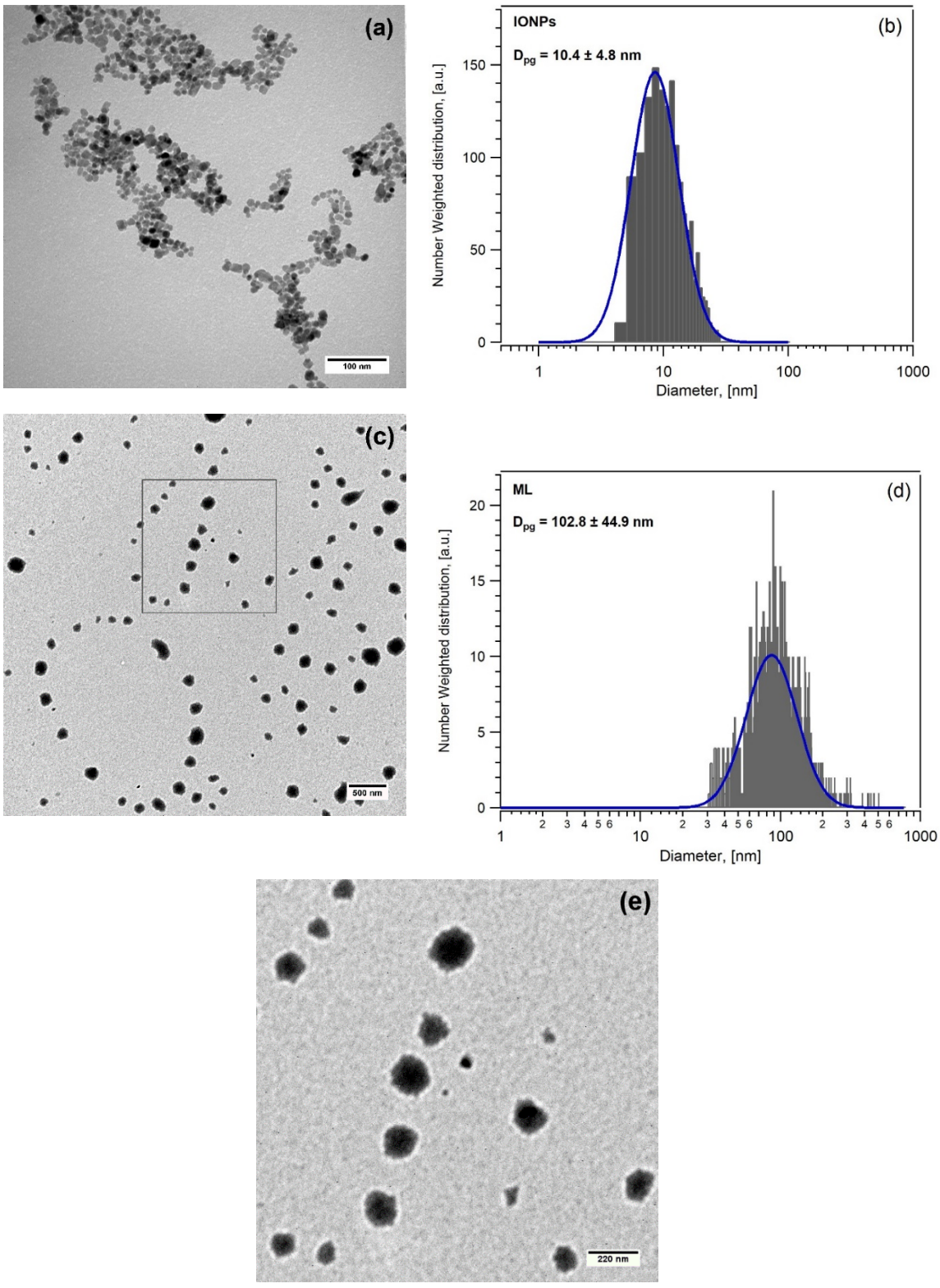

Reference: (ROST *et al.*, 2020).

It is noteworthy that the encapsulation of magnetic nanoparticles at 2.0 mg/mL occurred inside DSPC liposomes more effectively than to other concentrations of particles. Indeed, high-density packing of nanoparticles inside the vesicles was identified. Empty vesicles were not observed, some non-encapsulated particles were noted, which may be attributed to TEM grids preparation, stock, or even to the interaction with the electron beam that can disrupt liposomal structures. Anyway, the number of free nanoparticles was negligible if compared to magnetoliposomes. Statistical analyses were made because more than 1,000 liposomes were counted across images. The size distribution of magnetoliposomes is compared to the observed for as-synthesized IONPs@TMAOH in Figure 2.20.

According to the statistical processes on TEM images, the number median diameter of IONPs was found to be 10.4 ± 4.8 nm and of the roughly spherical magnetoliposomes, 102.8 ± 44.9 nm. The arithmetic volume mean diameter of IONPs and magnetoliposomes were, respectively, 20.5 nm (σ = 9.5 nm) and 189.5 nm (σ = 82.8 nm). Volume-weighted distributions were calculated for comparison with magnetic diameters values, which will be presented in Section 2.3.2.2. The hydrodynamic diameter distributions are demonstrated in Figure 2.21.

Figure 2.21 – The lognormal curve fit of the hydrodynamic diameter distributions of peptized IONPs (represented by black) and magnetoliposomes (gray). Data collected by DLS measurements.

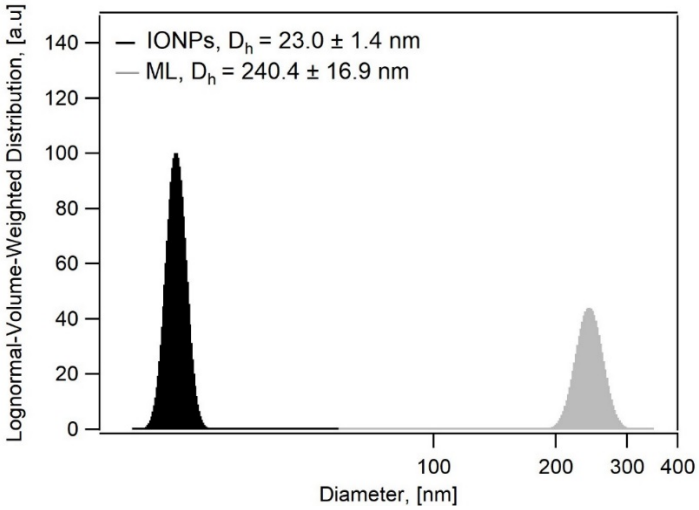

Reference: (ROST *et al.*, 2020).

The hydrodynamic sizes of peptized IONPs were found to be 23 nm (σ = 1.4 nm), which was very close to the physical size (20.5 nm). The hydrodynamic diameter of magnetoliposomes was 240.6 nm (σ = 16.9 nm), which is ~50 nm larger than the observed for the physical size. It is important to remind that DLS is sensitive to aggregates, which means that, even though non-encapsulated particles were detected in a lower amount than ML, they can contribute to the final results of DLS. TEM data, on the other hand, allows differentiating individual particles, and aggregates were not taken into account for the statistical analyses. Moreover, the analyses of liposomes by TEM are limited by vesicles shrinkage during the drying process, which leads to size reduction. In summary, usually liposomes characterization applies TEM and DLS for results complementation. The increase of particles size after liposomes formation, confirmed by both techniques, corroborates with encapsulation.

Zeta Potential values indicated IONPs surface charge -26.31 mV at pH 7.23 and -10.55 mV at pH 6.79 for magnetoliposomes. The lowest value of Zeta Potential was registered for magnetoliposomes prepared with higher concentration than 2.0 mg/mL, which can be explained by the presence of non-encapsulated IONPs@TMAOH.

2.3.2.2 Magnetic properties

Figure 2.22 shows the magnetization curves of both samples, IONPs and ML at 300 K, measured by SQUID. Based on these data, the superparamagnetic characteristic of both as-synthesized particles and magnetoliposomes was confirmed, because there was no hysteresis. Langevin fit was applied and the saturation magnetization, related to magnetite mass, was found to be 93 Am^2/kg and 78 Am^2/kg, respectively for IONPs and ML. Furthermore, the volume-weighted magnetic size distributions were obtained through magnetometry and the mean magnetic diameter calculated for IONPs was 15 nm (σ = 1.8 nm) and 16 nm (σ = 0.90 nm) for ML. The observation that the magnetic size of IONPs is comparable to the one obtained for ML suggests that nanoparticles did not aggregate inside the liposomes, although it is known that the entrapment affects inter-particle distances. The volume susceptibility mode DMS spectra are represented in Figure 2.23.

Figure 2.22 – (a) Magnetization curves of IONPs (solid spheres) and ML (hollow spheres); (b) magnetic size distributions.

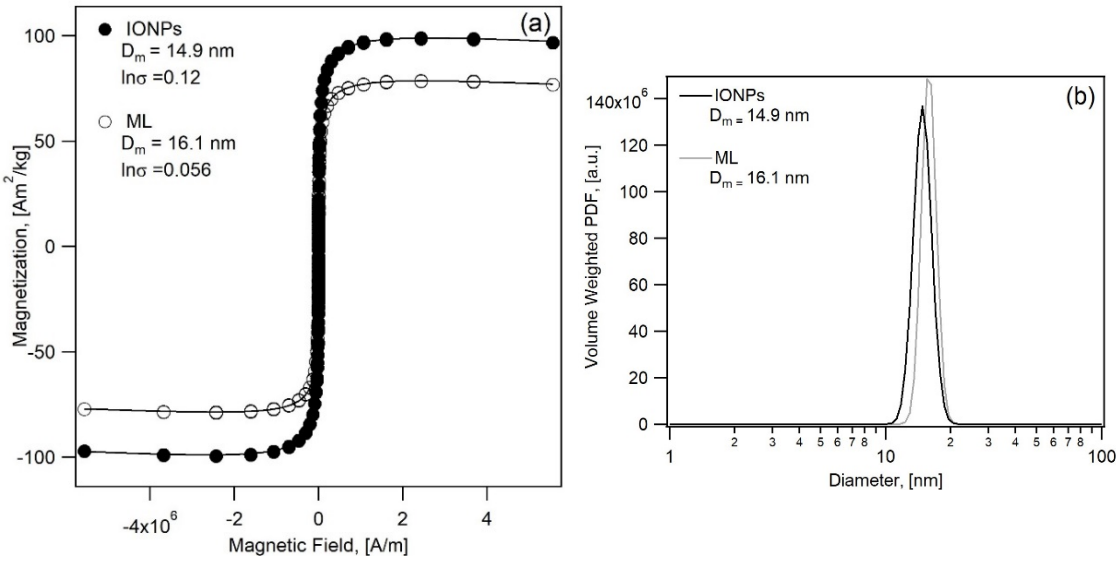

Reference: (ROST *et al.*, 2020).

Figure 2.23 – Volume susceptibility mode DMS spectra of IONPs (represented by circles) and ML (triangles).

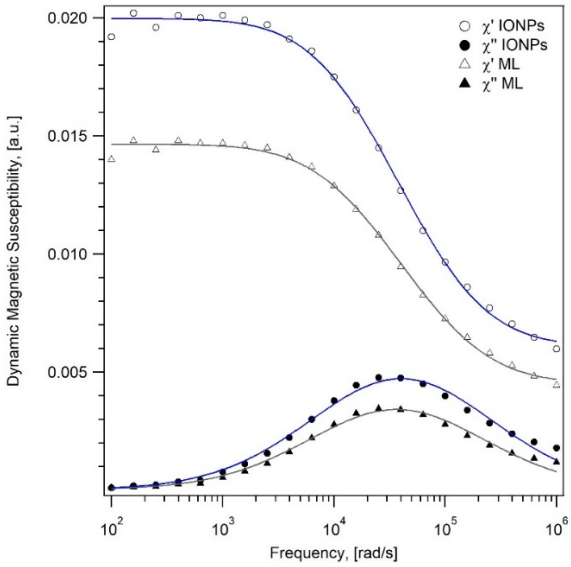

Reference: (ROST *et al.*, 2020).

Table 2.1 expresses a comparison among the sizes of IONPs and ML obtained from TEM, DLS, and DMS. Debye function applied on DMS spectra allowed to calculate the hydrodynamic diameter, zero frequency in-phase susceptibility (χ'_0), infinite frequency in-phase susceptibility (χ'_∞) and the fractions of particles governed by both Néel and Brownian relaxation mechanisms.

Table 2.1 – The hydrodynamic and physical diameter of IONPs and ML, achieved from DMS, TEM, and DLS data. The values of Néel and Brownian fractions along with infinite frequency in-phase susceptibility and zero frequency in-phase susceptibility are also shown.

Sample	D_p (nm) TEM	D_h (nm) DLS	D_h (nm) DMS	χ'_0	χ'_∞	ϕ_N	ϕ_B
IONPs	20.5	23.0	40.93	0.020	0.0061	0.31	0.69
ML	189.5	240.6	40.18	0.015	0.0045	0.31	0.69

Reference: (ROST *et al.*, 2020).

DMS data indicates that IONPs and ML were predominantly governed by Brownian rotation, but overall, both samples were a mixture of the two relaxation mechanisms. The rotation of the magnetic particles was not affected by encapsulation in liposomes, considering that Néel and Brownian fractions were not changed after the entrapment. Irrespective of the D_h of IONPs had been smaller than that of ML when measured by DLS, IONPs and ML had almost the same hydrodynamic diameter according to DMS (~40 nm). The multicore nature of IONPs and ML is inherent to the synthesis by coprecipitation because controlling the size distribution on those processes is complex. Therefore, magnetic nanoparticles produced by this method are usually polydisperse. Then, the formation of aggregates takes place and magnetic blocking can occur due to interactions among aggregates and also from Brownian relaxation. For those reasons, hydrodynamic diameters estimated from DMS results and the Debye model are commonly larger than the values obtained from DLS data. It is noteworthy that, in the case of magnetoliposomes, only the nanoparticles respond to the magnetic field, which means that it was expected to observe lower D_h when measured by DMS. However, the lipid bilayer is counted in the Brownian motion detected by DLS.

2.3.2.3 Performance of magnetoliposomes in MPI

Figure 2.24 demonstrates the PSF of IONPs and ML compared to Ferucarbotran. Those data were obtained at an excitation field of 4 mT and frequency of 45 kHz, by the Relax® module of the commercially available imager

Momentum from Magnetic Insights. The illustrated PSF of each sample was obtained as an average of two measurements of positive and negative scans.

Figure 2.24 – Point Spread Function of IONPs, ML, and Ferucarbotran, collected by a Momentum system (Magnetic Insights). The signals were normalized by iron mass, determined by UV absorption assays.

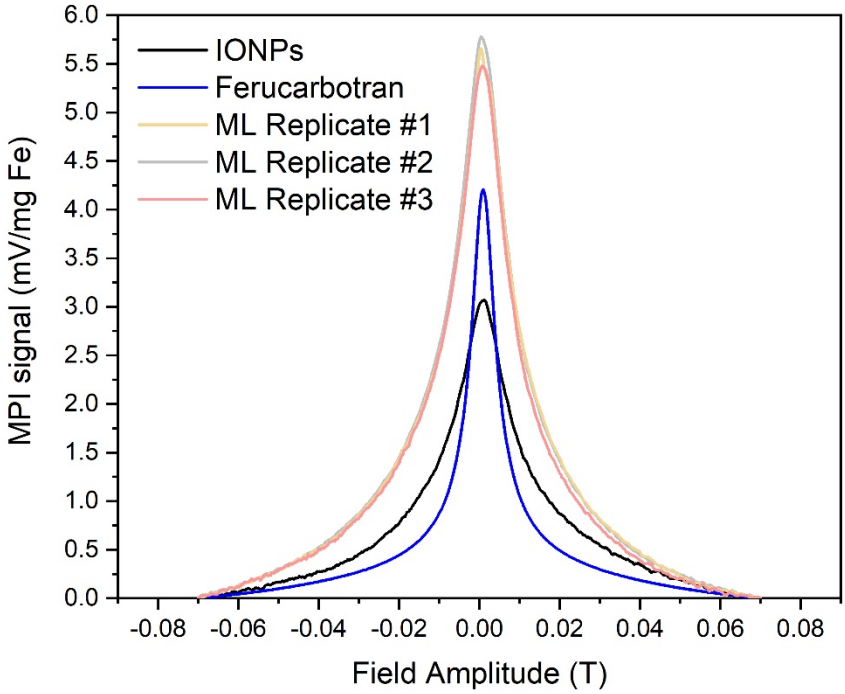

Reference: (ROST *et al.*, 2020).

It is evident the MPI signal amplitude increasing after particles encapsulation in liposomes. The MPI signal before entrapment (IONPs) was 3.08 mV/mg Fe in contrast to 5.80 mV/mg Fe when measuring ML. The ML were prepared in triplicate for been analyzed in MPI and confirm these results. All those samples had shown the same performance, that is, signal intensity higher than as-synthesized IONPs. The hypothesis is that, as has been reported for Ferucarbotran, the encapsulation made the particles being closer, the inter-particle interactions were altered and somehow, slightly improved the response in MPI.

The MPI performance of IONPs and ML, compared to Ferucarbotran, is also shown in Table 2.2 that describes the values of peak signal-to-noise ratio (PSNR), full-width-at-half-maximum (FWHM), resolution, and MPI signal, normalized per iron mass.

Table 2.2 – The values of FWHM, PSNR, expected resolution, and MPI signal of Ferucarbotran, IONPs, and ML.

Sample	FWHM (mT)	PSNR normalized per iron mass (a.u.)	Expected resolution (mm) at 6 T/m	MPI signal normalized per iron mass (mV/mg Fe)
Ferucarbotran	10.160 ± 0.003	2,767.4 ± 0.4	1.69	4.23
IONPs	23.780 ± 0.002	20,248.9 ± 0.4	3.96	3.08
ML	22.040 ± 0.012	27,388.6 ± 0.3	3.67	5.80

Reference: (ROST *et al.*, 2020).

Because the most representative fraction of IONPs was governed by Brownian mechanisms, it was expected a worsening in MPI performance after encapsulation. However, as revealed by DMS results, the entrapment of IONPs within liposomes structures did not impact the mechanism governing particles rotation. On the other hand, as demonstrated in Table 2.2, the FWHM of ML was lower than the observed for IONPs and also the resolution. The highest PSNR value was ascribed to ML. Concerning Ferucarbotran, the ML had shown a slightly higher signal per iron mass, even with a poorer expected resolution. These findings overall suggest slight improvements in MPI response of IONPs after being encapsulated in liposomes.

For reference, Figure 2.25 shows the combined images collected in isotropic modes of three magnetoliposomes replicates and IONPs, proving that both could be tracked by MPI and therefore, be applied as a diagnostic platform.

Figure 2.25 – Combined images of magnetoliposomes replicates (a) #1, (b) #2, (c) #3 and (d) IONPs, taken in isotropic mode.

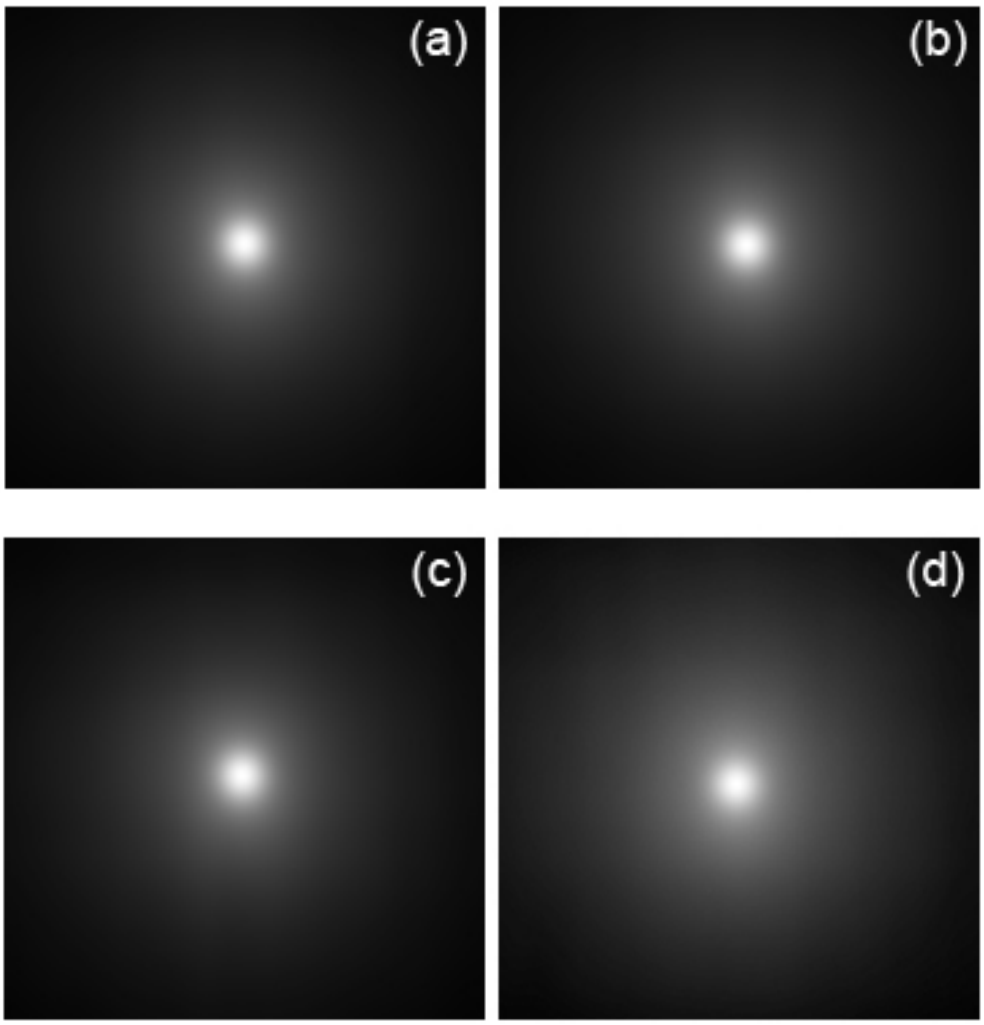

Reference: Author.

To state other types of tracers for MPI described in the literature, Starmans et. al (2013) reported micelles entrapping IONPs and studied their behavior in MPS for estimating the MPI performance. In comparison to the benchmark formulation Resovist, those micelles increased the MPS signal of the nanoparticles 4-6 times, considering iron mass, at the lower applied frequencies (< 0.5 MHz). The improvement was even better at the higher tested frequencies (> 1 MHz), in which those authors observed >200 times signal increasing for micelles with nanoparticles (STARMANS *et al.*, 2013). The results presented in this thesis corroborates the increase in signal of magnetic nanoparticles when encapsulated in a larger structure. However, the limitation of Starmans' work was

that straightforward information about the x-space formalism of MPI is not possible to be acquired by MPS measurements.

To highlight the potential usability of MPI, this new technique overcomes the drawbacks of using IONPs as contrast agents in MRI. For instance, MRI indirectly detects the nanoparticles by the relaxation effect of adjacent protons. Then, it is complicated to quantify IONPs in this case. Also, differentiate the hypointense nanoparticles signal in T_2 scans and the regions of tissue which has reduced signal in MRI is challenging. In summary, identifying IONPs biodistribution is questionable in MRI, even though this approach is extensively used in clinical diagnosis. The signal in MPI, on the other hand, is resulted from the nonlinear superparamagnetic response of IONPs that can be, therefore, locally tracked and quantified.

A comparison of the results presented in this Chapter is made to the reported by Maruyama et. al (2016). These authors evaluated magnetoliposomes loading doxorubicin or calcein in an MPI prototype operating at a frequency of the drive field 400 Hz and amplitude 20 mT (MURASE *et al.*, 2014; MARUYAMA *et al.*, 2016). Those scanner parameters matter because directly affect the tracer performance, considering the response to the magnetic field. For instance, at 20 kHz, Tay and co-authors (2018) noted insignificant heating of tumor in hyperthermia guided by MPI. However, this effect was pronounced when applying 354 kHz, which led to the heating of all tissues incorporated by SPIONs. The frequency in the preclinical imager Momentum from Magnetic Insight is 45 kHz and 25 kHz the commercialized by Bruker. Both systems operate at field amplitude up to 16 mT (TAY *et al.*, 2018). Because of the delay in particles magnetization caused by relaxation effects, the image resolution is affected by the interaction between nanoparticles and the MPI system, leading to a reduction in PSNR. For such reasons, Croft *et al*. (2016) reported a reduction in image blurring due to high frequency and low drive field amplitude (CROFT *et al.*, 2016).

Further, MPI prototypes generally use harmonic-space for reconstructing the images, which involves complicated inversions of matrices associated with more than a billion elements. The x-space formalism, on the other hand, processes the image in real-time and relies only on velocity and gridding compensation (GOODWILL *et al.*, 2012).

In respect to applications of magnetoliposomes as drug carriers, these materials have been suggested as promising agents in MRI. This is pertinent to the fact that one single liposome can be loaded with significant amounts of nanoparticles, which is favorable to producing satisfactory T_2-contrast agents. Moreover, combinatory therapies can arise from the ability of loading liposomes with small molecules of several drugs. In this case, therapeutic methods can be associated with imaging. Hybrid magneto-plasmonic liposomes had been developed by Tomitaka et. al (2018), starting from the co-encapsulation of a specific drug for treating Human immunodeficiency virus type 1 (HIV-1) and IONPs coated with gold. Studies of those authors revealed that microglia cells infected by HIV-1 were successfully treated by the magneto-plasmonic liposomes. The therapeutic administration was combined with imaging techniques. The hybrid liposomes provided bright positive contrast in X-ray computed tomography. A strong negative T_2-contrast was observed in MRI because of the magnetic core and in MPI, the magneto-plasmonic liposomes had shown signal proportional to the concentration (TOMITAKA *et al.*, 2018).

Future works would benefit from the investigation of MPI performance related to liposomes sizes, considering that smaller vesicles change nanoparticle packing and therefore, inter-particle interactions. In those studies, the dimension of magnetoliposomes could be reduced for membrane extrusion, for example. To state, higher T_1 relaxivity was found in MRI by Ghaghada *et al*. (2008) when applying liposomes as small as 50 nm, entrapping gadolinium (GHAGHADA *et al.*, 2008).

2.4 CONCLUSIONS

In this work, the magnetoliposomes prepared with IONPs@TMAOH were tested in the MPI Momentum imager from Magnetic Insight, Inc. and compared to the as-synthesized IONPs and the benchmark formulation Ferucarbotran. Even if a worsening in MPI performance was expected because the fraction of 0.69 was related to particles relaxing by Brownian rotation, an enhancement in the signal was observed for magnetoliposomes. Such results indicated that even after being entrapped in larger structures, IONPs were still able to rotate and respond to the external field. The MPI data, FWHM, and PSNR were better when analyzing magnetoliposomes, suggesting that interacting particles are probably more efficient as tracers due to being packed closely. It was concluded that the prepared magnetoliposomes presented poorer resolution than Ferucarbotran, but better signal per iron mass.

Additionally, the peptization of particles' surfaces significantly improved the size distribution and average diameter. As confirmed by TEM micrographs, IONPs@TMAOH were dispersed, which was also observed in the colloidal solution that did not settle out over time, considering almost one year of observation.

3 GENERAL CONCLUSIONS

Chapter 1: ***Synthesis of Iron Oxides Nanoparticles Optimized by Design of Experiments*** presented the application of experimental design, especially the Plackett-Burman method, for estimating the most important factors and levels of coprecipitation on IONPs hydrodynamic diameter and composition. It was concluded that such reactions can be performed with more reliability when this statistical tool is used. Further, the randomization minimizes the number of required experiments, which is cost-effective and less time-consuming. By doing so, IONPs were produced and the ideal protocol established, aiming to synthesize particles within nanoscale size and composed by magnetite. However, in this work, the surface was not stabilized, which implied in sedimentation of all samples.

Chapter 2: ***Magnetic Particle Imaging Performance of Liposomes Encapsulating Iron Oxide Nanoparticles*** described the encapsulation of IONPs in liposomes, which can benefit biomedical applications requiring drug co-encapsulation, delivery, release, and imaging tools. TEM micrographs revealed the encapsulation. As an optimization for magnetoliposomes preparation, SPIONs@TMAOH and bare SPIONs were initially tested at a concentration ranging from 0.3 to 3 mg/mL. Both particles were analyzed in DLS for determining the Zeta Potential and the stability of SPIONs@TMAOH was evident, contrary to what was observed for bare SPIONs. Additionally, the sedimentation of bare SPIONs was noted. The stable nanoparticles had shown the highest MPR signal.

The optimal nanoparticle for magnetoliposomes preparation was SPIONs@TMAOH at 2.0 mg/mL of magnetite. TEM micrographs confirmed the encapsulation and more than 1,000 magnetoliposomes across images, which supported to perform statistical analyses for determining the physical size and distribution. In the optimal replicates of magnetoliposomes, the amount of non-encapsulated particles and empty vesicles was negligible compared to loaded liposomes.

The MPI performance was slightly better after encapsulating the magnetic nanoparticles in larger structures, as has been suggested in the literature for Ferucarbotran. In comparison to the benchmark formulation, the magnetoliposomes presented poorer resolution but better signal per iron mass.

REFERENCES

ABENOJAR, E. C. *et al.* Structural effects on the magnetic hyperthermia properties of iron oxide nanoparticles. **Progress in Natural Science: Materials International,** v. 26, n. 5, p. 440-448, 2016. https://doi.org/10.1016/j.pnsc.2016.09.004

AHN, T. *et al.* Formation pathways of magnetite nanoparticles by coprecipitation method. **The journal of physical chemistry C,** v. 116, n. 10, p. 6069-6076, 2012. https://doi.org/10.1021/jp211843g

ALBERTS, B. *et al.* Molecular Biology of the Cell 4th edn (New York: Garland Science). **Ann Bot,** v. 91, p. 401, 2002. https://doi.org/10.1093/aob/mcg023

AMSTAD, E. *et al.* Triggered release from liposomes through magnetic actuation of iron oxide nanoparticle containing membranes. **Nano letters,** v. 11, n. 4, p. 1664-1670 2011. http://doi.org/10.1021/nl2001499

ANDRADE, Â. L. *et al.* Effect of tetramethylammonium hydroxide on nucleation, surface modification and growth of magnetic nanoparticles. **Journal of Nanomaterials,** v. 2012, p. 15 2012. http://doi.org/10.1155/2012/454759

BARBOSA, T. C. *et al.* Política de inovação em nanotecnologia no Brasil: a trajetória dos instrumentos financeiros não reembolsáveis. **Revista Tecnologia e Sociedade,** v. 14, n. 31, p. 56-74, 2018.

BIKIARIS, D. *et al.* Ochre-differentiation through micro-Raman and micro-FTIR spectroscopies: application on wall paintings at Meteora and Mount Athos, Greece. **Spectrochimica Acta Part A: Molecular and Biomolecular Spectroscopy,** v. 56, n. 1, p. 3-18 2000. http://doi.org/10.1016/S1386-1425(99)00134-1

BRADLEY, E. L. *et al.* Applications of nanomaterials in food packaging with a consideration of opportunities for developing countries. **Trends in food science & technology,** v. 22, n. 11, p. 604-610, 2011. https://doi.org/10.1016/j.tifs.2011.01.002

BRAHMANWADE, K. *et al.* Fungicidal activity of cu nanoparticles against Fusarium causing crop disease. **Environ Chem Lett,** v. 14, p. 229-235, 2016. https://doi.org/10.1007/s10311-015-0543-1

CHANTRELL, R. *et al.* Measurements of particle size distribution parameters in ferrofluids. **IEEE Transactions on Magnetics,** v. 14, n. 5, p. 975-977, 1978. https://doi.org/10.1109/TMAG.1978.1059918

CHATTERJEE, A. K. X-ray diffraction. **Handbook of analytical techniques in concrete science and technology**, p. 275-332, 2001.

CHEN, Y. *et al.* Applications of micro-fourier transform infrared spectroscopy (FTIR) in the geological sciences—a review. **International journal of molecular sciences,** v. 16, n. 12, p. 30223-30250, 2015. https://doi.org/10.3390/ijms161226227

CHUKANOV, N. V.; CHERVONNYI, A. D. **Infrared spectroscopy of minerals and related compounds**. Springer, 2016.

CHUKHROV, F. V. *et al.* Feroxyhyte, a new modification of FeOOH. **International Geology Review,** v. 19, n. 8, p. 873-890, 1977. https://doi.org/10.1080/00206817709471086

CORNELL, R. M.; SCHWERTMANN, U. **The iron oxides: structure, properties, reactions, occurrences and uses**. John Wiley & Sons, 2003.

CROFT, L. R. *et al.* Low drive field amplitude for improved image resolution in magnetic particle imaging Low drive field amplitude for improved image resolution in magnetic particle imaging. 2016. https://doi.org/10.1118/1.4938097

DE, M. C.; JONIAU, M. Magnetoliposomes. Formation and structural characterization. **European biophysics journal: EBJ,** v. 15, n. 5, p. 311-319 1988. http://doi.org/10.1007/bf00256482

DEATSCH, A. E.; EVANS, B. A. Heating efficiency in magnetic nanoparticle hyperthermia. **Journal of Magnetism and Magnetic Materials,** v. 354, p. 163-172, 2014. https://doi.org/10.1016/j.jmmm.2013.11.006

DEMAS, V.; LOWERY, T. J. Magnetic resonance for in vitro medical diagnostics: superparamagnetic nanoparticle-based magnetic relaxation switches. **New Journal of Physics,** v. 13, n. 2, p. 025005, 2011. https://doi.org/10.1088/1367-2630/13/2/025005

DEMIR, V. *et al.* Influence of alpha and gamma-iron oxide nanoparticles on marine microalgae species. **Bulletin of environmental contamination and toxicology,** v. 95, n. 6, p. 752-757 2015. http://doi.org/10.1007/s00128-015-1633-2

DEVI, M.; MOHANTA, D. Rheological properties of Iron oxide based ferrofluids. 2009, American Institute of Physics. p.495-501.

EINSTEIN, A. On the motion of small particles suspended in liquids at rest required by the molecular-kinetic theory of heat. **Annalen der physik,** v. 17, n. 549-560, p. 208, 1905.

ENRIQUEZ-NAVAS, P. M.; GARCIA-MARTIN, M. L. Application of inorganic nanoparticles for diagnosis based on MRI. In: (Ed.). **Frontiers of Nanoscience**: Elsevier, v.4, 2012. p.233-245. ISBN 1876-2778.

EPP, J. X-ray diffraction (XRD) techniques for materials characterization. In: (Ed.). **Materials characterization using Nondestructive Evaluation (NDE) methods**: Elsevier, 2016. p.81-124.

FAIVRE, D. **Iron oxides: from nature to applications**. John Wiley & Sons, 2016.

FERGUSON, R. M. *et al.* Optimization of nanoparticle core size for magnetic particle imaging. **Journal of magnetism and magnetic materials,** v. 321, n. 10, p. 1548-1551, 2009. https://doi.org/10.1016/j.jmmm.2009.02.083

FRYXELL, G. E.; CAO, G. **Environmental applications of nanomaterials: synthesis, sorbents and sensors**. World Scientific, 2012.

FULLER, E. G. *et al.* Externally triggered heat and drug release from magnetically controlled nanocarriers. **ACS Applied Polymer Materials,** v. 1, n. 2, p. 211-220, 2019. https://doi.org/10.1021/acsapm.8b00100

GARRAUD, N. *et al.* Benchtop magnetic particle relaxometer for detection, characterization and analysis of magnetic nanoparticles. **Physics in Medicine & Biology,** v. 63, n. 17, p. 175016, 2018. https://doi.org/10.1088/1361-6560/aad97d

GHAGHADA, K. *et al.* T1 relaxivity of core-encapsulated gadolinium liposomal contrast agents—effect of liposome size and internal gadolinium concentration. **Academic radiology,** v. 15, n. 10, p. 1259-1263, 2008. https://doi.org/10.1016/j.acra.2008.04.018

GHASEMZADEH, G. *et al.* Applications of nanomaterials in water treatment and environmental remediation. **Frontiers of Environmental Science & Engineering,** v. 8, n. 4, p. 471-482, 2014. https://doi.org/10.1007/s11783-014-0654-0

GILBERT, F. *et al.* Synthesis of goethite from Fe (OH) 2 precipitates: Influence of Fe (II) concentration and stirring speed. **Journal of Physics and Chemistry**

of Solids, v. 69, n. 8, p. 2124-2130, 2008. https://doi.org/10.1016/j.jpcs.2008.03.010

GLEICH, B.; WEIZENECKER, J. Tomographic imaging using the nonlinear response of magnetic particles. **Nature,** v. 435, n. 7046, p. 1214-1217, 2005. https://doi.org/10.1038/nature03808

GOODWILL, P. W. *et al.* X-space MPI: magnetic nanoparticles for safe medical imaging. **Advanced Materials,** v. 24, n. 28, p. 3870-3877, 2012. https://doi.org/10.1002/adma.201200221

GRIFFITHS, P. R.; DE HASETH, J. A. **Fourier transform infrared spectrometry**. John Wiley & Sons, 2007.

HAKEEM, N. A. *et al.* Study of the thermal transformation of natural goethite using infrared spectroscopy. **Journal of materials science letters,** v. 5, n. 1, p. 4-6, 1986. https://doi.org/10.1007/BF01671416

HERNANDO, A. *et al.* Magnetic hysteresis. 2001. https://doi.org/10.1016/B0-08-043152-6/00835-4

HERZ, S. *et al.* Magnetic particle imaging guided real-time percutaneous transluminal angioplasty in a phantom model. **Cardiovascular and interventional radiology,** v. 41, n. 7, p. 1100-1105, 2018. https://doi.org/10.1007/s00270-018-1955-7

HIBBERT, D. B. Experimental design in chromatography: a tutorial review. **Journal of chromatography B,** v. 910, p. 2-13, 2012. https://doi.org/10.1016/j.jchromb.2012.01.020

HOU, X. *et al.* Applications of Fourier transform infrared spectroscopy technologies on asphalt materials. **Measurement,** v. 121, p. 304-316, 2018. https://doi.org/10.1016/j.measurement.2018.03.001

HUNTER, R. J. **Zeta potential in colloid science: principles and applications**. Academic press, 2013. ISBN 1483214087.

HUPFFER, H. M.; LAZZARETTI, L. L. Nanotecnologia e sua regulamentação no Brasil. **Revista Gestão e Desenvolvimento,** v. 16, n. 3, p. 153-177, 2019.

ISO, I. S. Methods for determination of particle size distribution part 8: Photon correlation spectroscopy. **International Organisation for Standardisation (ISO)**, 1996.

IYENGAR, S. J. *et al.* Colloidal properties of water dispersible magnetite nanoparticles by photon correlation spectroscopy. **RSC Advances,** v. 6, n. 17, p. 14393-14402, 2016. http://doi.org/10.1039/C5RA26488J

JAYAKUMAR, T. G., Gnanaprakash, S., Mahadevan, P., Kalyanasundaram, ve ark., Effect of initial pH and temperature of iron salt solution on formation of magnetite nanoparticles. **Materials Chemistry and Physics,** v. 103, n. 1, p. 168-175, 2007. https://doi.org/10.1016/j.matchemphys.2007.02.011

JEONG, U. *et al.* Superparamagnetic colloids: controlled synthesis and niche applications. **Advanced Materials,** v. 19, n. 1, p. 33-60, 2007. https://doi.org/10.1002/adma.200600674

KAMMARI, R. *et al.* Nanoparticulate systems for therapeutic and diagnostic applications. In: (Ed.). **Emerging Nanotechnologies for Diagnostics, Drug Delivery and Medical Devices**: Elsevier, 2017. p.105-144.

KARAAGAC, O.; KOCKAR, H. Effect of synthesis parameters on the properties of superparamagnetic iron oxide nanoparticles. **Journal of superconductivity and novel magnetism,** v. 25, n. 8, p. 2777-2781, 2012a. https://doi.org/10.1007/s10948-011-1264-8

KARAAGAC, O.; KOCKAR, H. Iron oxide nanoparticles co-precipitated in air environment: effect of [Fe $^{+ 2} $]/[Fe $^{+ 3} $] ratio. **IEEE Transactions on Magnetics,** v. 48, n. 4, p. 1532-1536, 2012b. https://doi.org/10.1109/TMAG.2011.2173313

KARAAGAC, O.; KOCKAR, H. A simple way to obtain high saturation magnetization for superparamagnetic iron oxide nanoparticles synthesized in air atmosphere: Optimization by experimental design. **Journal of Magnetism and Magnetic Materials,** v. 409, p. 116-123, 2016.

KARAAGAC, O. *et al.* A simple way to synthesize superparamagnetic iron oxide nanoparticles in air atmosphere: iron ion concentration effect. **IEEE Transactions on Magnetics,** v. 46, n. 12, p. 3978-3983, 2010. http://doi.org/10.1109/TMAG.2010.2076824

KARAAGAC, O. *et al.* Properties of iron oxide nanoparticles synthesized at different temperatures. **Journal of superconductivity and novel magnetism,** v. 24, n. 1-2, p. 675-678, 2011. https://doi.org/10.1007/s10948-010-0932-4

KHOT, L. R. *et al.* Applications of nanomaterials in agricultural production and crop protection: a review. **Crop protection,** v. 35, p. 64-70, 2012. https://doi.org/10.1016/j.cropro.2012.01.007

KHURANA, A. *et al.* Role of nanotechnology behind the success of mRNA vaccines for COVID-19. **Nano Today,** v. 38, p. 101142, 2021.

KRALJ, S. *et al.* Design and fabrication of magnetically responsive nanocarriers for drug delivery. **Current medicinal chemistry,** v. 24, n. 5, p. 454-469 2017. http://doi.org/10.2174/0929867323666160813211736

LAMER, V. K.; DINEGAR, R. H. Theory, production and mechanism of formation of monodispersed hydrosols. **Journal of the American Chemical Society,** v. 72, n. 11, p. 4847-4854 1950. http://doi.org/10.1021/ja01167a001

LAURENT, S. *et al.* Magnetic iron oxide nanoparticles: synthesis, stabilization, vectorization, physicochemical characterizations, and biological applications. **Chemical reviews,** v. 108, n. 6, p. 2064-2110, 2008. https://doi.org/10.1021/cr068445e

LEE, N.; HYEON, T. Designed synthesis of uniformly sized iron oxide nanoparticles for efficient magnetic resonance imaging contrast agents. **Chemical Society Reviews,** v. 41, n. 7, p. 2575-2589, 2012. https://doi.org/10.1039/C1CS15248C

LI, Y.-S. *et al.* Infrared and Raman spectroscopic studies on iron oxide magnetic nano-particles and their surface modifications. **Journal of Magnetism and Magnetic Materials,** v. 324, n. 8, p. 1543-1550 2012. http://doi.org/10.1016/j.jmmm.2011.11.065

LIM, J. *et al.* Characterization of magnetic nanoparticle by dynamic light scattering. Nanoscale Res Lett 8 (1): 381. **Go to original source... Go to PubMed**, 2013. https://doi.org/10.1186/1556-276X-8-381

LOPES, C. D. C. A. *et al.* Fourier transform infrared spectroscopy (FTIR) application chemical characterization of enamel, dentin and bone. **Applied Spectroscopy Reviews,** v. 53, n. 9, p. 747-769, 2018. https://doi.org/10.1080/05704928.2018.1431923

MAHMOUDI, M. *et al.* Optimal design and characterization of superparamagnetic iron oxide nanoparticles coated with polyvinyl alcohol for targeted delivery and imaging. **The Journal of Physical Chemistry B,** v. 112, n. 46, p. 14470-14481, 2008. https://doi.org/10.1021/jp803016n

MALDONADO-CAMARGO, L. *et al.* Estimating the contribution of Brownian and Néel relaxation in a magnetic fluid through dynamic magnetic susceptibility measurements. **Journal of Magnetism and Magnetic Materials,** v. 412, p. 223-233, 2016. https://doi.org/10.1016/j.jmmm.2016.03.087

MANSOORI, G. A. **Principles of nanotechnology: molecular-based study of condensed matter in small systems**. World Scientific, 2005.

MARUYAMA, S. *et al.* Development of magnetic nanocarriers based on thermosensitive liposomes and their visualization using magnetic particle imaging. **Int. J. Nanomed. Nanosurg,** v. 2, n. 2, 2016. https://doi.org/10.16966/2470-3206.111

MASSART, R. Preparation of aqueous magnetic liquids in alkaline and acidic media. **IEEE transactions on magnetics,** v. 17, n. 2, p. 1247-1248, 1981.

MÉRIDA, F. *et al.* Optimization of synthesis and peptization steps to obtain iron oxide nanoparticles with high energy dissipation rates. **Journal of magnetism and magnetic materials,** v. 394, p. 361-371, 2015. https://doi.org/10.1016/j.jmmm.2015.06.076

MOHAPATRA, J.; LIU, J. P. Rare-Earth-Free Permanent Magnets: The Past and Future. In: (Ed.). **Handbook of Magnetic Materials**: Elsevier, v.27, 2018. p.1-57. ISBN 1567-2719.

MOROS, M. *et al.* Triggering antitumoural drug release and gene expression by magnetic hyperthermia. **Advanced drug delivery reviews,** v. 138, p. 326-343, 2019. https://doi.org/10.1016/j.addr.2018.10.004

MURASE, K. *et al.* Development of a system for magnetic particle imaging using neodymium magnets and gradiometer. **Japanese Journal of Applied Physics,** v. 53, n. 6, p. 067001, 2014. https://doi.org/10.7567/JJAP.53.067001

MUSIĆ, S. *et al.* Mossbauer spectroscopy, X-ray diffraction and IR spectroscopy of oxide precipitates formed from FeSO 4 solution. **Croatica Chemica Acta,** v. 59, n. 4, p. 833-851 1986.

ORDOUKHANIAN, J. *et al.* One step paired electrochemical synthesis of iron and iron oxide nanoparticles. **Materials Science-Poland,** v. 34, n. 3, p. 655-658 2016. http://doi.org/10.1515/msp-2016-0090

ORENDORFF, R. *et al.* First in vivo traumatic brain injury imaging via magnetic particle imaging. **Physics in Medicine & Biology,** v. 62, n. 9, p. 3501, 2017. https://doi.org/10.1088/1361-6560/aa52ad

RAHMAN, M. *et al.* Biomedical applications of superparamagnetic nanoparticles in molecular scale. **Current Organic Chemistry,** v. 19, n. 11, p. 982-990, 2015.

RAMAN, A. *et al.* The application of infrared spectroscopy to the study of atmospheric rust systems—I. Standard spectra and illustrative applications to identify rust phases in natural atmospheric corrosion products. **Corrosion Science,** v. 32, n. 12, p. 1295-1306, 1991. https://doi.org/10.1016/0010-938X(91)90049-U

ROSENSWEIG, R. E. Ferrohydrodynamics Cambridge University Press Cambridge. **New York, Melbourne**, 1985. https://doi.org/10.1002/zamm.19870670626

ROST, N. C. V. *et al.* Synthesis of Iron Oxide Nanoparticles Optimized by Design of Experiments. **Brazilian Journal of Physics,** v. 49, n. 1, p. 22-27, 2019. https://doi.org/10.1007/s13538-018-0616-2

ROST, N. C. V. *et al.* Magnetic Particle Imaging Performance of Liposomes Encapsulating Iron Oxide Nanoparticles. **Journal of Magnetism and Magnetic Materials**, p. 166675, 2020. https://doi.org/10.1016/j.jmmm.2020.166675

SANTHOSH, P. B. *et al.* Effect of superparamagnetic iron oxide nanoparticles on fluidity and phase transition of phosphatidylcholine liposomal membranes. **International journal of nanomedicine,** v. 10, p. 6089, 2015. http://doi.org/10.2147/IJN.S89679

SARASWATHY, A. *et al.* Citrate coated iron oxide nanoparticles with enhanced relaxivity for in vivo magnetic resonance imaging of liver fibrosis. **Colloids and Surfaces B: Biointerfaces,** v. 117, p. 216-224, 2014. https://doi.org/10.1016/j.colsurfb.2014.02.034

SARITAS, E. U. *et al.* Magnetic particle imaging (MPI) for NMR and MRI researchers. **Journal of Magnetic Resonance,** v. 229, p. 116-126, 2013. https://doi.org/10.1016/j.jmr.2012.11.029

SEDLACIK, J. *et al.* Magnetic particle imaging for high temporal resolution assessment of aneurysm hemodynamics. **PloS one,** v. 11, n. 8, 2016. https://doi.org/10.1371/journal.pone.0160097

SEIBERT, J. A.; BOONE, J. M. X-ray imaging physics for nuclear medicine technologists. Part 2: X-ray interactions and image formation. **Journal of nuclear medicine technology,** v. 33, n. 1, p. 3-18, 2005.

SHARMA, A. *et al.* Antibody immobilized cysteamine functionalized-gold nanoparticles for aflatoxin detection. **Thin Solid Films,** v. 519, n. 3, p. 1213-1218, 2010. https://doi.org/10.1016/j.tsf.2010.08.071

SILVA, M. **How colours matter to philosophy**. Springer, 2017. ISBN 331967398X.

SKLUTE, E. C. *et al.* Spectral and morphological characteristics of synthetic nanophase iron (oxyhydr) oxides. **Physics and chemistry of minerals,** v. 45, n. 1, p. 1-26, 2018. https://doi.org/10.1007/s00269-017-0897-y

SMITH, B. C. **Fundamentals of Fourier transform infrared spectroscopy**. CRC press, 2011. ISBN 1420069306.

SPALDIN, N. A. **Magnetic materials: fundamentals and applications**. Cambridge university press, 2010. ISBN 1139491555.

SPIZZO, F. *et al.* Synthesis of ferrofluids made of iron oxide nanoflowers: Interplay between carrier fluid and magnetic properties. **Nanomaterials,** v. 7, n. 11, p. 373, 2017. https://doi.org/10.3390/nano7110373

SRIWONGSITANONT, S.; UENO, M. Effect of freeze-thawing process on the size and lamellarity of peg-lipid liposomes. **The Open Colloid Science Journal,** v. 4, n. 1, 2010. https://doi.org/10.2174/1876530001104010001

STARMANS, L. W. E. *et al.* Iron oxide nanoparticle-micelles (ION-micelles) for sensitive (molecular) magnetic particle imaging and magnetic resonance imaging. **PloS one,** v. 8, n. 2, p. e57335, 2013. https://doi.org/10.1371/journal.pone.0057335

SUN, T. *et al.* Engineered nanoparticles for drug delivery in cancer therapy. **Angewandte Chemie International Edition,** v. 53, n. 46, p. 12320-12364, 2014. https://doi.org/10.1002/anie.201403036

SWEZEY, K. M. Nikola Tesla. **Science,** v. 127, n. 3307, p. 1147-1159, 1958.

TARTAJ, P. *et al.* The preparation of magnetic nanoparticles for applications in biomedicine. **Journal of physics D: Applied physics,** v. 36, n. 13, p. R182, 2003. https://doi.org/10.1088/0022-3727/36/13/202

TAY, Z. W. *et al.* Magnetic particle imaging-guided heating in vivo using gradient fields for arbitrary localization of magnetic hyperthermia therapy. **ACS nano,** v. 12, n. 4, p. 3699-3713, 2018. https://doi.org/10.1021/acsnano.8b00893

THANH, N. T. K. **Magnetic nanoparticles: from fabrication to clinical applications**. CRC press, 2012.

THANH, N. T. K. *et al.* Mechanisms of nucleation and growth of nanoparticles in solution. **Chemical reviews,** v. 114, n. 15, p. 7610-7630 2014. http://doi.org/10.1021/cr400544s

TOMITAKA, A. *et al.* Hybrid magneto-plasmonic liposomes for multimodal image-guided and brain-targeted HIV treatment. **Nanoscale,** v. 10, n. 1, p. 184-194, 2018. https://doi.org/10.1039/C7NR07255D

TRIVEDI, M. K. *et al.* A comprehensive physicochemical, thermal, and spectroscopic characterization of zinc (II) chloride using X-ray diffraction, particle size distribution, differential scanning calorimetry, thermogravimetric analysis/differential thermogravimetric analysis, ultraviolet-visible, and Fourier transform-infrared spectroscopy. **International Journal of Pharmaceutical Investigation,** v. 7, n. 1, p. 33, 2017. https://doi.org/10.4103/jphi.JPHI_2_17

TSAI, D.-H. *et al.* Quantitative determination of competitive molecular adsorption on gold nanoparticles using attenuated total reflectance–fourier transform infrared spectroscopy. **Langmuir,** v. 27, n. 15, p. 9302-9313, 2011. https://doi.org/10.1021/la2005425

UNNI, M. *et al.* Thermal decomposition synthesis of iron oxide nanoparticles with diminished magnetic dead layer by controlled addition of oxygen. **ACS nano,** v. 11, n. 2, p. 2284-2303, 2017. https://doi.org/10.1021/acsnano.7b00609

VAN RIJSSEL, J. *et al.* Bimodal distribution of the magnetic dipole moment in nanoparticles with a monomodal distribution of the physical size. **Journal of Magnetism and Magnetic Materials,** v. 380, p. 325-329, 2015. https://doi.org/10.1016/j.jmmm.2014.09.058

VINHAS, R. *et al.* Gold nanoparticle-based theranostics: disease diagnostics and treatment using a single nanomaterial. **Nanobiosensors in Disease Diagnosis,** v. 4, p. 11, 2015. https://doi.org/10.2147/NDD.S60285

VUJIĆ, J. Nikola Tesla: Electrifying Legacy. **Scientific-Technical Review, LVI,** v. 2, p. 3-9, 2006.

WECKLER, B.; LUTZ, H. D. Lattice vibration spectra. Part XCV. Infrared spectroscopic studies on the iron oxide hydroxides goethite (α), akaganéite (β), lepidocrocite (γ), and feroxyhite (δ). **European Journal of Solid State and Inorganic Chemistry,** v. 35, n. 8-9, p. 531-544 1998. http://doi.org/10.1016/S0992-4361(99)80017-4

WU, W. *et al.* Recent progress on magnetic iron oxide nanoparticles: synthesis, surface functional strategies and biomedical applications. **Science and**

technology of advanced materials, v. 16, n. 2, p. 023501, 2015. https://doi.org/10.1088/1468-6996/16/2/023501

YU, E. Y. *et al.* Magnetic particle imaging: a novel in vivo imaging platform for cancer detection. **Nano letters,** v. 17, n. 3, p. 1648-1654, 2017. https://doi.org/10.1021/acs.nanolett.6b04865

YU, H. *et al.* Impact of ultraviolet radiation on the aging properties of SBS-modified asphalt binders. **Polymers,** v. 11, n. 7, p. 1111, 2019. https://doi.org/10.3390/polym11071111

ZHANG, J. *et al.* Application of Fourier transform infrared spectroscopy with chemometrics on postmortem interval estimation based on pericardial fluids. **Scientific reports,** v. 7, n. 1, p. 1-8, 2017. https://doi.org/10.1038/s41598-017-18228-7

ZHENG, B. *et al.* Quantitative magnetic particle imaging monitors the transplantation, biodistribution, and clearance of stem cells in vivo. **Theranostics,** v. 6, n. 3, p. 291, 2016. https://doi.org/10.7150/thno.13728

ZHOU, X. Y. *et al.* Magnetic particle imaging for radiation-free, sensitive and high-contrast vascular imaging and cell tracking. **Current opinion in chemical biology,** v. 45, p. 131-138, 2018. https://doi.org/10.1016/j.cbpa.2018.04.014

POSTGRADUATE MEMORY

Timeline

2017 – 2018: Doctorate course, IP&D/UNIVAP, Brazil.
2018 – 2019: Exchange internship, University of Florida, USA.
2019 – 2021: Doctorate course, IP&D/UNIVAP, Brazil.

Scientific articles published

1) **ROST, Nathanne Cristina Vilela**; GONÇALVES, GIULIA CAPIZZANI; PALMA, DENISE; CASTILHO, MAIARA LIMA; LEITE, PRISCILA MARIA S. CORREA M.; BROCA, FÁTIMA MARIA; RANIERO, LEANDRO. Comparação entre métodos de síntese de partículas magnéticas. Revista UniVap, v. 22, p. 872, 2017. DOI: http://dx.doi.org/10.18066/revistaunivap.v22i40.469.

2) **ROST, N. C. V.** et al. Synthesis of Iron Oxide Nanoparticles Optimized by Design of Experiments. **Brazilian Journal of Physics,** v. 49, n. 1, p. 22-27, 2019. DOI: https://doi.org/10.1007/s13538-018-0616-2.

3) **ROST, N. C. V.** et al. Magnetic Particle Imaging Performance of Liposomes Encapsulating Iron Oxide Nanoparticles. **Journal of Magnetism and Magnetic Materials**, p. 166675, 2020. DOI: https://doi.org/10.1016/j.jmmm.2020.166675.

Works presented in scientific events

1) BHATTACHARJEE, T. T.; Maiara Lima Castilho; Fátima Maria Broca; **Nathanne Cristina Vilela Rost**; Kevin Cecil Hewitt; Leandro Raniero. Study of secondary structure changes in Epidermal Growth Factor during nanoparticle functionalization. In: 10th International Conference on Nanophotonics, 2017, Recife. 10th International Conference on Nanophotonics, 2017.

2) **Nathanne Cristina Vilela Rost**; Giulia Capizzani Gonçalves; Denise Palma; Maiara Lima Castilho; Fátima Maria Broca; Leandro Raniero. Synthesis, characterization and application of magnetic particles as heavy metal adsorbents. In: 10th International Conference on Nanophotonics, 2017, Recife. 10th International Conference on Nanophotonics, 2017.

3) **Nathanne Cristina Vilela Rost**; Fátima Maria Broca ; Giulia Capizzani Gonçalves ; BHATTACHARJEE, T. T. ; Maiara Lima Castilho ; Leandro Raniero . Influência da razão molar entre os íons ferroso e férrico no tamanho e composição de partículas magnéticas. 2017. In: XVII Encontro Latino Americano de Pós-Graduação (XVII EPG), São José dos Campos. Ciência que aproxima, ciência que liberta, 2017.

4) Giulia Capizzani Gonçalves; **Nathanne Cristina Vilela Rost**; Fátima Maria Broca; Maiara Lima Castilho; Leandro Raniero. Avaliação da nucleação e crescimento de partículas magnéticas durante a reação de síntese. In: XXI Encontro Latino Americano de Iniciação Científica (XXI INIC), 2017, São José dos Campos. Ciência que aproxima, ciência que liberta, 2017.

5) Giulia Capizzani Gonçalves; Marcela Aparecida Cândido; **Nathanne Cristina Vilela Rost**; Fátima Maria Broca; Leandro Raniero. Estudo da sedimentação de nanopartículas de óxido de ferro pela técnica de espalhamento dinâmico da luz. In: XXII Encontro Latino Americano de Iniciação Científica (XXII INIC), 2018, São José dos Campos. Patrimônio e cultura: desafios da ciência frente a identidades plurais, 2018.

6) **Nathanne Cristina Vilela Rost**; Viviane Paula dos Santos Jesus; Giulia Capizzani Gonçalves; Maiara Lima Castilho ; Leandro Raniero . The rule of experimental parameters of magnetic nanoparticles synthesized with amino acid based on design of experiments. In: Encontro de Outono da

Sociedade Brasileira de Física, 2018, Foz do Iguaçu. Encontro de Outono da Sociedade Brasileira de Física, 2018.

7) Thaís da Silva Veriato; **Nathanne Cristina Vilela Rost**; Olavo de Osti Comparato Filho; Marcela Aparecida Cândido; Maiara Lima Castilho; Leandro Raniero. Influence of gold nanoparticles concentrations in dynamic light scattering. In: Encontro de Outono da Sociedade Brasileira de Física, 2018, Foz do Iguaçu. Encontro de Outono da Sociedade Brasileira de Física, 2018.

8) JESUS, V. P. S.; LEMES, G.; **Rost, N.**; RANIERO, L.; CASTILHO, M. Silver Nanoparticles for Enhancement Photodynamic Therapy. In: Encontro de Outono da Sociedade Brasileira de Física, 2018, Foz do Iguaçu. Encontro de Outono da Sociedade Brasileira de Física, 2018.

9) **Nathanne Cristina Vilela Rost**; Marcela Aparecida Cândido ; Paula Fonseca Antunes Vieira ; Leandro Raniero ; Carlos Rinaldi . Aplicações teranósticas de nanopartículas de óxido de ferro. In: XX Encontro Latino Americano de Pós-Graduação, 2020, São José dos Campos. Sociedade em rede: educação, pesquisa e desafios nos tempos atuais, 2020.

10) Marcela Aparecida Cândido; Vitor Gabriel Poli de Lima; **Nathanne Cristina Vilela Rost**; Priscila Maria Sarmeiro Correia Marciano Leite; Maiara Lima Castilho; Leandro Raniero. Estudo da estabilidade de nanopartículas de óxido de ferro. In: XX Encontro Latino Americano de Pós-Graduação, 2020, São José dos Campos. Sociedade em rede: educação, pesquisa e desafios nos tempos atuais, 2020.

11) Marcela A.Cândido; Paula F. A. Vieira; **Nathanne C. V. Rost**; Giulia C. Gonçalves; Maiara L. Castilho; Leandro Raniero. The cytotoxicity of the water-based suspension of iron oxide nanoparticles stabilized by sodium citrate. In: II International Conference of Nanoscience and Nanobiotechnology, Brazil, 2021.

12) Viviane P. dos S. Jesus; **Nathanne C. V. Rost**; Paula F. A. Vieira; Maiara L. Castilho; Leandro Raniero. *In vitro* MTT assay of magnetic nanoparticles negatively charged by surfactant. In: II International Conference of Nanoscience and Nanobiotechnology, Brazil, 2021.

13) Marcela Aparecida Cândido, **Nathanne Cristina Vilela Rost**, Vitor Gabriel Poli de Lima, Maiara Lima Castilho, Leandro Raniero. "Synthesis and characterization study of iron oxide nanoparticles and core-shell with gold." In: Encontro de Outono da SBF 2021, Brasil – Online, 2021.

Participation in scientific events

1) V Simpósio de Física e Astronomia do Vale do Paraíba. 2017. (Simpósio).

2) 10th International Conference on Nanophotonics. Synthesis, characterization and application of magnetic particles as heavy metal adsorbents. 2017. (Congresso).

3) Encontro de Outono da Sociedade Brasileira de Física.Effects of iron oxide nanoparticles peptization on magnetoliposomes properties and the potential use in magnetic particle imaging. 2020. (Encontro).

4) I Congresso Digital de Nanobiotecnologia e Bioengenharia. 2020. (Congresso).

5) IV Escola de Inverno em Física Aplicada à Medicina e Biologia. 2020. (Outra).

Participation as examiner

1) XXIII Encontro Latino Americano de Iniciação Científica (XXIII INIC) e XIX Encontro Latino Americano de Pós-Graduação (XIX EPG).Subárea: Química. 2019. (Encontro).

2) XXIII Encontro Latino Americano de Iniciação Científica (XXIII INIC) e XIX Encontro Latino Americano de Pós-Graduação (XIX EPG).Subárea: Física. 2019. (Encontro).

3) XXIII Encontro Latino Americano de Iniciação Científica (XXIII INIC) e XIX Encontro Latino Americano de Pós-Graduação (XIX EPG).Subárea: Engenharia Química. 2019. (Encontro).

4) XXII Encontro Latino Americano de Iniciação Científica e XVIII Encontro Latino Americano de Pós-Graduação. Subárea: Engenharia Química. 2018. (Encontro).

5) XXII Encontro Latino Americano de Iniciação Científica e XVIII Encontro Latino Americano de Pós-Graduação. Subárea: Química. 2018. (Encontro).

6) XXIV Encontro Latino Americano de Iniciação Científica (XXIV INIC) e XX Encontro Latino Americano de Pós-Graduação (XX EPG).Subárea: Física (Avaliadora). 2020. (Encontro).

7) XXIV Encontro Latino Americano de Iniciação Científica (XXIV INIC) e XX Encontro Latino Americano de Pós-Graduação (XX EPG).Subárea: Engenharia Química (Avaliadora). 2020. (Encontro).

8) XXIV Encontro Latino Americano de Iniciação Científica (XXIV INIC) e XX Encontro Latino Americano de Pós-Graduação (XX EPG).Subárea: Química (Avaliadora). 2020. (Encontro).

Award

1) Segundo Melhor Trabalho da Área de Engenharias - XX Encontro Latino Americano de Pós-Graduação. "Aplicações teranósticas de nanopartículas de óxido de ferro", Universidade do Vale do Paraíba. 2020. (Encontro).